UNIVERSITÀ
DEGLI STUDI
DI PADOVA

Sede Amministrativa: Università degli Studi di Padova
Centro di Ateneo di Studi e Attività Spaziali "Giuseppe Colombo" - CISAS

CORSO DI DOTTORATO DI RICERCA IN: Scienze, Tecnologie e Misure Spaziali
CURRICOLO: Scienze e Tecnologie per Applicazioni Satellitari e Aeronautiche
Ciclo XXXIV

Space flight dynamics via invariant structures and chaos indicators methods

Coordinatore: Ch.mo Prof. Francesco Picano
Supervisore: Ch.mo Prof. Massimiliano Guzzo

Dottoranda: Erica Scantamburlo

Contents

Abstract

The solutions originating at the collinear Lagrangian points L_1, L_2, and L_3 of the Sun–Earth system have been proposed as ideal locations to perform observations of the Solar activities and of the space environment, as well as for station-keeping and low-energy orbital transfers. Since the Lagrangian points and the dynamics around them are extensively studied mainly in the circular restricted three-body problem (CR3BP), it is fundamental to understand how these dynamics are modified under the effect of the perturbations due to the other planets and of the elliptic shape of the Earth's orbit. The aim of this thesis is to analyze the solutions originating at the Sun–Earth L_1, L_2, L_3 in the presence of such perturbations, in connection to space flight applications. For this purpose, we consider several models for the motion of a spacecraft between the CR3BP and a realistic model of the Solar System which is compatible with the precision of the JPL digital ephemerides. We therefore consider as intermediate models the elliptic restricted three-body problem (ER3BP), the multicircular restricted eight-body problem (MCR8BP) as well as the bi-elliptic restricted four-body problem (BER4BP), and we apply the methods typical of the Dynamical Systems and the Hamiltonian perturbation theories. Specifically, we implement the construction of normal forms within the averaging method and the computation of chaos indicators. The thesis is divided into three chapters: in the first one, we provide an introduction to the subject; the second one focuses on the existence of motions in the restricted N-body problem remaining close to the Sun–Earth L_3 point for a time-span of interest for astrodynamics. Thanks to a combination of the Hamiltonian averaging method and the computation of fast Lyapunov indicators we find orbits in the realistic model of the Solar System that remain in the vicinity of the Sun–Earth L_3 for at least two centuries, and whose libration amplitudes range from 2.5×10^{-4} AU to 3×10^{-2} AU. The third chapter focuses on the differences of the manifold tubes originating at the Lagrangian points L_1 and L_2 of the inner planets of the Solar System when they are defined using the ER3BP, rather than the circular one. We find relevant differences, and we discuss the impact they have in the design of interplanetary mission trajectories. By analyzing the evolution of the orbital elements in the manifold tubes originating at the Lagrangian points L_1 and L_2, we find a threshold value for the eccentricity of the planet where we have a drastic change in the distribution of the longitudes of perihelion for a family of orbits in the manifold tubes which are of interest for interplanetary transfers. This leads to important changes in the design of a interplanetary mission trajectory between the manifold tubes originating at the Lagrangian points of different Sun–planet elliptic restricted three-body problems as, for example, the Hohmann transfers.

Sommario

Le soluzioni che si originano dagli equilibri Lagrangiani collineari L_1, L_2 ed L_3 del sistema Sole–Terra sono state proposte come luoghi ideali in cui osservare l'attività solare, lo spazio, così come per station keeping e trasferimenti orbitali a bassa energia. Poiché i punti Lagrangiani e le dinamiche attorno ad essi sono studiati principalmente nel problema circolare ristretto dei tre corpi (CR3BP), è fondamentale capire come queste dinamiche si modificano sotto l'effetto delle perturbazioni dovute agli altri pianeti e alla forma ellittica della traiettoria terrestre. L'obiettivo di questa tesi è di analizzare le soluzioni che si originano dai punti L_1, L_2, L_3 del sistema Sole–Terra in presenza di tali perturbazioni, in connessione alle applicazioni per il volo spaziale. A tal proposito, consideramo per il moto dello spacecraft diversi modelli tra il CR3BP ed un modello realistico del Sistema Solare che sia compatibile con la precisione del sistema digitale JPL per le effemeridi. Perciò consideriamo come modelli intermedi il problema ellittico dei tre corpi (ER3BP), il problema multicircolare degli otto corpi (MCR8BP) come anche il problema biellittico dei quattro corpi (BER4BP), e applichiamo i metodi tipici dei Sistemi Dinamici e la teoria perturbativa Hamiltoniana. Più precisamente, implementiamo la costruzione di forme normali utilizzando il metodo della media e il calcolo degli indicatori di caos. La tesi è divisa in tre capitoli: nel primo forniamo un'introduzione alla materia; il secondo si concentra sull'esistenza di moti che rimangono vicini ad L_3 del sistema Sole–Terra nel problema ristretto degli N-corpi per un intervallo di tempo di interesse per l'astrodinamica. Grazie alla combinazione del metodo della media Hamiltoniano e al calcolo dei fast Lyapunov indicators, troviamo orbite nel modello realistico del Sistema Solare che rimagono vicine ad L_3 del sistema Sole–Terra per almeno due secoli, e la cui ampiezza di librazione varia da 2.5×10^{-4} AU a 3×10^{-2} AU. Il terzo capitolo si focalizza sulla differenza tra le manifold tubes che si originano ai punti Lagrangiani L_1 ed L_2 dei pianeti interni del Sistema Solare quando sono definiti usando il ER3BP, rispetto a quello circolare. Troviamo delle differenze rilevanti e discutiamo l'impatto che queste ultime hanno nel design di una missione interplanetaria. Analizzando l'evoluzione degli elementi orbitali nelle manifold tubes che si originano ai punti Lagrangiani L_1 ed L_2, troviamo un valore soglia per l'eccentricità del pianeta dove abbiamo un cambiamento drastico della distribuzione delle longitudini del perielio per una famiglia di orbite nelle manifold tubes che sono di interesse per le missioni interplanetarie. Ciò comporta a cambiamenti importanti nel design delle traiettorie di una missione interplanetaria tra le manifold tubes che si originano ai punti Lagrangiani di diversi Sole-pianeta ER3BP come, per esempio, il trasferimento alla Hohmann.

Introduction

In the last decades, the Sun–Earth circular restricted three-body problem (CR3BP), namely a simplified model of the Solar System in which a spacecraft is gravitationally attracted by the Sun and the Earth, while the latter is performing a circular motion around the Sun, has been deeply investigated in connection to space flight dynamics. This is because the Sun–Earth CR3BP admits five equilibrium points, called the Lagrangian points, that represent ideal locations to perform observations of the Solar activities and of the space environment, as well as for station-keeping and low-energy orbital transfers (Farquhar, 1968; Breakwell, 1970; Euler and Yu, 1971; Farquhar et al., 1977, 1979; Lukjanov, 1980; Heuberger, 1977; Muhanen, 1983; Simó et al., 1987; Farquhar, 1998; Simó, 1999; Gómez et al., 2001; Howell and Pernika, 1993; Howell and Gordon, 1994; Hou et al., 2007; Tantardini et al., 2010; Koon et al., 2008; Tartaglia et al., 2018). As a matter of fact, there exists a lot of literature about the dynamics originating at the Lagrangian points L_1 and L_2 in the CR3BP, and the possibility to transfer a spacecraft from one equilibrium to another via the heteroclinic intersections between their manifold tubes (as example, the reader is referred to Conley, 1968; Gómez et al., 1993, 1998; Llibre et al., 1985; Simó et al., 1986; Howell et al., 1997, 1998; Gómez et al., 2001; Cobos and Masdemont, 2003; Dunham and Farquhar, 2003; Folta and Beckman, 2003; Koon et al., 2008; Howell and Kakoi, 2006; Parker and Anderson, 2013; Jorba, 2012; Farrés and Jorba, 2010; Martin et al., 2010; van Damme et al., 2010; Gómez and Mondelo, 2001). Moreover, several space missions were recently designed to reach the vicinity of the Sun–Earth L_1 and L_2 points, such as ISEE-3, WMAP, Herschel and Planck, Genesis, and SOHO. The Sun–Earth system is well approximated by the CR3BP, but if we are planning to design an interplanetary transfer between the Lagrangian points of different Sun-planet systems the CR3BP provides a crude approximation; in such a case, an extension of the model including the elliptic shape of the orbit of the planets and the planetary perturbations is required. Recently, particular emphasis was dedicated to the elliptic restricted three-body problem (ER3BP), which deals with the study of the motion of a body of negligible mass that is attracted by two celestial bodies performing an elliptic motion with respect to their common barycenter (Szebehely, 1967 and, more recently, Llibre and Piñol, 1990; Hiday-Johnston and Howell, 1994; Howell and Hiday-Johnston, 1994; de Almeida Prado, 1997; Palacián et al., 2006; de Almeida Prado and Neto, 2006; Gawlik et al., 2009; Hyeraci and Topputo, 2010; Ferreira et al., 2017; Ferrari and Lavagna, 2018; Qi and de Ruiter, 2018; Paez and Guzzo, 2021; Kumar et al., 2021), and to the bi-circular restricted four-body problem (BCR4BP), which deals with the study of the motion of a body of negligible mass gravitationally attracted by three celestial bodies, while two of them are performing circular motion around the central one (Michalodimitrakis, 1981; Andreu, 1998; Gabern and Jorba, 2001; Barrabés et al., 2016; Scantamburlo, 2018; Negri and Prado, 2020).

The dynamics originating at the collinear Lagrange points is determined by the motions on and

close to the so called center manifolds and its manifold tubes, that are defined by the motions which are asymptotic to the center manifold (see Sijbrand, 1985; Vanderbauwhede, 1989 for general results on the center manifolds, while for a sample of applications to the CR3BP we quote Jorba, 1999; Jorba and Masdemont, 1999; Andreu, 2002; Capiński and Roldán, 2012; Jorba and Farrès, 2010; Jorba, 2012; Guzzo and Lega, 2014; Celletti et al., 2015; Lega and Guzzo, 2016b; Ceccaroni et al., 2016; Bucciarelli et al., 2016; Guzzo and Lega, 2018; Pucacco, 2019). The analytic representation of the dynamics in a neighbourhood of the collinear equilibrium points can be performed through the so called reduction to the center manifold. Since L_1, L_2, and L_3 are center×saddle equilibria in the planar problem, the Hamiltonian of the CR3BP in a neighbourhood of L_1, L_2 or L_3 can be represented using canonical variables $\boldsymbol{Q}, \boldsymbol{P}$ defined using the Birkhoff normalization, in the form:

$$K(\boldsymbol{Q}, \boldsymbol{P}) = \sigma \frac{Q_1^2 + P_1^2}{2} + \lambda Q_2 P_2 + K_4(\boldsymbol{Q}, \boldsymbol{P}) + \ldots + K_N(\boldsymbol{Q}, \boldsymbol{P}) + R_N(\boldsymbol{Q}, \boldsymbol{P}) \tag{1}$$

where $(\boldsymbol{Q}, \boldsymbol{P}) = (0, 0, 0, 0)$ represents the equilibrium point; $K_4, K_6, \ldots, K_N$ are polynomials in $\boldsymbol{Q}, \boldsymbol{P}$ of order $4, 6, \ldots, N$ depending on the $\boldsymbol{Q}, \boldsymbol{P}$ only through the combination of the terms $(Q_1^2 + P_1^2)/2$ and $Q_2 P_2$, and R_N has Taylor expansion starting from order $N + 1$. Therefore, when N is suitably large, in a small neighbourhood of the origin we are allowed to neglect the remainder R_N, and to describe the dynamics using the integrable Hamiltonian:

$$K_N(\boldsymbol{Q}, \boldsymbol{P}) = \sigma \frac{Q_1^2 + P_1^2}{2} + \lambda Q_2 P_2 + K_4(\boldsymbol{Q}, \boldsymbol{P}) + \ldots + K_N(\boldsymbol{Q}, \boldsymbol{P}). \tag{2}$$

In this approximation, the variables Q_1, P_1 describe a non-linear elliptic motion, while the variables Q_2, P_2 describe a non linear hyperbolic motion. For $Q_1, P_1 = 0$ we obtain an approximation for the family of planar Lyapunov orbits, which constitute the center manifold of the planar problem. For $Q_2 = 0$ or $P_2 = 0$ instead we obtain motions which are asymptotic to the Lyapunov orbits, and define the manifold tubes, while for Q_2, P_2 both different from 0 we have orbits which are scattered by the Lyapunov orbits. For a detailed description of this procedure, also in the spatial problem, we refer to Jorba and Masdemont (1999). Together with the analytic approach, which is based on the computation of the Birkhoff normal form Hamiltonian in a neighbourhood of L_1, L_2, L_3 there are in the literature also numerical methods (Jorba and Villanueva, 1998; Gabern et al., 2005; Efthymiopoulos, 2013; Paez and Locatelli, 2014, 2015; Paez, 2016; Celletti et al., 2016; Paita et al., 2018; Caracciolo and Locatelli, 2020; Paez and Guzzo, 2020, 2021). In this thesis we use both the implementation of the Birkhoff normalization and the numerical method based on the definition of a suitable fast Lyapunov indicator (FLI hereafter). In the last decades to study the dynamics of complex dynamical systems several numerical methods based on the computation of the fast Lyapunov indicators were introduced. The FLI method was originally introduced by Froeschlé et al. (1997a,b) to discriminate between regular and chaotic orbits and afterwards developed in Froeschlé et al. (2000); Guzzo et al. (2002); Lega et al. (2003); Guzzo et al. (2009); Guzzo and Lega (2014); Lega and Guzzo (2016b); Guzzo and Lega (2018). Since the FLI method represents a powerful tool for the numerical analysis of the dynamics of complex systems, it has been applied to obtain sharp computations of the Arnold web (Froeschlé et al., 2000) and of Arnold diffusion (Lega et al., 2003; Guzzo et al., 2005) along it. The FLI proved to be so versatile that they found several applications: in Guzzo (2005, 2006) they have been used to compute the web of three and four planet resonances and the outer Solar System, and more recently they found several applications to

the dynamics of space debris (Daquin et al., 2016; Celletti et al., 2017; Gkolias et al., 2019) as well as to cometary dynamics (Guzzo and Lega, 2015, 2017). In particular, we will need the modifications of the FLI which have been introduced in order to sharply detect the stable and unstable manifolds of the center manifolds originating at the partially hyperbolic equilibrium points (Guzzo and Lega, 2014, 2015, 2017, 2018; Lega and Guzzo, 2016a,b).

The aim of this thesis is to analyze the solutions originating at the Sun–Earth Lagrangian points L_1, L_2 and L_3 in the presence of the planetary perturbations and by considering the elliptic shape of the planetary orbits in connection to space flight dynamics.

For this purpose we consider several intermediate models between the CR3BP and the complete N-body problem; such intermediate models are those defined by the multicircular restricted eight-body problem (MCR8BP), namely a model in which a body of negligible mass is gravitationally attracted by the Sun and the eight planets of the Solar System (from Mercury to Neptune) while the latter are performing a circular motion around the Sun, the ER3BP as well as and the bi-elliptic restricted four-body problem (BER4BP), namely a model in which a body of negligible mass is gravitationally attracted by the Sun and two planets, while the latter are both performing an elliptic motion around the Sun.

The first part of the thesis (described in Chapter 2) focuses on the short-period effects of the planetary perturbations on the Sun–Earth L_3 point, and it is based on the results of Scantamburlo and Guzzo (2020). The goal is to find orbits close to the Sun–Earth L_3 point that are useful for astrodynamics, i.e. orbits remaining close to the Lagrangian point at least for several decades in a model of the Solar System whose ephemerides are compatible with those provided by the JPL digital service. We recall that in a neighbourhood of the collinear equilibrium points in the CR3BP there are the periodic Lyapunov orbits, but since the planetary perturbations (mainly from Venus and Jupiter) on the Sun–Earth L_3 are stronger than the Earth attraction, the Sun–Earth CR3BP does not approximate well the dynamics of a spacecraft around L_3. Hence, to quantify the effects of such perturbations we consider the Sun–Earth MCR8BP where the eight planets, from Mercury to Neptune, are performing circular motions around the Sun. Using the techniques of Hamiltonian perturbation theory, we find that the Hamiltonian describing the dynamics of the MCR8BP is conjugate by a canonical transformation to an averaged Hamiltonian system still having an equilibrium close to L_3 and collinear with the Sun–Earth direction, up to terms of second order in the planetary masses and fourth order in the spacecraft eccentricity; we denote such equilibrium by $\mathcal{L}_3$; The image of $\mathcal{L}_3$ in the original Cartesian variables is a quasi-periodic orbit, that we identify as the dynamical substitute of L_3. We find that the contributions of the planets to the libration amplitude of the dynamical substitute sum up to about $d = 10^{-4}$ AU (about 15 000 km). Since $\mathcal{L}_3$ is partially hyperbolic, in its neighbourhood there are periodic and quasi-periodic orbits. Hence, we expect that when we map back these orbits of the averaged Hamiltonian to the original Hamiltonian system, we obtain librations around L_3 of amplitudes larger than d generalizing the Lyapunov orbits of the CR3BP. As the MCR8BP still provides a crude approximation of the dynamics in the real Solar System, we use the fast Lyapunov indicators as a tool to refine the results obtained in the MCR8BP and to numerically detect libration orbits that remain in a small neighbourhood $\mathcal{B}$ of the Sun–Earth L_3 point in a model where the motion of the planets is represented with a precision compatible with that of the JPL ephemerides system, for a time span of interest for space flight dynamics. To construct the neighbourhood $\mathcal{B}$ we need to consider the effects caused by the elliptic orbit of the Earth. Hence, for a given libration orbit of amplitude $\alpha > d$ we first compute a

Lyapunov orbit of amplitude α in the Sun–Earth CR3BP, and then we use such a Lyapunov orbit as an input for the FLI method to find orbits in the Sun–Earth ER3BP that remain close to the Lyapunov orbit up to 200 years. Subsequently we consider a realistic model of our Solar System in which the planetary ephemerides are compatible with those provided by the JPL digital service. Finally, we define the neighbourhood $\mathcal{B}$ as a neighbourhood of the librations orbit of amplitude $\rho \in (d, \alpha/10)$ found in the Sun–Earth ER3BP and we find libration orbits in the realistic model that remain in $\mathcal{B}$ for at least for 200 years. For $\alpha < 10d$ we apply the FLI method using a ball of radius α and centered at $\mathcal{L}_3$ as $\mathcal{B}$. With such methods we find libration orbits in the realistic model of the Solar System that remain close to the Sun–Earth L_3 point for at least 200 years, of amplitude ranging from 2.5×10^{-4} AU to 3×10^{-2} AU.

The second part of the thesis (described in Chapter 3) studies the definition of interplanetary transfers using the stable and unstable manifold tubes originating at L_1 and L_2 in the ER3BPs, and it is based on the results of Scantamburlo et al. (2021). In the literature, several papers were dedicated to the study of the dynamics in a neighbourhood of L_1 and L_2 in the ER3BP, and to the design of interplanetary transfers via gravity assists and ballistic captures (the reader is referred to Broucke, 1969; de Almeida Prado, 1997; de Almeida Prado and Neto, 2006; Hyeraci and Topputo, 2010; Hou and Liu, 2011; Peng et al., 2015; Peng and Xu, 2015; Peng et al., 2017; Qi et al., 2017; Ferreira et al., 2017, 2018; Ferrari and Lavagna, 2018). Our goal is to analyze the differences of the manifold tubes originating at L_1 and L_2 in the planar ER3BP and the CR3BP, and to discuss the impact they have in the design of interplanetary transfers. To do this, we first need to consider the generalization of the space manifold dynamics to the ER3BP defined in Paez and Guzzo (2021), obtained with the construction of suitable Hamiltonian Floquet-Birkhoff normal forms. Using the definition and the method of computation of the manifold tubes provided in Paez and Guzzo (2021), we first characterize the evolution of the orbital elements of a spacecraft whose motion is described by a solution of the ER3BP that belongs to the manifold tubes of a generic Sun–P_j system (here P_j denotes the j-th planet of the Solar System; P_1 Mercury, P_2 Venus, ...). Let us consider any solution whose initial condition belongs to the local unstable manifold tubes originating at L_1 or L_2: for an initial time-span the solution remains close the to Lagrangian one, oscillating around it; then it exits from the planet's Hill sphere. We follow its evolution until it arrives sufficiently far from the planet so that its dynamics is well approximated by a Keplerian orbit. The solutions whose initial condition belong to the stable manifold tube are characterized by the same behaviour for negative time-spans. Let us denote by $\mathcal{K}^s_{j,L_i}$ and $\mathcal{K}^u_{j,L_i}$ the families of all the Keplerian orbits that are obtained for all the possible initial conditions in the local stable and unstable manifold tubes originating at L_i of the Sun–P_j ER3BP, and for all the values of the initial true anomaly of P_j. The idea is to use the orbits in the families $\mathcal{K}^u_{h,L_i}$ and $\mathcal{K}^s_{k,L_m}$ of different planets P_h, P_k for the design of an interplanetary transfer between P_h and P_k. Depending on the value of the orbital eccentricity e_j of the planet P_j, we find different distribution of the longitude of perihelion of the orbits in the families $\mathcal{K}^s_{j,L_i}$ and $\mathcal{K}^u_{j,L_i}$. Precisely we find that for $e_j \gtrsim 3r_{\mathrm{H},j}/a_j$ where $r_{\mathrm{H},j}$ and a_j represent the Hill radius and the semi-major axis of P_j, the distribution of the longitude of perihelion in the families $\mathcal{K}^s_{j,L_i}$ and $\mathcal{K}^u_{j,L_i}$ is bounded in some interval whose length is $\Delta\varpi \sim 2 \arctan \frac{3r_{\mathrm{H},j}}{e_j}$. Conversely, i.e. for $e_j \lesssim 3r_{\mathrm{H},j}/a_j$, the distribution of the longitude of perihelion is spread in $[0, 2\pi]$. In connection to space flight dynamics, this leads to several consequences: i) if both the orbital eccentricities of P_h and P_k are such that the distributions of the longitude of perihelion in the families $\mathcal{K}^u_{h,L_i}$ and $\mathcal{K}^s_{k,L_m}$ are bounded in some intervals, and if such intervals do not match, then

it is not possible to perform an Hohmann transfer between the two families (for the definition of the Hohmann transfer between two co-axial elliptic orbits, the reader is referred to, for example, Curtis, 2005); ii) if both the orbital eccentricities of P_h and P_k are such that the distribution of the longitude of perihelion of the orbits in $\mathcal{K}^u_{h,L_i}$ and $\mathcal{K}^s_{k,L_m}$ are spread in $[0, 2\pi]$, then we have an abundance of co-axial orbits between the two families that are suitable for an Hohmann transfer; iii) if the orbital eccentricity of one planet is such that the distribution of the longitude of perihelion is bounded, but the other does not. In such a case we still have an abundance of co-axial orbits between the two families $\mathcal{K}^u_{h,L_i}$ and $\mathcal{K}^s_{k,L_m}$, and the Hohmann transfer can be considered. We note that if we plan to design an interplanetary transfer using two decoupled CR3BP, the situation described in ii) has to be considered. We apply these results to the Sun–Mercury, Sun–Earth, and Sun–Mars ER3BPs. Since both Mercury and Mars are such that the longitudes of perihelion of the Keplerian orbits are bounded, while the Earth does not, it is possible to apply an Hohmann transfer between the manifold tubes originating at a Lagrangian point of the Sun–Earth and Sun–Mercury (or Sun–Mars) ER3BP. Finally we check if the transfer computed using the two decoupled Sun–Earth and Sun–Mercury (or Sun–Mars) ER3BPs remain effective also in the Sun–Earth–Mercury (or Sun–Earth–Mars) BER4BP.

The thesis is organized as follows: Chapter 1 is dedicated an overview about the models and methods used during the PhD research program; in particular, we focus on the CR3BP and the ER3BP, and we emphasize the different techniques used to study such two problems. In particular Chapter 2 is dedicated to the study of the short-period effects of the planetary perturbations on the Sun–Earth L_3 point. Chapter 3 is dedicated to the interplanetary transfers between the manifold tubes originating at L_1 and L_2 in the ER3BPs.

Chapter 1

Fundamentals for Space Manifold Dynamics

A modern concept of mission design exploits the solutions originating at the Lagrangian points whose definition requires to consider, at least, the three-body problem. For this reason the modern astrodynamics is developed using advanced mathematical theories, mainly from the fields of Dynamical Systems and Hamiltonian Mechanics which are required when the Lagrangian solutions are considered.

The aim of this chapter is to provide an overview about the fundamentals of celestial mechanics which are used in the modern astrodynamics. In Sec. 1.1 we describe the circular restricted three-body problem: in such a context we define the Lagrangian points, the Jacobi constant, and we describe peculiar solutions originating at the collinear Lagrangian points. In Sec. 1.2 we consider the first extension of the circular restricted three-body problem to a model which is more realistic for space flight dynamics, namely the elliptic restricted three-body problem. In particular, we will explain which are the additional difficulties in the study of the solutions originating at the Lagrangian points in this model and we describe the state of art. Sec. 1.3 is dedicated to an overview of Hamiltonian perturbation theory. In Sec. 1.4 we review the finite time chaos indicators as a numerical tool for the analysis of the dynamics of complex dynamical systems. In Sec. 1.5 we briefly define the classical concept of impulsive orbital maneuver, whose most celebrated example is the Hohmann transfer.

1.1 The planar circular restricted three-body problem

1.1.1 The equations of motion

The planar circular restricted three-body problem (CR3BP) deals with the study of the dynamics of a body having negligible mass (which we identify as the "spacecraft") that is gravitationally attracted by two massive bodies P_1 and P_2 whose gravitational parameters will be denoted by ε_1 and ε_2. Moreover, we assume that P_2 is performing a circular motion around P_1. In a reference frame Oxy centered at P_1 with axes parallel to the axes of an inertial one, the position vector of P_2 is $\boldsymbol{r}_2(t) = d_2(\cos(n_2 t + \phi_2), \sin(n_2 t + \phi_2))$, where n_2, d_2, and ϕ_2 denote the mean motion, the orbital radius, and the initial phase displacement of P_2. By denoting with $\boldsymbol{r} = (x, y)$ the position vector of the spacecraft in the Oxy reference frame, the Lagrange function describing its dynamics

is

$$L(\boldsymbol{r},\dot{\boldsymbol{r}};t)=\frac{\|\dot{\boldsymbol{r}}\|^2}{2}+\frac{\varepsilon_1}{\|\boldsymbol{r}\|}-\varepsilon_2\left(\frac{\boldsymbol{r}\cdot\boldsymbol{r}_2(t)}{\|\boldsymbol{r}_2(t)\|^3}-\frac{1}{\|\boldsymbol{r}-\boldsymbol{r}_2(t)\|}\right). \tag{1.1}$$

In order to eliminate the explicit dependence on the time t from the Lagrangian, we introduce as usual the co-rotating reference frame OXY in which P_1 and P_2 are located at the origin and at $(d_2,0)$ respectively for all $t\in\mathbb{R}$. For this purpose we introduce the rotation matrix

$$\mathcal{R}=\begin{pmatrix}\cos(n_2t+\phi_2) & -\sin(n_2t+\phi_2)\\ \sin(n_2t+\phi_2) & \cos(n_2t+\phi_2)\end{pmatrix} \tag{1.2}$$

such that the position vector of the spacecraft in the co-rotating reference frame is $\boldsymbol{R}=\mathcal{R}^T\boldsymbol{r}$. Since

$$\|\dot{\boldsymbol{r}}\|^2=\|\dot{\boldsymbol{R}}\|^2+n_2^2\|\boldsymbol{R}\|^2+2n_2(X\dot{Y}-\dot{X}Y), \tag{1.3}$$

the Lagrange function describing the motion of the spacecraft in the heliocentric co-rotating reference frame is

$$\begin{aligned}\mathcal{L}(X,Y,\dot{X},\dot{Y})&=\frac{\dot{X}^2+\dot{Y}^2}{2}+\frac{n_2^2}{2}(X^2+Y^2)+n_2(X\dot{Y}-\dot{X}Y)+\frac{\varepsilon_1}{\sqrt{X^2+Y^2}}\\&\quad-\varepsilon_2\left(\frac{X}{d_2^2}-\frac{1}{\sqrt{(X-d_2)^2+Y^2}}\right)\\&=\frac{\dot{X}^2+\dot{Y}^2}{2}+n_2(X\dot{Y}-\dot{X}Y)-V(X,Y),\end{aligned} \tag{1.4}$$

where

$$V(X,Y)=-\frac{n_2^2}{2}(X^2+Y^2)-\frac{\varepsilon_1}{\sqrt{X^2+Y^2}}+\varepsilon_2\left(\frac{X}{d_2^2}-\frac{1}{\sqrt{(X-d_2)^2+Y^2}}\right). \tag{1.5}$$

The equations of motion of the spacecraft in the heliocentric co-rotating reference frame are provided by the Lagrange-Euler equations of (1.4), i.e.

$$\frac{d}{dt}\frac{\partial\mathcal{L}}{\partial\dot{X}}=\frac{\partial\mathcal{L}}{\partial X},\quad \frac{d}{dt}\frac{\partial\mathcal{L}}{\partial\dot{Y}}=\frac{\partial\mathcal{L}}{\partial Y}, \tag{1.6}$$

hence

$$\begin{aligned}\ddot{X}&=2n_2\dot{Y}+n_2^2X-\varepsilon_1\frac{X}{(X^2+Y^2)^{3/2}}-\varepsilon_2\left(\frac{1}{d_2^2}+\frac{X-d_2}{((X-d_2)^2+Y^2)^{3/2}}\right)\\ \ddot{Y}&=-2n_2\dot{X}+n_2^2Y-\varepsilon_1\frac{Y}{(X^2+Y^2)^{3/2}}-\varepsilon_2\frac{Y}{((X-d_2)^2+Y^2)^{3/2}}.\end{aligned} \tag{1.7}$$

It is usual to describe the motion of the spacecraft using units of measure such that the distance between P_1 and P_2 is one, the sum of the masses of P_1 and P_2 is one, and the revolution period of P_2 around P_1 is 2π; with such assumptions, we obtain $n_2=1$ and also the gravitational constant is one; hence we have $\varepsilon_1=1-\varepsilon_2$. The Hamilton function describing the dynamics of the CR3BP is obtained from the Lagrange function via the usual Legendre transform. Therefore, by introducing the momenta conjugate to the variables X and Y, i.e.

$$P_X=\frac{\partial\mathcal{L}}{\partial\dot{X}}=\dot{X}-Y,\qquad P_Y=\frac{\partial\mathcal{L}}{\partial\dot{Y}}=\dot{Y}+X, \tag{1.8}$$

the Legendre transform of $\mathcal{L}$ is

$$\mathcal{H}(X,Y,P_X,P_Y)=\frac{P_X^2+P_Y^2}{2}-(XP_Y-YP_X)-\frac{1-\varepsilon_2}{\sqrt{X^2+Y^2}}+\varepsilon_2\left(X-\frac{1}{\sqrt{(X-1)^2+Y^2}}\right). \quad (1.9)$$

The Hamilton equations of (1.9) are

$$\begin{aligned}
\dot{X}&=P_X+Y\\
\dot{Y}&=P_Y-X\\
\dot{P}_X&=P_Y-(1-\varepsilon_2)\frac{X}{(X^2+Y^2)^{3/2}}-\varepsilon_2\left(1+\frac{X-1}{((X-1)^2+Y^2)^{3/2}}\right)\\
\dot{P}_Y&=-P_X-(1-\varepsilon_2)\frac{Y}{(X^2+Y^2)^{3/2}}-\varepsilon_2\frac{Y}{((X-1)^2+Y^2)^{3/2}}.
\end{aligned} \quad (1.10)$$

1.1.2 The Jacobi constant and the Lagrangian points

In this subsection we find convenient to use the Lagrangian formulation of the CR3BP. Since the Lagrange function (1.4) is time independent, the CR3BP admits the constant of motion:

$$J(X,Y,\dot{X},\dot{Y})=\dot{X}\frac{\partial\mathcal{L}}{\partial\dot{X}}+\dot{Y}\frac{\partial\mathcal{L}}{\partial\dot{Y}}-\mathcal{L}(X,Y,\dot{X},\dot{Y})=\frac{\dot{X}^2+\dot{Y}^2}{2}+V(X,Y). \quad (1.11)$$

Instead of (1.11) it is historically used as first integral the *Jacobi constant*, defined by

$$C(X,Y,\dot{X},\dot{Y})=-2J(X,Y,\dot{X},\dot{Y}). \quad (1.12)$$

Since $\dot{X}^2+\dot{Y}^2\geq 0$, any solution $(X(t),Y(t))$ of the CR3BP characterized by a value $\mathcal{J}$ of the constant of motion (1.11) is constrained in the region

$$\mathcal{A}(\mathcal{J})=\{(X,Y):V(X,Y)\leq\mathcal{J}\}, \quad (1.13)$$

which is known as the *admissible region*. The border of $\mathcal{A}(\mathcal{J})$, i.e. $\mathcal{Z}(\mathcal{J})=\{(X,Y):V(X,Y)=\mathcal{J}\}$ is called the *zero velocity curve* (when $(X(t),Y(t))\in\mathcal{Z}(\mathcal{J})$, we have $(\dot{X}(t),\dot{Y}(t))=(0,0)$).

Let us now consider the equilibrium configurations of the system, which are the solutions of the equations $\frac{\partial V}{\partial X}=0$, $\frac{\partial V}{\partial Y}=0$, i.e.

$$X-\varepsilon_2\left(1+\frac{X-1}{((X-1)^2+Y^2)^{3/2}}\right)-(1-\varepsilon_2)\frac{X}{(X^2+Y^2)^{3/2}}=0 \quad (1.14)$$

$$Y\left[1-\frac{\varepsilon_2}{((X-1)^2+Y^2)^{3/2}}-\frac{1-\varepsilon_2}{(X^2+Y^2)^{3/2}}\right]=0. \quad (1.15)$$

We notice that:

(i) for $Y=0$ there are three values X_{L_1},X_{L_2},X_{L_3} satisfying the relation

$$X-\varepsilon_2\left(1+\frac{X-1}{|X-1|^3}\right)-(1-\varepsilon_2)\frac{X}{|X|^3}=0. \quad (1.16)$$

For convention $X_{L_3}<0<X_{L_1}<1<X_{L_2}$. Correspondingly, we have three equilibrium points, the so called *collinear Lagrange points* L_1, L_2, and L_3. In Fig. 1.1 we represent the

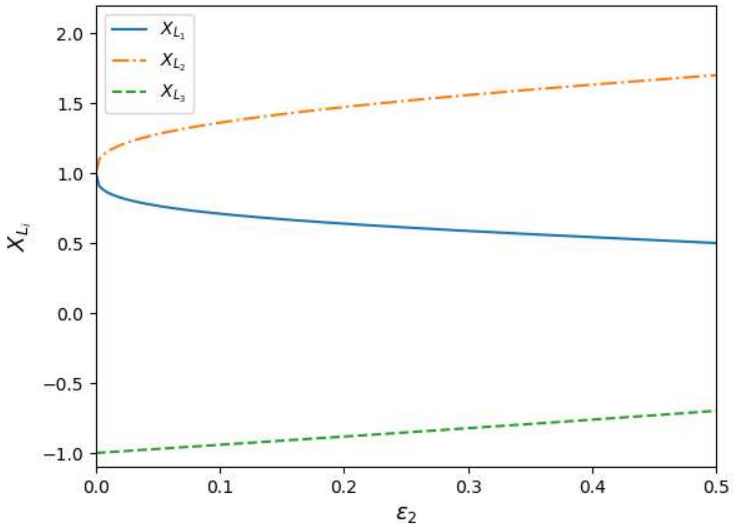

Figure 1.1: Location of the collinear equilibrium points L_1, L_2 and L_3 for different values of the gravitational parameter ε_2.

values of X_{L_1}, X_{L_2}, and X_{L_3} as a function of ε_2;

(ii) for $Y \neq 0$, from relation (1.15) we get

$$\frac{\varepsilon_2}{((X-1)^2+Y^2)^{3/2}} = 1 - \frac{1-\varepsilon_2}{(X^2+Y^2)^{3/2}}, \tag{1.17}$$

and consequently equation (1.14) reduces to

$$1 - \frac{1}{(X^2+Y^2)^{3/2}} = 0 \tag{1.18}$$

that is solved for $\sqrt{X^2+Y^2} = 1$; by replacing (1.18) in (1.17) then we also get $\sqrt{(X-1)^2+Y^2} = 1$. There are two points, L_4 and L_5, fulfilling such two conditions, that are

$$X_{L_4} = \frac{1}{2}, \quad Y_{L_4} = \frac{\sqrt{3}}{2} \tag{1.19}$$

$$X_{L_5} = \frac{1}{2}, \quad Y_{L_5} = -\frac{\sqrt{3}}{2}, \tag{1.20}$$

usually called the *triangular Lagrange points*.

Hence there exist five equilibrium configurations L_1, L_2, L_3, L_4, and L_5, whose location in the XY plane is schematically represented in Fig. 1.2. We emphasize that, given $\mathcal{J}_{L_1} = V(X_{L_1}, 0)$, $\mathcal{J}_{L_2} = V(X_{L_2}, 0)$, $\mathcal{J}_{L_3} = V(X_{L_3}, 0)$, $\mathcal{J}_{L_4} = V(X_{L_4}, 0)$ and $\mathcal{J}_{L_5} = V(X_{L_5}, 0)$, we have

$$\mathcal{J}_{L_1} < \mathcal{J}_{L_2} < \mathcal{J}_{L_3} < \mathcal{J}_{L_4} = \mathcal{J}_{L_5}. \tag{1.21}$$

To better understand the property of the orbits in the OXY plane, we plot the different realms of motion for different values of the constant of motion $\mathcal{J}$ (the reader is referred to Figures 1.3 and 1.4), for the sample value $\varepsilon_2 = 0.1$. We note that for $\mathcal{J} < \mathcal{J}_{L_1}$ (case represented in panel

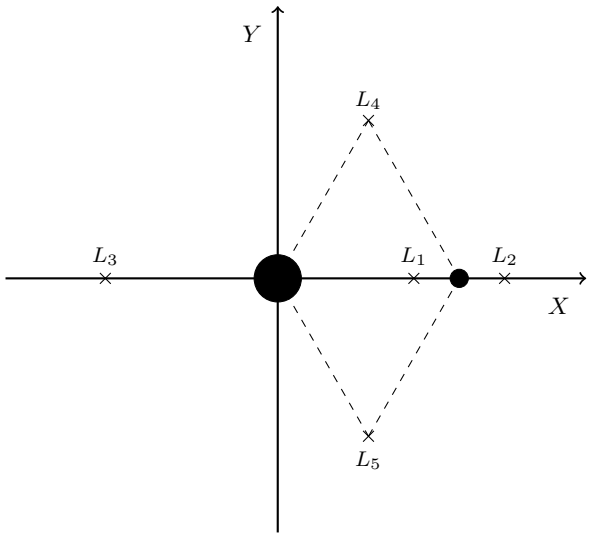

Figure 1.2: Location of the Lagrangian equilibrium points in the XY plane.

1.3a) there are three disconnected parts of the admissible realm that are confined around P_1, P_2, and in the exterior of the P_1–P_2 system respectively; hence for such values of $\mathcal{J}$, it is not possible to transfer a spacecraft from one region to another one without changing the value of the Jacobi constant via a propulsion system. As a matter of fact, by increasing the value of $\mathcal{J}$ we observe that for $\mathcal{J} = J_{L_1}$ the forbidden realm of motion shrinks in L_1 (panel 1.3b) and for $\mathcal{J} \in (\mathcal{J}_{L_1}, \mathcal{J}_{L_2})$ the two admissible regions surrounding P_1 and P_2 are connected by a channel which opens at L_1 (panel 1.3c). For such values of $\mathcal{J}$, a spacecraft leaving, for example P_2, can pass around P_1 without consumption of propellant. For $\mathcal{J} = \mathcal{J}_{L_2}$ the forbidden real of motion shrinks in L_2 (panel 1.3d) and for $\mathcal{J} \in (\mathcal{J}_{L_2}, \mathcal{J}_{L_3})$ the admissible region surrounding P_1 and P_2 is connected to the external region of the P_1–P_2 system (panel 1.3e). For such values a spacecraft can transit from the external region to P_1 or P_2 and vice versa. For $\mathcal{J} = \mathcal{J}_{L_3}$ the forbidden region shrinks in L_3 (panel 1.3f) and for $\mathcal{J} \in (\mathcal{J}_{L_3}, \mathcal{J}_{L_4})$ shrinks in L_4 and L_5 (panels 1.4a and 1.4b). For $\mathcal{J} > \mathcal{J}_{L_4}$ the admissible region extends to the whole Cartesian plane. We underline that $\mathcal{J}_{L_1}$ and $\mathcal{J}_{L_2}$ are the limit values for two different types of transits: those leaving P_1 and arriving to P_2 (or vice versa), and those leaving (or arriving) the P_1–P_2 system. For such reason the values of the constant of motion computed at L_1 and L_2 are so important in connection to astrodynamics and space flight dynamics.

1.1.3 Periodic orbits around the collinear equilibria

The simplest analysis of the dynamics close to an equilibrium point is provided by the linearization of the equations of motion at the equilibrium itself. The linearization at a collinear Lagrangian point L_i (in this Section we limit our discussion to the collinear points L_1, L_2, L_3, which are partially hyperbolic) is more conveniently performed using the Hamiltonian formulation. By considering the Hamiltonian (1.9), the collinear points are mapped to the phase-space points

$$(X_{L_i}, Y_{L_i}, P_{X,L_i}, P_{Y,L_i}) = (X_{L_i}, 0, 0, X_{L_i}). \tag{1.22}$$

Then, we introduce the variables $(\boldsymbol{q}, \boldsymbol{p}) = (q_1, q_2, p_1, p_2)$ by translation at L_i:

$$q_1 = X - X_{L_i}, \quad q_2 = Y, \quad p_1 = P_X, \quad p_2 = P_Y - X_{L_i} \tag{1.23}$$

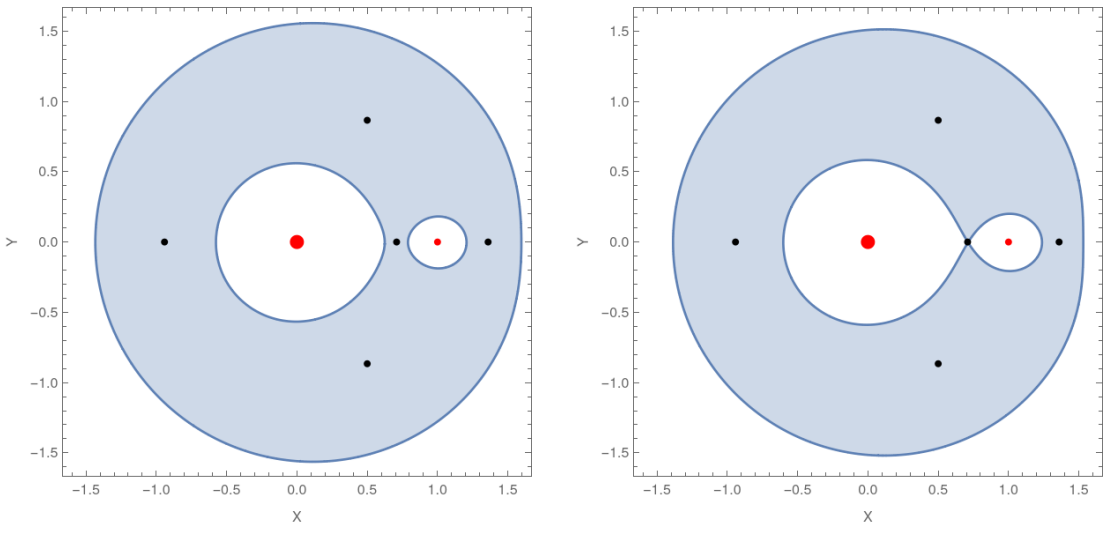

(a) $\mathcal{J} < \mathcal{J}_{L_1}$.

(b) $\mathcal{J} = \mathcal{J}_{L_1}$.

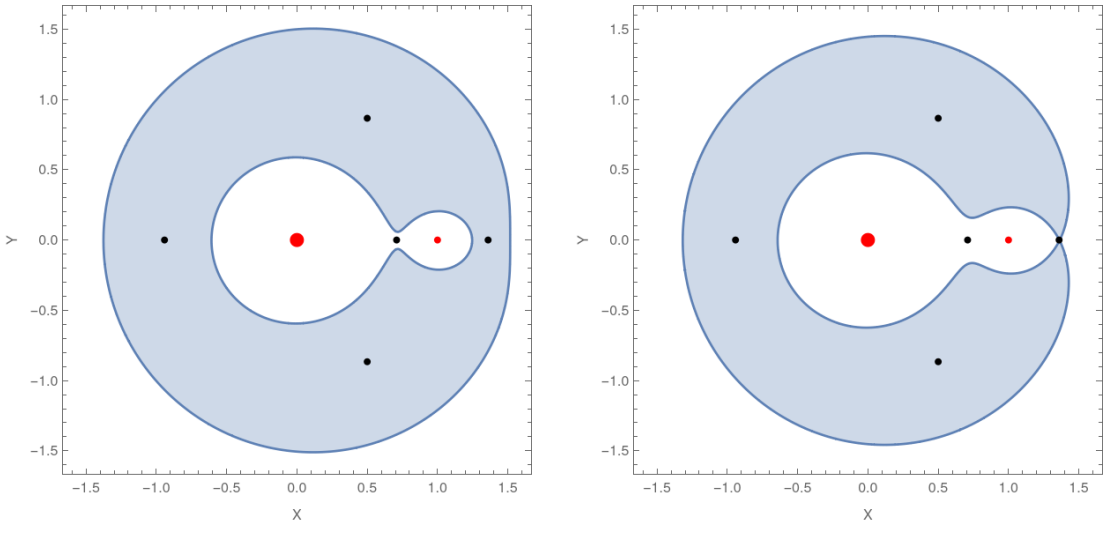

(c) $\mathcal{J} \in (\mathcal{J}_{L_1}, \mathcal{J}_{L_2})$.

(d) $\mathcal{J} = \mathcal{J}_{L_2}$.

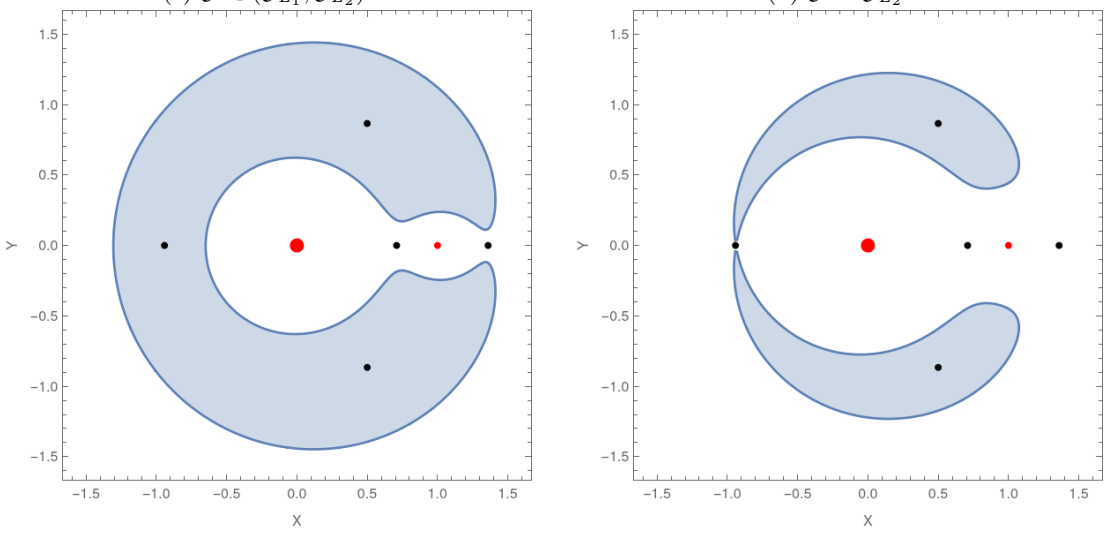

(e) $\mathcal{J} \in (\mathcal{J}_{L_2}, \mathcal{J}_{L_3})$.

(f) $\mathcal{J} = \mathcal{J}_{L_3}$.

Figure 1.3: Representation of the admissible (white) and forbidden (gray) regions for different values of the constant of motion $\mathcal{J}$ in the CR3BP characterized by $\varepsilon_2 = 0.1$. The black points represent the location of the Lagrange points, while the red points represent the position of the bodies P_1 and P_2. The border of the admissible regions (dark gray curve) represent the zero velocity curves.

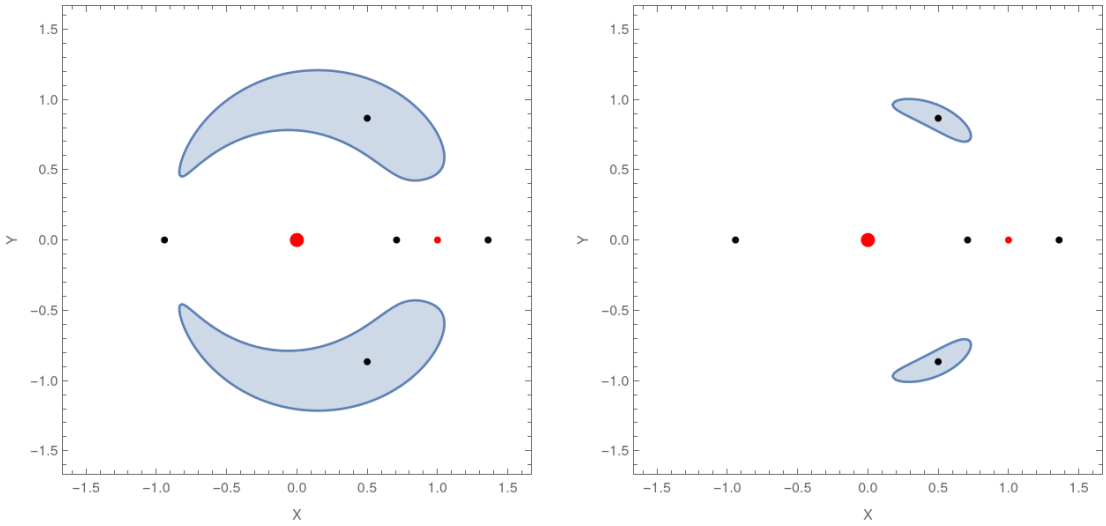

(a) $\mathcal{J} = \mathcal{J}^* \in (\mathcal{J}_{L_3}, \mathcal{J}_{L_4})$. (b) $\mathcal{J} \in (\mathcal{J}^*, \mathcal{J}_{L_4})$.

Figure 1.4: Representation of the admissible (white) and forbidden (gray) regions for different values of the constant of motion $\mathcal{J}$ in the interval $(\mathcal{J}_{L_3}, \mathcal{J}_{L_4})$ in the CR3BP characterized by $\varepsilon_2 = 0.1$. The black points represent the location of the Lagrange points, while the red points represent the position of the bodies P_1 and P_2. The border of the admissible regions (dark gray curve) represent the zero velocity curves.

and the Hamiltonian

$$H(\boldsymbol{q}, \boldsymbol{p}) = \mathcal{H}(q_1 + X_{L_i}, q_2, p_1, p_2 + X_{L_i}) \tag{1.24}$$

conjugate to $\mathcal{H}$ by the transformation (1.23). Next, we expand H at $(\boldsymbol{q}, \boldsymbol{p}) = (\boldsymbol{0}, \boldsymbol{0})$. By dropping the constant term $H(\boldsymbol{0}, \boldsymbol{0})$, and since the term of first order vanishes because $(\boldsymbol{0}, \boldsymbol{0})$ is an equilibrium point, we obtain

$$H(\boldsymbol{q}, \boldsymbol{p}) = H_2(\boldsymbol{q}, \boldsymbol{p}) + H_3(\boldsymbol{q}, \boldsymbol{p}) + \ldots = \sum_{\alpha \geq 2} H_\alpha(\boldsymbol{q}, \boldsymbol{p}) \tag{1.25}$$

where H_α is a polynomial of degree α in the variables $\boldsymbol{q}$ and $\boldsymbol{p}$. The linearization of the Hamilton equations of $H(\boldsymbol{q}, \boldsymbol{p})$

$$\dot{q}_1 = \frac{\partial H}{\partial p_1}, \quad \dot{q}_2 = \frac{\partial H}{\partial p_2}, \quad \dot{p}_1 = -\frac{\partial H}{\partial q_1}, \quad \dot{p}_2 = -\frac{\partial H}{\partial q_2} \tag{1.26}$$

at the equilibrium $(\boldsymbol{q}, \boldsymbol{p}) = (\boldsymbol{0}, \boldsymbol{0})$, are the Hamilton equations of

$$H_2(\boldsymbol{q}, \boldsymbol{p}) = \frac{p_1^2 + p_2^2}{2} + q_2 p_1 - q_1 p_2 + \gamma \left(\frac{q_2^2}{2} - q_1^2 \right), \quad \gamma = \frac{1 - \varepsilon_2}{|X_{L_i}^3|} - \frac{\varepsilon_2}{|X_{L_i} - 1|^3} \tag{1.27}$$

which are also represented by the linear system

$$\begin{pmatrix} \dot{\boldsymbol{q}} \\ \dot{\boldsymbol{p}} \end{pmatrix} = A \begin{pmatrix} \boldsymbol{q} \\ \boldsymbol{p} \end{pmatrix} \qquad A = \begin{pmatrix} 0 & 1 & 1 & 0 \\ -1 & 0 & 0 & 1 \\ 2\gamma & 0 & 0 & 1 \\ 0 & -\gamma & -1 & 0 \end{pmatrix}. \tag{1.28}$$

For the Lagrangian points L_1, L_2, and L_3 the matrix A has two complex eigenvalues which we denote by $\pm i\sigma$ and two opposite real eigenvalues which we denote by $\pm\lambda$. Therefore, they are partially hyperbolic, since the real couple is related to an hyperbolic motion, while the complex

couple is related to an elliptic motion. The partially hyperbolic nature of L_1, L_2, and L_3 is well represented by the existence of a canonical linear transformation (for further details, the reader is referred to Jorba, 2012)

$$(\boldsymbol{q}, \boldsymbol{p}) = \mathcal{C}(\boldsymbol{Q}, \boldsymbol{P}) \tag{1.29}$$

conjugating H_2 to

$$K_2(\boldsymbol{Q}, \boldsymbol{P}) = \sigma \frac{Q_1^2 + P_1^2}{2} + \lambda Q_2 P_2. \tag{1.30}$$

The reader is referred to Fig. 1.5 for a schematic representation of the phase-portrait in the $\boldsymbol{QP}$ phase-space. The flow approximated by the normal form (1.30) has

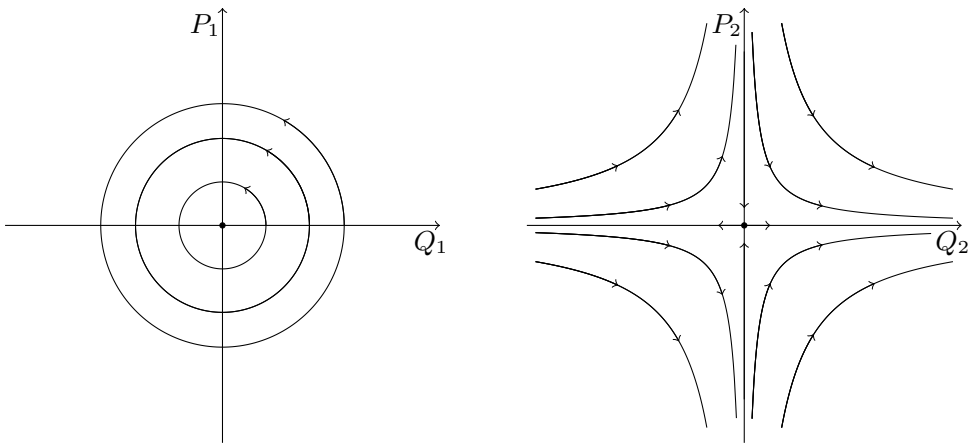

Figure 1.5: In the linear approximation, the phase-space $(\boldsymbol{Q}, \boldsymbol{P})$ is decomposed by an harmonic oscillator component (described by the Q_1 and P_1 variables), and an hyperbolic expansion/contraction (described by the Q_2 and P_2 variables).

a) an equilibrium point at $(Q_1, P_1, Q_2, P_2) = (0, 0, 0, 0)$;

b) a family of periodic orbits identified by

$$Q_1 = \sqrt{2I_1}\sin\phi_1, \quad P_1 = \sqrt{2I_1}\cos\phi_1, \quad Q_2 = 0, \quad P_2 = 0 \text{ where } I_1 > 0, \phi_1 \in [0, 2\pi]; \tag{1.31}$$

c) for any periodic orbit of the family b), there exists a set of initial data converging in the future to the periodic orbit; such a set is called the local stable manifold, and it is identified by

$$Q_1 = \sqrt{2I_1}\sin\phi_1, \quad P_1 = \sqrt{2I_1}\cos\phi_1, \quad Q_2 = 0, \quad |P_2| \in (0, \epsilon), \tag{1.32}$$

for ϵ suitably small;

d) for any periodic orbit of the family b), there exists a set of initial data converging in the past to the periodic orbit; such a set is called the local unstable manifold, and it is identified by

$$Q_1 = \sqrt{2I_1}\sin\phi_1, \quad P_1 = \sqrt{2I_1}\cos\phi_1, \quad P_2 = 0, \quad |Q_2| \in (0, \epsilon), \tag{1.33}$$

for ϵ suitably small;

e) for any periodic orbit, there exists a set of initial data that are inside the stable (or unstable) manifold tube but transit from right to left, and vice versa, of the periodic orbit. Such a set

of orbits are called the transit orbits, and are identified by

$$Q_1 = \sqrt{2I_1}\sin\phi_1, \quad P_1 = \sqrt{2I_1}\cos\phi_1, \quad Q_2P_2 > 0. \tag{1.34}$$

Birkhoff normalization allows to extend to higher orders the description of the motions obtained with $H_2(\boldsymbol{Q},\boldsymbol{P})$ so that the periodic orbits generalize to the planar Lyapunov orbits, and the manifolds asymptotic to them are the stable and unstable manifold tubes. In Sec. 1.3.4 we will discuss how to define a canonical transformation:

$$(\boldsymbol{q},\boldsymbol{p}) = \mathcal{C}(\boldsymbol{Q},\boldsymbol{P}) \tag{1.35}$$

which conjugates the Hamiltonian (1.25) to an Hamiltonian of the form:

$$K(\boldsymbol{Q},\boldsymbol{P}) = \sum_{\nu=1}^{N/2} K_{2\nu}(\boldsymbol{Q},\boldsymbol{P}) + R_{N+1}(\boldsymbol{Q},\boldsymbol{P}) \tag{1.36}$$

where

- $K_{2\nu}(\boldsymbol{Q},\boldsymbol{P})$ denotes a polynomial of degree 2ν depending on the variables $\boldsymbol{Q}$ and $\boldsymbol{P}$ through the combinations of the terms $(Q_1^2+P_1^2)/2$ and Q_2P_2;
- the remainder R_{N+1} is a polynomial of order $N+1$ in the variables $\boldsymbol{Q}$ and $\boldsymbol{P}$.

In a neighbourhood of the equilibrium $(\boldsymbol{Q},\boldsymbol{P}) = (\boldsymbol{0},\boldsymbol{0})$ of radius D:

$$B(D) = \{(\boldsymbol{Q},\boldsymbol{P}) : |\boldsymbol{Q}|, |\boldsymbol{P}| \le D\} \tag{1.37}$$

the remainder R_{N+1} is estimated by

$$\|R_{N+1}\| \le C_{N+1}D^{N+1} \tag{1.38}$$

and therefore, if D is suitably small, in the set $B(D)$ we consider the approximate Hamiltonian

$$\tilde{K}(\boldsymbol{Q},\boldsymbol{P}) = \sum_{\nu=1}^{N/2} K_{2\nu}(\boldsymbol{Q},\boldsymbol{P}) \tag{1.39}$$

whose flow is easily computed explicitly. In particular, the actions

$$I_1 = \frac{Q_1^2+P_1^2}{2}, \quad I_2 = Q_2P_2 \tag{1.40}$$

are first integrals for the flow of $\tilde{K}$ and for $Q_2, P_2 = 0$ we have a family of periodic orbits that are identified by $Q_1 = \sqrt{2I_1}\sin\phi_1$, $P_1 = \sqrt{2I_1}\cos\phi_1$, $I_1 > 0$ and $\phi_1 \in [0, 2\pi]$. Such periodic orbits admit local stable manifold identified by $Q_1 = \sqrt{2I_1}\sin\phi_1$, $P_1 = \sqrt{2I_1}\cos\phi_1$, $Q_2 = 0$ and $P_2 \neq 0$ suitably small, and local unstable manifold identified by $Q_1 = \sqrt{2I_1}\sin\phi_1$, $P_1 = \sqrt{2I_1}\cos\phi_1$, $P_2 = 0$ and $Q_2 \neq 0$ suitably small. When we map back the periodic orbits and their stable and unstable manifolds to the original Cartesian variables of the co-rotating reference frame we obtain the non-linear approximations of the:

- *planar Lyapunov orbit* $\mathcal{LL}_i(I_1)$:

$$\mathcal{LL}_i(I_1) = \bigcup_{\phi_1 \in [0,2\pi]} \{(X, Y, P_X, P_Y) = (X_{L_i}, 0, 0, X_{L_i}) + \mathcal{C}(\boldsymbol{Q}, \boldsymbol{P}) : \\ (Q_1, P_1) = \sqrt{2I_1}(\sin\phi_1, \cos\phi_1), Q_2, P_2 = 0\}; \tag{1.41}$$

- local stable manifold of $\mathcal{LL}_i(I_1)$:

$$\mathcal{W}^{s,loc}_{I_1} = \bigcup_{\phi_1 \in [0,2\pi]} \{(X, Y, P_X, P_Y) = (X_{L_i}, 0, 0, X_{L_i}) + \mathcal{C}(\boldsymbol{Q}, \boldsymbol{P}) : \\ (Q_1, P_1) = \sqrt{2I_1}(\sin\phi_1, \cos\phi_1), Q_2 = 0, |P_2| \in (0, \epsilon)\} \tag{1.42}$$

where ϵ is such that $\boldsymbol{Q}, \boldsymbol{P}$ is in the domain of the transformation $\mathcal{C}(\boldsymbol{Q}, \boldsymbol{P})$;

- local unstable manifold of $\mathcal{LL}_i(I_1)$:

$$\mathcal{W}^{u,loc}_{I_1} = \bigcup_{\phi_1 \in [0,2\pi]} \{(X, Y, P_X, P_Y) = (X_{L_i}, 0, 0, X_{L_i}) + \mathcal{C}(\boldsymbol{Q}, \boldsymbol{P}) : \\ (Q_1, P_1) = \sqrt{2I_1}(\sin\phi_1, \cos\phi_1), P_2 = 0, |Q_2| \in (0, \epsilon)\} \tag{1.43}$$

where ϵ is such that $\boldsymbol{Q}, \boldsymbol{P}$ is in the domain of the transformation $\mathcal{C}(\boldsymbol{Q}, \boldsymbol{P})$.

When we propagate the initial conditions in $\mathcal{W}^{s,loc}_{I_1}$ and $\mathcal{W}^{u,loc}_{I_1}$ with the flow of the CR3BP backward and forward in time respectively we obtain the global stable and unstable manifolds $\mathcal{W}^{s}_{I_1}$ and $\mathcal{W}^{u}_{I_1}$, also called the *manifold tubes*.

The manifold tubes of the Lyapunov orbits associated to L_1 and L_2 have been widely investigated in connection to transport phenomena, close encounters, and space mission design (see, for example, Conley, 1968; Howell et al., 1997, 1998; Koon et al., 2008; Gómez et al., 2001; Dunham and Farquhar, 2003; Gómez et al., 2004; Topputo et al., 2005; Guzzo, 2010; Belló et al., 2010; Simó, 2010; Ren et al., 2012; Guzzo and Lega, 2013; Parker and Anderson, 2013; Lega and Guzzo, 2016b; Guzzo and Lega, 2018). Several space missions, such as SOHO, ISEE-3, WMAP, Herschel and Planck, were designed to reach the vicinity of the Sun–Earth L_1 and L_2 equilibrium points. A modern concept of mission design, called *space manifold dynamics*, exploits the solutions originating at the Lagrangian points, and determine new trajectories and optimal transfers that can not be found in the two-body approximation (Conley, 1968; Gómez et al., 1993; Koon et al., 2001; Belló et al., 2010). In particular, we recall that for values of the constant of motion $\mathcal{J} \geq J_{L_1}$, transfers between the primaries are possible. Since the latter require a minimal fuel consumption, they are also called *low-energy transfers*.

We remark that to transfer a spacecraft from one planet to another, there exists another kind of orbital transfers that are based on gravity assist. Such a transfer differs from the low-energy transfer since it requires a delta-v sufficiently high to escape from the sphere of influence of the planet. For further details about the gravity assists, the reader is referred to Strange and Longuski (2002); Miller and Weeks (2002); Campagnola and Russell (2010a,b).

1.2 The planar elliptic restricted three-body problem

1.2.1 Equations of motion

The elliptic restricted three-body problem (ER3BP) deals with the study of the dynamics of a body P of negligible mass that is gravitationally attracted by two massive bodies P_1 and P_2 which perform an elliptic motion with eccentricity e_2. To compare the solutions of the ER3BP with those of the CR3BP it is useful to introduce a rotating-pulsating reference frame OXY (for further details the reader is referred to Szebehely, 1967), and to use the standard unit of the system P_1-P_2 (i.e. the sum of the gravitational parameters of P_1 and P_2 is one, the semi-major axis of P_2 is one). By denoting with $\boldsymbol{r} = \boldsymbol{P}_2 - \boldsymbol{P}_1$ the relative position vector of P_2 with respect to P_1, the heliocentric rotating-pulsating reference frame OXY is centered at P_1, and its axes are parallel to the unit vectors

$$\boldsymbol{u}_r = \frac{\boldsymbol{r}}{\|\boldsymbol{r}\|}, \quad \boldsymbol{u}_t = \frac{\boldsymbol{r} \times \boldsymbol{u}_n}{\|\boldsymbol{r} \times \boldsymbol{u}_n\|}, \tag{1.44}$$

where $\boldsymbol{u}_n = \frac{\dot{\boldsymbol{r}} \times \boldsymbol{r}}{\|\dot{\boldsymbol{r}} \times \boldsymbol{r}\|}$; in such a reference frame, P_1 is at the origin and P_2 is located at $(0, 1)$. The equations of motion of P in the OXY reference frame are conveniently expressed in Hamiltonian form using the true anomaly f_2 of the elliptic motion of P_2 as an independent variable of the Hamilton equations. Precisely, the Hamilton function of the ER3BP in the heliocentric rotating-pulsating reference frame is

$$\begin{aligned}\mathcal{H}(X, Y, P_X, P_Y, f_2; \varepsilon_2, e_2) =& \frac{1}{2}\left[(P_X + Y)^2 + (P_Y - X)^2\right] - \frac{1}{1 + e_2 \cos f_2}\left[\frac{X^2 + Y^2}{2} + \frac{1}{\sqrt{X^2 + Y^2}}\right] \\ &+ \frac{\varepsilon_2}{1 + e_2 \cos f_2}\left(X + \frac{1}{\sqrt{X^2 + Y^2}} - \frac{1}{\sqrt{(X-1)^2 + Y^2}}\right)\end{aligned} \tag{1.45}$$

where ε_2 denotes the gravitational parameter of P_2, and P_X and P_Y represent the conjugate momenta to X and Y respectively. We remark that the Hamiltonian is not autonomous since it depends explicitly on the true anomaly f_2, which is the independent variable of the Hamilton's equations

$$\frac{dX}{df_2} = \frac{\partial \mathcal{H}}{\partial P_X}, \quad \frac{dY}{df_2} = \frac{\partial \mathcal{H}}{\partial P_Y}, \quad \frac{dP_X}{df_2} = -\frac{\partial \mathcal{H}}{\partial X}, \quad \frac{dP_Y}{df_2} = -\frac{\partial \mathcal{H}}{\partial Y}, \tag{1.46}$$

i.e.

$$\begin{aligned}\frac{dX}{df_2} &= P_X + Y \\ \frac{dY}{df_2} &= P_Y - X \\ \frac{dP_X}{df_2} &= P_Y - X + \frac{1}{1 + e_2 \cos f_2}\left[X - (1 - \varepsilon_2)\frac{X}{(X^2 + Y^2)^{3/2}} - \varepsilon_2\left(1 + \frac{X - 1}{((X-1)^2 + Y^2)^{3/2}}\right)\right] \\ \frac{dP_Y}{df_2} &= -P_X - Y + \frac{Y}{1 + e_2 \cos f_2}\left(1 - \frac{\varepsilon_2}{((X-1)^2 + Y^2)^{3/2}} - \frac{1 - \varepsilon_2}{(X^2 + Y^2)^{3/2}}\right).\end{aligned} \tag{1.47}$$

The advantage of the rotating-pulsating reference frame, is that the Hamiltonian system (1.46) has five equilibrium points $L_1, \ldots, L_5$ in the same location of the Lagrangian points computed in the

corresponding CR3BP.

1.2.2 The difficulties in the study of the ER3BP

The effects that the eccentricity of P_2 have on the dynamics of the body with negligible mass have been studied by using both analytical and numerical methods (as example, the reader is referred to Szebehely and Giacaglia, 1964; Broucke, 1969; Llibre and Piñol, 1990; Howell and Hiday-Johnston, 1994; Hiday-Johnston and Howell, 1994; de Almeida Prado, 1997; Palacián et al., 2006; Lhotka et al., 2008; Gawlik et al., 2009; Hyeraci and Topputo, 2010; Capinski et al., 2016; Peng et al., 2017; Ferrari and Lavagna, 2018; Qi and de Ruiter, 2018; de Almeida Prado and Neto, 2006; Hou and Liu, 2011; Peng and Xu, 2015; Ferreira et al., 2018; Paez and Guzzo, 2021). Although the ER3BP admits the same equilibria of the CR3BP, the study of the solutions originating at these Lagrangian points is more difficult with respect to the CR3BP: this mainly because no constants of motion (such as the Jacobi constant) are known, and the application of the perturbations theory is complicated by the fact that the expansion of the Hamiltonian $\mathcal{H}$ at L_1 and L_2 is non-autonomous already at order two. Thus, a Floquet theory is necessary in order to have an Hamiltonian with quadratic part which is autonomous, and then to Birkhoff normalize the normal form. The Floquet-Birkhoff normalization of the ER3BP has been recently done by Paez and Guzzo (2021). With these Floquet-Birkhoff normal forms, the authors constructed a quasi-integral of motion, locally defined in a neighbourhood of L_1 and L_2; the analog of zero velocity curves have been defined as well as the extensions of the planar Lyapunov orbits to planar Lyapunov tori, with their stable and unstable manifolds. We will define and discuss the properties of these dynamical structures in Chapter 3, Sec. 1.3.5. Before, we need to review the basic ideas and techniques of Hamiltonian perturbation theory.

1.3 Hamiltonian perturbation theory

Hamiltonian perturbation theory aims to study those systems whose Hamilton function is nearly integrable. In Celestial Mechanics, the most famous nearly integrable system is represented by the CR3BP, that is a perturbation of the two-body problem. Several theories were developed to analyze nearly integrable systems; in this Section, we provide an overview about the most famous and useful techniques for the study of nearly integrable system, such as the Lie series, the Floquet canonical theory, and the Birkhoff normal forms. For further details about the Hamiltonian perturbation theory, the reader is referred to Poincaré (1892); Arnold (1989); Arnold et al. (1993); Benettin (2004).

1.3.1 Quasi-integrable integrable systems

Let us consider the Hamiltonian

$$\mathcal{H}(\boldsymbol{I}, \boldsymbol{\varphi}) = H(\boldsymbol{I}) + \varepsilon \mathcal{P}(\boldsymbol{I}, \boldsymbol{\varphi}) \tag{1.48}$$

where $\boldsymbol{I} := (I_1, \ldots, I_n)$, $\boldsymbol{\varphi} := (\varphi_1, \ldots, \varphi_n)$ are the action-angle variables, ε is a parameter, and $\mathcal{P}$ is the perturbing function which depends periodically on each angle φ_j. It is convenient to represent $\mathcal{P}$ as:

$$\mathcal{P}(\boldsymbol{I}, \boldsymbol{\varphi}) = \overline{\mathcal{P}}(\boldsymbol{I}) + \hat{\mathcal{P}}(\boldsymbol{I}, \boldsymbol{\varphi}) \tag{1.49}$$

where the Fourier average of $\hat{\mathcal{P}}$ is equal to zero. Hamiltonian systems of the form (1.48) are called *quasi-integrable*. It is natural to consider how much the solutions of (1.48) are different from those of the integrable system of Hamiltonian $H(\boldsymbol{I})$, which are characterized by constant value of the actions. Standard estimates (called *a priori estimates*) provide

$$|I_j(t) - I_j(t_0)| \leq C\varepsilon|t - t_0| \tag{1.50}$$

where:

$$C := \sup_{(\boldsymbol{I},\boldsymbol{\varphi})} \max_{j\in\{1,\dots,n\}} \left|\frac{\partial \mathcal{P}}{\partial \varphi_j}(\boldsymbol{I},\boldsymbol{\varphi})\right|. \tag{1.51}$$

Hence, the actions can drift away from their initial data $\boldsymbol{I}(t_0)$ only after time-spans of order ε^{-1}.

The aim of the Hamiltonian perturbation theory is to study the evolution of the action-angle variables for time-spans longer than $1/\varepsilon$. Since Poincaré, the main approach to this study is to construct a canonical transformation w close to the identity, i.e. $(\boldsymbol{I},\boldsymbol{\varphi}) = w(\tilde{\boldsymbol{I}},\tilde{\boldsymbol{\varphi}}) = (\tilde{\boldsymbol{I}},\tilde{\boldsymbol{\varphi}}) + \mathcal{O}(\varepsilon)$ conjugating the Hamiltonian (1.48) to

$$\tilde{\mathcal{H}}(\tilde{\boldsymbol{I}},\tilde{\boldsymbol{\varphi}}) = H(\tilde{\boldsymbol{I}}) + \varepsilon\overline{\mathcal{P}}(\tilde{\boldsymbol{I}}) + \varepsilon^2\mathcal{R}(\tilde{\boldsymbol{I}},\tilde{\boldsymbol{\varphi}},\varepsilon). \tag{1.52}$$

If such a transformation exists, the time evolution of the new actions satisfies the estimate:

$$|\tilde{I}_j(t) - \tilde{I}_j(t_0)| \leq \varepsilon^2\tilde{C}|t - t_0|, \tag{1.53}$$

where $\tilde{C} := \sup_{(\tilde{\boldsymbol{I}},\tilde{\boldsymbol{\varphi}})} \max_{j\in\{1,\dots,n\}} \left|\frac{\partial \mathcal{R}}{\partial \tilde{\varphi}_j}(\tilde{\boldsymbol{I}},\tilde{\boldsymbol{\varphi}},\varepsilon)\right|$.

In a broad sense, discussions about the existence of such a transformation, as well as its iteration, lead to the most important results of modern perturbations theories, such as the KAM and Nekhoroshev theorems.

1.3.2 The Lie series method

Near to the identity canonical transformations can be explicitly generated using the so called *Lie series method*. In this method, the canonical transformation is defined by the Hamiltonian flow at time ε of a Hamilton function $\chi(\boldsymbol{I},\boldsymbol{\varphi})$ with initial conditions $(\tilde{\boldsymbol{I}},\tilde{\boldsymbol{\varphi}})$, i.e. $(\boldsymbol{I},\boldsymbol{\varphi}) = \Phi^{\varepsilon}_{\chi}(\tilde{\boldsymbol{I}},\tilde{\boldsymbol{\varphi}})$; the Hamiltonian function χ is usually called *generating function*. Therefore, given $\chi(\boldsymbol{I},\boldsymbol{\varphi})$, we first denote by $(\hat{\boldsymbol{I}}(s),\hat{\boldsymbol{\varphi}}(s))$ the solutions of the Hamilton equations of χ with initial conditions $(\tilde{\boldsymbol{I}},\tilde{\boldsymbol{\varphi}})$, i.e.

$$(\hat{\boldsymbol{I}}(0),\hat{\boldsymbol{\varphi}}(0)) = (\tilde{\boldsymbol{I}},\tilde{\boldsymbol{\varphi}}). \tag{1.54}$$

Next, for any function $f(\boldsymbol{I},\boldsymbol{\varphi})$, we denote by: $f^s(\tilde{\boldsymbol{I}},\tilde{\boldsymbol{\varphi}}) = f(\hat{\boldsymbol{I}}(s),\hat{\boldsymbol{\varphi}}(s))$ the composition of f with the flow of χ. We have:

$$\frac{df^s}{ds} = \frac{df^s}{d\hat{\boldsymbol{I}}}\cdot\frac{d\hat{\boldsymbol{I}}}{ds} + \frac{df^s}{d\hat{\boldsymbol{\varphi}}}\cdot\frac{d\hat{\boldsymbol{\varphi}}}{ds} = \frac{df^s}{d\hat{\boldsymbol{\varphi}}}\cdot\frac{\partial\chi}{\partial\hat{\boldsymbol{I}}} - \frac{df^s}{d\hat{\boldsymbol{I}}}\cdot\frac{\partial\chi}{\partial\hat{\boldsymbol{\varphi}}} = \{f^s,\chi\} \tag{1.55}$$

$$\frac{d^2f^s}{ds^2} = \left\{\frac{df^s}{ds},\chi\right\} = \{\{f^s,\chi\},\chi\} \tag{1.56}$$

as well as:

$$\frac{d^i f^s}{ds^i} = \left\{ \frac{d^{(i-1)} f^s}{ds^{(i-1)}}, \chi \right\}, \quad i \geq 2 \tag{1.57}$$

By introducing the Lie derivative $\mathcal{L}$ such that

$$\mathcal{L}^0_\chi f := f, \qquad \mathcal{L}^i_\chi f := \mathcal{L}^1_\chi \left(\mathcal{L}^{(i-1)}_\chi f \right) \qquad i \geq 1, \tag{1.58}$$

the relation (1.57) computed at $s = 0$ provides:

$$\left. \frac{d^i f^s}{ds^i} \right|_{s=0} = \mathcal{L}^i_\chi f. \tag{1.59}$$

By applying the previous formulas to compute the Taylor expansion of f^ε, we have:

$$f(\phi^\varepsilon_\chi(\tilde{\boldsymbol{I}}, \tilde{\boldsymbol{\varphi}})) = f^\varepsilon = \sum_{i=0}^{\infty} \frac{\varepsilon^i}{i!} \mathcal{L}^i_\chi f(\tilde{\boldsymbol{I}}, \tilde{\boldsymbol{\varphi}}). \tag{1.60}$$

The right-hand side of Eq. (1.60) is called the *Lie series* of $f(\boldsymbol{I}, \boldsymbol{\varphi})$. In such a way the canonical transformation $(\boldsymbol{I}, \boldsymbol{\varphi}) = \Phi^\varepsilon_\chi(\tilde{\boldsymbol{I}}, \tilde{\boldsymbol{\varphi}})$ is also explicitly represented by

$$\begin{aligned} I_j &= \tilde{I}_j + \varepsilon\{\tilde{I}_j, \chi\} + \frac{\varepsilon^2}{2}\{\{\tilde{I}_j, \chi\}, \chi\} + \dots \\ \varphi_j &= \tilde{\varphi}_j + \varepsilon\{\tilde{\varphi}_j, \chi\} + \frac{\varepsilon^2}{2}\{\{\tilde{\varphi}_j, \chi\}, \chi\} + \dots \end{aligned} \qquad j \in 1, \dots, n, \tag{1.61}$$

and the Hamilton function $\mathcal{H}$ is conjugate to

$$\tilde{\mathcal{H}}(\tilde{\boldsymbol{I}}, \tilde{\boldsymbol{\varphi}}) := \mathcal{H} \circ \Phi^\varepsilon_\chi = \mathcal{H}(\tilde{\boldsymbol{I}}, \tilde{\boldsymbol{\varphi}}) + \varepsilon\{\mathcal{H}, \chi\}(\tilde{\boldsymbol{I}}, \tilde{\boldsymbol{\varphi}}) + \frac{\varepsilon^2}{2}\{\{\mathcal{H}, \chi\}, \chi\} + \dots \tag{1.62}$$

Since $\mathcal{H}$ itself depends on ε, we replace in (1.62) the Hamiltonian $\mathcal{H}$ with the right-hand side of (1.48), and we rearrange in the Lie series the terms with the same power of ε. We obtain the expansion:

$$\tilde{\mathcal{H}} = H(\boldsymbol{I}) + \varepsilon \left[\overline{\mathcal{P}} + \hat{\mathcal{P}} - \boldsymbol{\omega}(\boldsymbol{I}) \cdot \frac{\partial \chi}{\partial \boldsymbol{\varphi}} \right] + \mathcal{O}(\varepsilon^2) \tag{1.63}$$

where $\boldsymbol{\omega}(\boldsymbol{I}) = \frac{\partial H}{\partial \boldsymbol{I}}(\boldsymbol{I})$.

In order to accomplish the requirement that the Hamiltonian (1.63) is in the form (1.52), we need a generating function $\chi(\boldsymbol{I}, \boldsymbol{\varphi})$ satisfying the so called *fundamental equation of perturbation theory*[1]:

$$\boldsymbol{\omega}(\tilde{\boldsymbol{I}}) \cdot \frac{\partial \chi}{\partial \tilde{\boldsymbol{\varphi}}} = \hat{\mathcal{P}}(\tilde{\boldsymbol{I}}, \tilde{\boldsymbol{\varphi}}). \tag{1.64}$$

Since both $\mathcal{P}$ and χ can be expressed as a Fourier series, i.e.

$$\mathcal{P}(\tilde{\boldsymbol{I}}, \tilde{\boldsymbol{\varphi}}) = \sum_{\boldsymbol{k} \in \mathbb{Z}^n} \hat{P}_{\boldsymbol{k}}(\tilde{\boldsymbol{I}}) e^{i\boldsymbol{k} \cdot \tilde{\boldsymbol{\varphi}}}, \qquad \chi(\tilde{\boldsymbol{I}}, \tilde{\boldsymbol{\varphi}}) = \sum_{\boldsymbol{k} \in \mathbb{Z}^n} \hat{\chi}_{\boldsymbol{k}}(\tilde{\boldsymbol{I}}) e^{i\boldsymbol{k} \cdot \tilde{\boldsymbol{\varphi}}}, \tag{1.65}$$

Eq. (1.64) becomes:

$$\sum_{\boldsymbol{k} \in \mathbb{Z}^n} i \left(\boldsymbol{\omega}(\tilde{\boldsymbol{I}}) \cdot \boldsymbol{k} \right) \hat{\chi}_{\boldsymbol{k}}(\tilde{\boldsymbol{I}}) e^{i\boldsymbol{k} \cdot \tilde{\boldsymbol{\varphi}}} = \sum_{\boldsymbol{k} \in \mathbb{Z}^n \setminus \boldsymbol{0}} \hat{P}_{\boldsymbol{k}}(\tilde{\boldsymbol{I}}) e^{i\boldsymbol{k} \cdot \boldsymbol{\varphi}} \tag{1.66}$$

[1] The fundamental equation of perturbation theory is usually known as *homological equation*.

which is formally solved by

$$\chi_{\mathbf{0}}(\tilde{\boldsymbol{I}}) = 0, \qquad \chi_{\boldsymbol{k}}(\tilde{\boldsymbol{I}}) = \frac{\hat{P}_{\boldsymbol{k}}(\tilde{\boldsymbol{I}})}{i\boldsymbol{k}\cdot\boldsymbol{\omega}(\tilde{\boldsymbol{I}})} \qquad \text{for } \boldsymbol{k} \neq \mathbf{0}. \tag{1.67}$$

As it is well known since Poincaré, if the Hamiltonian $\mathcal{H}$ satisfies some genericity properties, the Fourier series defined by the coefficients of Eq. (1.67) do not sum to a regular function in any open domain of the actions space. The reason is due to the denominators which vanish for each $\boldsymbol{k}$ at the resonance:

$$\boldsymbol{k}\cdot\boldsymbol{\omega}(\boldsymbol{I}) = 0, \tag{1.68}$$

and by the divergence of the series in a neighbourhood of all the resonances. Regular solutions exist with weaker requirements for the transformation. For example, if the Fourier spectrum of $\mathcal{H}$ is finite (i.e. $\hat{\mathcal{H}}_{\boldsymbol{k}} \neq 0$ only for a finite set of vectors $\boldsymbol{k}$), then the series sums to a regular function in a domain of the actions space which excludes a neighbourhood of the finite number of resonances which are in the spectrum. In this thesis, we will define χ by considering the finite spectrum perturbations which are obtained by truncating the original Hamiltonian to a suitably large Fourier order.

Moreover, the transformation χ can be defined also in the neighbourhood of some specific resonances

$$\overline{\boldsymbol{k}}\cdot\boldsymbol{\omega}(\boldsymbol{I}) = 0, \tag{1.69}$$

simply by excluding the vectors $\boldsymbol{k}$ parallel to $\overline{\boldsymbol{k}}$ from the series. In this way we obtain resonant normal form, where at order ε of the Hamiltonian may depend on the angles only through the combinations $\boldsymbol{k}\cdot\boldsymbol{\varphi}$ with $\boldsymbol{k}$ integer vectors parallel to $\overline{\boldsymbol{k}}$. A more advanced treatment of the problem of small divisors lead to the celebrated KAM and Nekhoroshev theorems.

1.3.3 Floquet theory

The Floquet theorem (Floquet, 1883) has become the most important method to represent the solutions of the periodic linear differential systems of the form:

$$\dot{\boldsymbol{x}} = A(t)\boldsymbol{x}, \qquad \boldsymbol{x} \in \mathbb{R}^n \tag{1.70}$$

where $A(t)$ is a regular function of period T. By denoting with $\Phi(t)$ the principal fundamental matrix, whose columns are n linearly independent solutions of Eq. (1.70) satisfying $\Phi(0) = \mathbb{I}$, the Floquet theorem states that the principal fundamental matrix is decomposed as

$$\Phi(t) = C(t)e^{Bt}, \tag{1.71}$$

where $C(t)$ is a non-singular and $2T$-periodic function of t, $C(0) = \mathbb{I}$; while B is a matrix such that

$$\Phi(T)^2 = e^{2TB}, \tag{1.72}$$

called the *monodromy matrix*. Wiesel and Pohlen (1994) proved that if $\boldsymbol{x} = (\boldsymbol{q}, \boldsymbol{p}) \in \mathbb{R}^{2m}$, and the system (1.70) is Hamiltonian, then the matrix $C(t)$ is symplectic. This implies that there exists a canonical time-dependent change of variables $\boldsymbol{x} = C(t)\boldsymbol{y}$, $\boldsymbol{y} \in \mathbb{R}^n, n = 2m$ which conjugates the

Hamiltonian system (1.70) to the following autonomous one:

$$\dot{\boldsymbol{y}} = B\boldsymbol{y}. \tag{1.73}$$

To construct such a change of variables, the computation of the monodromy matrix $\Phi(T)$ as well as of its logarithms is required.

In connection to the Lagrangian equilibria L_1, L_2 of the ER3BP, Paez and Guzzo (2021) proved that given the linearized Hamiltonian equations

$$\frac{d\boldsymbol{x}}{df} = A(f;e)\boldsymbol{x}, \qquad \boldsymbol{x} = (X - X_{L_i}, Y, P_X, P_Y - X_{L_i}) \tag{1.74}$$

where e and f denote the orbital eccentricity and true anomaly of the secondary body, and $A(f;e) = \mathbb{E}\mathcal{H}_2$ where $\mathbb{E}$ and $\mathcal{H}_2$ denote respectively the standard symplectic matrix and the second order term of the Hamiltonian (1.45) expanded at the equilibrium point L_1 or L_2. We denote by $\Phi(2\pi;e)$ the principal fundamental matrix of (1.74), and $\boldsymbol{\Phi}_e := \Phi(2\pi;e)$ the monodromy matrix; the authors in Paez and Guzzo (2021) proved the following

Lemma 1 *Assume that the matrix $\boldsymbol{\Phi}_e$ has a couple of real eigenvalues $e^{2\pi\lambda} > e^{-2\pi\lambda}$ and two different couples of complex conjugate eigenvalues $a_1 \pm ib_1$, $a_2 \pm ib_2$ with $a_1^2 + b_1^2 = a_2^2 + b_2^2$ and $b_1, b_2 > 0$. Then there exists a real symplectic matrix C, which is explicit function of the eigenvectors of $\boldsymbol{\Phi}_e$, such that the matrix defined by*

$$\hat{B}_e(k_1,k_2) = C \begin{pmatrix} 0 & 0 & 0 & \pm(\omega_1+k_1) & 0 & 0 \\ 0 & 0 & 0 & 0 & \pm(\omega_2+k_2) & 0 \\ 0 & 0 & \pm\lambda & 0 & 0 & 0 \\ \mp(\omega_1+k_1) & 0 & 0 & 0 & 0 & 0 \\ 0 & \mp(\omega_2+k_2) & 0 & 0 & 0 & 0 \\ 0 & 0 & 0 & 0 & 0 & \mp\lambda \end{pmatrix} C^{-1}, \tag{1.75}$$

where

$$\omega_j = \frac{1}{2\pi}\arccos(a_j), \quad j = 1,2 \tag{1.76}$$

k_1, k_2 are arbitrary integer numbers and the choice of the signs in the matrix depends on the eigenvectors of $\boldsymbol{\Phi}_e$, satisfies

$$e^{2\pi\hat{B}_e(k_1,k_2)} = \boldsymbol{\Phi}_e. \tag{1.77}$$

The matrix $\hat{B}_e(k_1,k_2)$ is Hamiltonian, i.e.

$$(\mathbb{E}\hat{B}_e(k_1,k_2))^T = \mathbb{E}\hat{B}_e(k_1,k_2), \tag{1.78}$$

and defines a canonical Floquet transformation

$$\mathcal{C}(f;e) = \Phi(f;e)e^{-f\hat{B}_e(k_1,k_2)} \tag{1.79}$$

which for $e = 0$ is the identify matrix $\mathcal{C}(f;0) = \mathbb{I}$ if k_1, k_2 satisfy

$$\hat{B}_0(k_1,k_2) = A_0, \quad A_0 := A(f;0). \tag{1.80}$$

As a consequence of the lemma, $2\pi\hat{B}_e(k_1)$ represents a logarithm of the monodromy matrix for all the values of k_1. For the choice of a suitable value of $2\pi\hat{B}_e(k_1)$ it is convenient to fix the integer k_1 by using (1.80).

Therefore, using the Floquet transformation defined according to Lemma 1, Guzzo and Paez conjugated the Hamiltonian (1.45) to an Hamiltonian of the form:

$$K(\boldsymbol{Q},\boldsymbol{P};f) = K_2(\boldsymbol{Q},\boldsymbol{P}) + \sum_{j\geq 3} K_j(\boldsymbol{Q},\boldsymbol{P};f) \tag{1.81}$$

where $(\boldsymbol{Q},\boldsymbol{P})$ are canonical variables such that $(\boldsymbol{Q},\boldsymbol{P}) = (\boldsymbol{0},\boldsymbol{0})$ correspond to the selected Lagrangian equilibrium point; the second order term satisfies

$$K_2(\boldsymbol{Q},\boldsymbol{P}) = \sigma\frac{Q_1^2+P_1^2}{2} + \lambda Q_2 P_2 \quad \sigma,\lambda > 0, \tag{1.82}$$

where $K_j(\boldsymbol{Q},\boldsymbol{P};f)$ are polynomial in $\boldsymbol{Q},\boldsymbol{P}$ of order j and depend periodically on the anomaly f. Hamiltonian (1.81) was then normalized with a non-autonomous version of the usual Birkhoff normalization.

1.3.4 Birkhoff normal forms

Let $\boldsymbol{q} = (q_1,\ldots,q_n)$ and $\boldsymbol{p} = (p_1,\ldots,p_n)$ be canonical coordinates and momenta, and consider the Hamilton function

$$\mathcal{H}(\boldsymbol{q},\boldsymbol{p}) = \mathcal{H}_2(\boldsymbol{q},\boldsymbol{p}) + \mathcal{P}(\boldsymbol{q},\boldsymbol{p}) \tag{1.83}$$

where

$$\mathcal{H}_2(\boldsymbol{q},\boldsymbol{p}) = \sum_{j=1}^{n}\omega_j\frac{p_j^2+q_j^2}{2}, \tag{1.84}$$

and $\mathcal{P}$ is a smooth function having the origin as zero of order three. For a given integer $N \geq 2$, the Birkhoff normal form theorem (for a recent formulation see Giorgilli, 2012) states that if the frequency vector $\boldsymbol{\omega} = (\omega_1,\ldots,\omega_n)$ is such that

$$\boldsymbol{\omega}\cdot\boldsymbol{k} \neq 0,\ \forall \boldsymbol{k}\in\mathbb{Z}^n\backslash\{\boldsymbol{0}\} \text{ such that } \sum_{\nu=1}^{n}|k_\nu| \leq N, \tag{1.85}$$

then there exists a canonical transformation defined in a neighbourhood of the origin that conjugates the Hamiltonian (1.83) to

$$\tilde{\mathcal{H}}(\boldsymbol{q},\boldsymbol{p}) = \mathcal{H}_2(\boldsymbol{q},\boldsymbol{p}) + \sum_{j=2}^{[N/2]}\mathcal{Z}_{2j}(\boldsymbol{q},\boldsymbol{p}) + \mathcal{R}_{N+1}(\boldsymbol{q},\boldsymbol{p}) \tag{1.86}$$

where $\mathcal{Z}_{2j}$ is a polynomial of degree j in the terms $(q_j^2+p_j^2)/2$, and $\mathcal{R}_{N+1}$ is a reminder of order $N+1$. The Hamiltonian (1.86) is called the *Birkhoff normal form of order* N.

To construct the Birkhoff normal form of order N, an iterative procedure whose elementary steps are named *Birkhoff steps*, is required. First of all we rewrite the Hamiltonian (1.83) in terms

of the Birkhoff canonical complex variables $\boldsymbol{Q} = (Q_1, \ldots, Q_n)$ and $\boldsymbol{P} = (P_1, \ldots, P_n)$ defined by

$$Q_j = \frac{ip_j + q_j}{\sqrt{2}}, \quad P_j = \frac{p_j + iq_j}{\sqrt{2}}, \tag{1.87}$$

and then we expand it in power series around the origin. In such a way we obtain

$$H^{(2)}(\boldsymbol{Q}, \boldsymbol{P}) = \mathcal{H}_2(\boldsymbol{Q}, \boldsymbol{P}) + \sum_{\alpha=3}^{N} H_\alpha^{(2)}(\boldsymbol{Q}, \boldsymbol{P}) + \mathcal{R}_{N+1}^{(2)}(\boldsymbol{Q}, \boldsymbol{P}) \tag{1.88}$$

where $H_\alpha^{(2)}$ are polynomial of degree α in $\boldsymbol{Q}$ and $\boldsymbol{P}$. To construct the intermediate Birkhoff normal forms of order j given by

$$H^{(j)}(\boldsymbol{Q}, \boldsymbol{P}) = \mathcal{H}_2(\boldsymbol{Q}, \boldsymbol{P}) + \sum_{\alpha=2}^{[j/2]} \mathcal{Z}_{2\alpha}^{(j)}(\boldsymbol{Q}, \boldsymbol{P}) + \mathcal{R}_{j+1}^{(j)}(\boldsymbol{Q}, \boldsymbol{P}) \tag{1.89}$$

we use the iterative scheme

$$H^{(j)} = H^{(j-1)} \circ \phi_{\chi_j} \tag{1.90}$$

for $j = 3, \ldots, N$, where ϕ_{χ_j} is the Hamiltonian flow at time 1 of a suitable generating function χ_j. In the hypothesis that $\mathcal{Z}_j^{(j-1)}$ is written as a Taylor expansion, i.e.

$$\mathcal{Z}_j^{(j-1)} = \sum_{l,m \in \mathbb{N}^n} z_{lm} \boldsymbol{Q}^l \boldsymbol{P}^m, \tag{1.91}$$

($\boldsymbol{Q}^l$ denotes $Q_1^{l_1} \cdots Q_n^{l_n}$; $\boldsymbol{P}^m$ denotes $P_1^{m_1} \cdots P_m^{m_n}$) then the generating function χ_j is found by solving

$$\{\mathcal{H}_2, \chi_j\} = \mathcal{Z}_j^{(j-1)} - \langle \mathcal{Z}_j^{(j-1)} \rangle, \tag{1.92}$$

where

$$\langle \mathcal{Z}_j^{(j-1)} \rangle = \sum_{l \in \mathbb{N}^n} z_{ll} \boldsymbol{Q}^l \boldsymbol{P}^l. \tag{1.93}$$

The solution of the Eq. (1.92) is possible because on the one hand the terms contain only a finite number of monomials, on the other hand because the frequency vector $\boldsymbol{\omega}$ does not satisfies the resonant relations defined by all these terms. As a matter of fact, this is the formulation of the Lie method previously described, but using Cartesian like variables rather than action-angle variables.

1.3.5 The Floquet-Birkhoff normal forms: application to the elliptic restricted three-body problem

In Paez and Guzzo (2021) a combination of the Floquet theory and the Birkhoff normal forms was used to conjugate the Hamiltonian (3.4) of the ER3BP to an Hamiltonian system that is autonomous and integrable up to a given order N.

The first step is to rewrite the Hamiltonian of the ER3BP in terms of the translated Cartesian coordinates $(\boldsymbol{q}, \boldsymbol{p})$, defined as

$$q_1 = X - X_{L_i}, \quad q_2 = y, \quad p_1 = P_X, \quad p_2 = P_Y, \tag{1.94}$$

and to expand it around the origin; in such a way we obtain the Hamiltonian

$$H(\boldsymbol{q},\boldsymbol{p},f)=\sum_{i=2}^{N}H_i(\boldsymbol{q},\boldsymbol{p},f)+\mathcal{P}_{N+1}(\boldsymbol{q},\boldsymbol{p},f). \tag{1.95}$$

Then a canonical Floquet transformation

$$(\boldsymbol{q},\boldsymbol{p})=C(f)(\tilde{\boldsymbol{q}},\tilde{\boldsymbol{p}}) \tag{1.96}$$

that conjugates (1.95) to

$$\tilde{H}(\tilde{\boldsymbol{q}},\tilde{\boldsymbol{p}},f)=\tilde{H}_2(\tilde{\boldsymbol{q}},\tilde{\boldsymbol{p}})+\sum_{\nu=3}^{N}\tilde{H}_\nu(\tilde{\boldsymbol{q}},\tilde{\boldsymbol{p}},f)+\tilde{\mathcal{P}}_{N+1}(\boldsymbol{q},\boldsymbol{p},f) \tag{1.97}$$

where $\tilde{H}_\nu$ is a polynomial of degree ν in the variables $\tilde{\boldsymbol{q}}$ and $\tilde{\boldsymbol{p}}$, and is 2π-periodic in f. By denoting by

$$(\tilde{\boldsymbol{q}},\tilde{\boldsymbol{p}})=D(\tilde{\boldsymbol{Q}},\tilde{\boldsymbol{P}}) \tag{1.98}$$

the linear coordinates transformation (1.87), then the Hamiltonian $\tilde{H}$ becomes

$$\tilde{K}(\hat{\boldsymbol{Q}},\hat{\boldsymbol{P}})=\tilde{K}_2(\tilde{\boldsymbol{Q}},\tilde{\boldsymbol{P}})+\sum_{j\geq 3}\tilde{K}_j(\tilde{\boldsymbol{Q}},\tilde{\boldsymbol{P}},f)+\tilde{\mathcal{R}}_{N+1}(\tilde{\boldsymbol{Q}},\tilde{\boldsymbol{P}},f) \tag{1.99}$$

where:

$$\tilde{K}_2(\tilde{\boldsymbol{Q}},\tilde{\boldsymbol{P}})=\sigma\frac{\tilde{Q}_1^2+\tilde{P}_1^2}{2}+\lambda\tilde{Q}_2\tilde{P}_2,\qquad \sigma,\lambda>0. \tag{1.100}$$

Finally, thanks to an additional Birkhoff normalization up to order $N-2$, the dependence on f is moved to order N, and we obtain the Hamiltonian

$$K(\boldsymbol{Q},\boldsymbol{P},f)=\sum_{j=1}^{[N/2]}K_{2j}(\boldsymbol{Q},\boldsymbol{P})+\mathcal{R}_{N+1}(\boldsymbol{Q},\boldsymbol{P},f) \tag{1.101}$$

with K_{2j} depending on the $\boldsymbol{Q},\boldsymbol{P}$ only through the combinations $(Q_1^2+P_1^2)/2$ and Q_2P_2.

1.4 Finite time chaos indicators

The finite chaos indicators have been introduced to analyze with numerical experiments, performed on relatively short integration times, the dynamics of a complex dynamical system up to much longer time spans. The analysis include sharp computations of phase-portraits, as well as the distribution of regular and chaotic orbits in the phase-space and the computation of stable/unstable manifolds or Lagrangian coherent structures. Several chaos indicators have been introduced so far, we mention the finite time Lyapunov exponent (FTLE), the mean exponential growth of nearby orbits (MEGNO) and the fast Lyapunov indicator (FLI). In this thesis, we focus on the FLI, introduced in Froeschlé et al. (1997a,b), and modified afterwards (Froeschlé et al., 2000; Guzzo and Lega, 2014, 2015, 2017, 2018).

A recent modification of the FLI (the modified FLI, introduced in Guzzo and Lega (2014)) considerably improved the precision of this chaos indicator in computing the stable or unstable

manifolds of periodic orbits of the center manifolds of partially hyperbolic equilibrium points, as well as of the collision manifolds (Guzzo and Lega, 2014, 2015; Lega and Guzzo, 2016a,b; Guzzo and Lega, 2018).

In this Section we first review the more classic characteristic Lyapunov exponent as a tool to quantify the separation between solutions with close initial conditions. Then, we introduce the FLI and we describe, as elementary application, its use to compute the distribution of regular and chaotic orbits, as well as the stable manifold of a fixed point for the model example provided by the standard map.

1.4.1 The characteristic Lyapunov exponents

Given an open set $\Omega \subset \mathbb{R}^n$ and a vector field $X : \Omega \to \mathbb{R}^n$, we consider the system of differential equations

$$\dot{\boldsymbol{x}} = X(\boldsymbol{x}), \qquad \boldsymbol{x} \in \Omega \tag{1.102}$$

and we discuss the method based on the computation of the Lyapunov characteristic exponent (LCE) to characterize the asymptotic separation of the solutions with initial conditions close to a given point $\boldsymbol{x}_0 \in \Omega$.

The *Lyapunov characteristic exponent* of the initial condition $\boldsymbol{x}_0$ and initial tangent vector $\boldsymbol{k}_0 \in \mathbb{R}^n$ is defined by the limit:

$$\chi(\boldsymbol{x}_0, \boldsymbol{k}_0) := \lim_{t\to\infty} \frac{\ln \|\boldsymbol{k}(t)\|}{t} \tag{1.103}$$

where $\boldsymbol{k}(t)$ is the solution with initial condition $\boldsymbol{k}_0$ of the variational equations of (1.102):

$$\dot{\boldsymbol{k}} = B(t)\boldsymbol{k} \tag{1.104}$$

where:

$$B_{ij}(t) = \frac{\partial X_i}{\partial x_j}(\boldsymbol{x}(t)), \tag{1.105}$$

and $\boldsymbol{x}(t)$ denotes the solution of (1.102) with initial condition $\boldsymbol{x}_0$.

The most important characteristic Lyapunov exponent is the largest one:

$$\mathrm{LLCE}(\boldsymbol{x}_0) = \max_{\boldsymbol{k}_0 \in \mathbb{R}^n \setminus \mathbf{0}} \chi(\boldsymbol{x}_0, \boldsymbol{k}_0) \tag{1.106}$$

which characterize the strongest asymptotic law of separation of the solution $\tilde{\boldsymbol{x}}(t)$ with initial conditions close to $\boldsymbol{x}_0$: in fact, if $\lambda := \mathrm{LLCE}(\boldsymbol{x}_0)$, we have

$$\|\boldsymbol{x}(t) - \tilde{\boldsymbol{x}}(t)\| \approx \|\boldsymbol{x}(0) - \tilde{\boldsymbol{x}}(0)\| e^{\lambda t} \tag{1.107}$$

as soon as $\tilde{\boldsymbol{x}}(t)$ remains close to $\boldsymbol{x}(t)$. If $\mathrm{LLCE}(\boldsymbol{x}_0) \leq 0$, there is not exponential separation of the solutions with close initial conditions (as it happens for the Hamiltonian systems which are Liouville-Arnold integrable).

We recall some basic properties of the LCE:

- the value of the LCE depends on the direction of the initial tangent vector, and not on its norm;

- if the system (1.102) is Hamiltonian and Liouville-Arnold integrable, then the time evolution of the tangent vector is at most linear. As a matter of fact, the variational equations:

$$\dot{I}_j = 0, \quad \dot{\varphi}_j = \omega_j(\boldsymbol{I}), \quad \dot{k}_{I_j} = 0, \quad \dot{k}_{\varphi_j} = \sum_{i=1}^{n} \frac{\partial \omega_j}{\partial I_i}(\boldsymbol{I}) k_{I_i}, \quad j = 1, \ldots, n \tag{1.108}$$

are immediately integrated, and we have

$$k_{I_j}(t) = k_{I_j}(0), \quad k_{\varphi_j}(t) = k_{\varphi_j}(0) + \sum_{i=1}^{n} \frac{\partial \omega_j}{\partial I_i}(\boldsymbol{I}_0) k_{I_i}(0) t. \tag{1.109}$$

Since the evolution of the tangent vector is at most linear in time, the characteristic Lyapunov exponents are equal to zero;

- if the dynamical system has an hyperbolic saddle equilibrium point $\boldsymbol{x}_{\text{eq}}$, then the variational equations for the equilibrium solutions is:

$$\dot{\boldsymbol{k}} = A\boldsymbol{k} \tag{1.110}$$

where A is the linearization matrix of the vector field X computed at $\boldsymbol{x}_{\text{eq}}$. Therefore, from the standard theory of linear ODE, $\lambda_1, \ldots, \lambda_n \in \mathbb{R}$ are the eigenvalues of A, then the largest characteristic Lyapunov exponent is $\max_{i \in \{1,\ldots,n\}} \lambda_i$;

- if the dynamical system has $\boldsymbol{x}_{\text{eq}}$ as equilibrium point, by denoting with A the linearization matrix at $\boldsymbol{x}_{\text{eq}}$, one proves that the largest LCE of $\boldsymbol{x}_{\text{eq}}$ is the maximum of $\text{Re}\lambda$, where λ is any eigenvalue (real or complex) of A.

In general for a n-dimensional dynamical system, the set of the characteristic Lyapunov exponents of an initial datum $\boldsymbol{x}_0$ is discrete, with at most n values. Moreover, if the dynamical system admits an equilibrium point $\boldsymbol{x}_{\text{eq}}$, then for all the initial data $\boldsymbol{x}_0$ such that $\lim_{t\to\infty} \Phi^t(\boldsymbol{x}_0) = \boldsymbol{x}_{\text{eq}}$ the characteristic Lyapunov exponents of $\boldsymbol{x}_0$ is that of $\boldsymbol{x}_{\text{eq}}$: hence the stable manifold of $\boldsymbol{x}_{\text{eq}}$ has the same Lyapunov exponents of the equilibrium point $\boldsymbol{x}_{\text{eq}}$.

Since the largest characteristic Lyapunov exponent quantifies the separation between two initial datum and its value is dependent only on the direction of the initial tangent vector, it is common to use

$$\lambda_L := \max_{\boldsymbol{k}_0 \in T_{\boldsymbol{x}_0}\Omega \setminus \{\boldsymbol{0}\}} \chi(\boldsymbol{x}_0, \boldsymbol{k}_0) \tag{1.111}$$

as a quantity to discriminate if an orbit is chaotic or not. As a matter of fact, if $\lambda_L > 0$ then the orbit with the initial condition $\boldsymbol{x}_0$ is said to be *chaotic*; otherwise the orbit is said to be *regular*. We note that the solutions of an integrable system are regular since the characteristic Lyapunov exponents are zero. For further details about the characteristic Lyapunov exponents, the reader is referred to Benettin et al. (1980a,b).

The numerical estimate of the largest Lyapunov exponent is expensive since it requires to numerically integrate the variational equations for the time needed to appreciate a stabilization of $\ln \|\boldsymbol{k}(t)\|/t$. In the last decades, new classes of finite time indicators were introduced: the main property of such indicators is that they allow to understand if the solution with initial condition $\boldsymbol{x}_0$ is chaotic or regular with a numerical integration done on a time-span which is much smaller than the time-span required to have a reliable estimation of $\text{LCE}(\boldsymbol{x}_0)$.

Examples of popular finite time chaos indicators are the fast Lyapunov indicators (Froeschlé et al., 1997a,b), the finite time Lyapunov exponent (Tang and Boozer, 1996), and the mean exponential growth of nearby orbits (Cincotta and Simó, 2000). For an overview of the FLI, the reader is referred to Guzzo and Lega (2021).

1.4.2 The fast Lyapunov indicator

The fast Lyapunov Indicators (FLI) were originally introduced in Froeschlé et al. (1997a,b) and then modified in Froeschlé et al. (2000); Guzzo and Lega (2014, 2015); Lega and Guzzo (2016b); Guzzo and Lega (2017, 2018). In their most commonly used version, they are defined as:

$$\mathrm{FLI}(\boldsymbol{x}_0, \boldsymbol{k}_0; T) = \max_{t\in[0,T]} \log \frac{\|\boldsymbol{k}(t)\|}{\|\boldsymbol{k}_0\|} \tag{1.112}$$

where $\boldsymbol{k}(t)$ is the solution of the variational equations with initial conditions $\boldsymbol{x}_0 = \boldsymbol{x}(0)$ and $\boldsymbol{k}_0 = \boldsymbol{k}(0)$. We note that

$$\chi(\boldsymbol{x}_0, \boldsymbol{k}_0) = \lim_{T\to\infty} \frac{\mathrm{FLI}(\boldsymbol{x}_0, \boldsymbol{k}_0; T)}{T}. \tag{1.113}$$

We remark that for chaotic orbits the time evolution of the FLI is approximately linear, while for regular orbits, the FLI evolves approximately as a logarithm; this fact is independent of the choice of the initial tangent vector, unless the initial tangent vector has null components on some special directions, such as the expanding directions of the tangent space. Hence, after short times T, the FLI value of chaotic orbits are higher than those of regular orbits. Therefore one is interested to compare the FLI for different orbits and it is usual to compute the FLI for a large set of initial data in the phase-space for the same initial tangent vector.

Let us illustrate the basic properties of the FLI on the most popular model example, represented by the dynamics obtained from the iterations of the standard map:

$$\begin{aligned} \Phi_\epsilon : \mathbb{T}^1 \times \mathbb{R} &\to \mathbb{T}^1 \times \mathbb{R} \\ (\varphi_n, I_n) &\mapsto (\varphi_{n+1}, I_{n+1}) \end{aligned} \tag{1.114}$$

defined by:

$$\begin{aligned} \varphi_{n+1} &= (\varphi_n + I_n) \mathrm{mod}(2\pi) \\ I_{n+1} &= I_n + \epsilon \sin(\varphi_n + I_n) \end{aligned} \tag{1.115}$$

where $\epsilon > 0$ is a parameter characterizing the dynamics.

We note that the standard map admits the fixed points $(\varphi, I) = (0, 0)$ and $(\varphi, I) = (\pi, 0)$ for all the values of ϵ. For $\epsilon > 0$ the fixed point $(\varphi, I) = (0, 0)$ is hyperbolic and it is well known that the related stable and unstable manifolds define a chaotic dynamics. In Fig. 1.6 we provided some orbits of the standard map for $\epsilon = 1.2$. We note that some orbits spread chaotically, while other are on invariant curves.

The variational equations of the standard map:

$$\begin{aligned} k_{\varphi,n+1} &= k_{\varphi,n} + k_{I,n} \\ k_{I,n+1} &= k_{I,n} + \epsilon(k_{\varphi,n} + k_{I,n}) \cos(\varphi_n + I_n) \end{aligned} \tag{1.116}$$

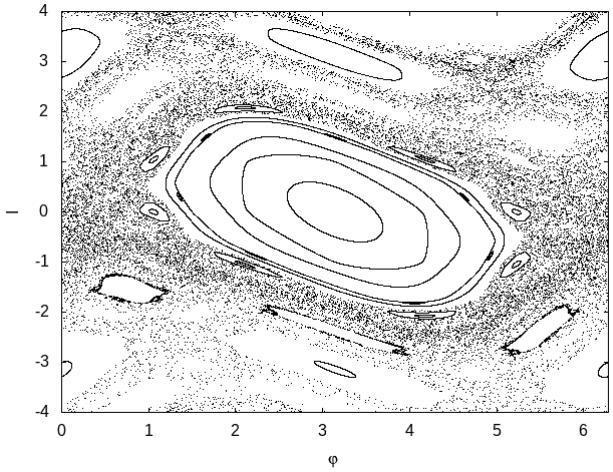

Figure 1.6: Some orbits of the standard map for $\epsilon = 1.2$ computed up to $N_{\max} = 10000$ iterations.

provide the time evolution of the tangent vectors. In Fig. 1.7 we plot the evolution of

$$\frac{\log(\|\boldsymbol{k}_n\|)}{n} \tag{1.117}$$

for three different orbits of the standard map: the first two orbits (top and middle panels) are confined in invariant curves, while the third one (bottom panels) spreads in the phase-space. In all the three cases we use $k_{\varphi,0}, k_{I,0} = 1/\sqrt{2}$ as initial tangent vector of the variational equations. We note that for the orbits confined on invariant curves the function (1.117) seems to converge to zero, while for the chaotic orbit (bottom panels) there is no such a convergence. This provides the indication that the largest Lyapunov exponent of the first two orbits is zero, while for the third orbit is positive. In Fig. 1.8 we represent the value of the fast Lyapunov indicator

$$\mathrm{FLI}((\varphi_0, I_0), \boldsymbol{k}_0; N) = \max_{n\in[0,N]} \log \frac{\|\boldsymbol{k}_n\|}{\|\boldsymbol{k}_0\|} \tag{1.118}$$

for a grid of 1000×1000 initial data $(\varphi_0, I_0) \in [0, 2\pi] \times [-4, 4]$, and for different number of iterations

The computation of the fast Lyapunov indicator is stopped when the value of the FLI exceeds the threshold 20 (correspondingly, the norm of the tangent vector is grown by a factor greater than e^{20} in a number of iteration smaller than N). We note that the stable invariant manifold of the hyperbolic fixed point $(\varphi, I) = (0, 0)$, as well as of other periodic orbits, is identified by the highest values of the FLI. From the panels of Fig. 1.8. we appreciate that as we increase the number N of iterations, we see the appearance of longer pieces of the stable manifold of the point $(0, 0)$, as well as of other hyperbolic periodic orbits which are located in this part of the phase space. The unstable manifolds would be obtained by computing the FLI of the inverse map Φ_ϵ^{-1}.

For $N = 100$ (Fig. 1.8f) the chaotic regions (the points spread in the phase-space of Fig. 1.6) are sharply distinguished from the ordered regions where the regular orbits are located. We emphasize that the chaotic regions are identified by the highest values of the fast Lyapunov indicator in a number of iterations that is small with respect to that used for the computation of the function (1.117), and that the higher values of the fast Lyapunov indicator are located in the region of the phase-space which contains the stable and unstable manifolds generated by the fixed point $(\varphi, I) = (0, 0)$.

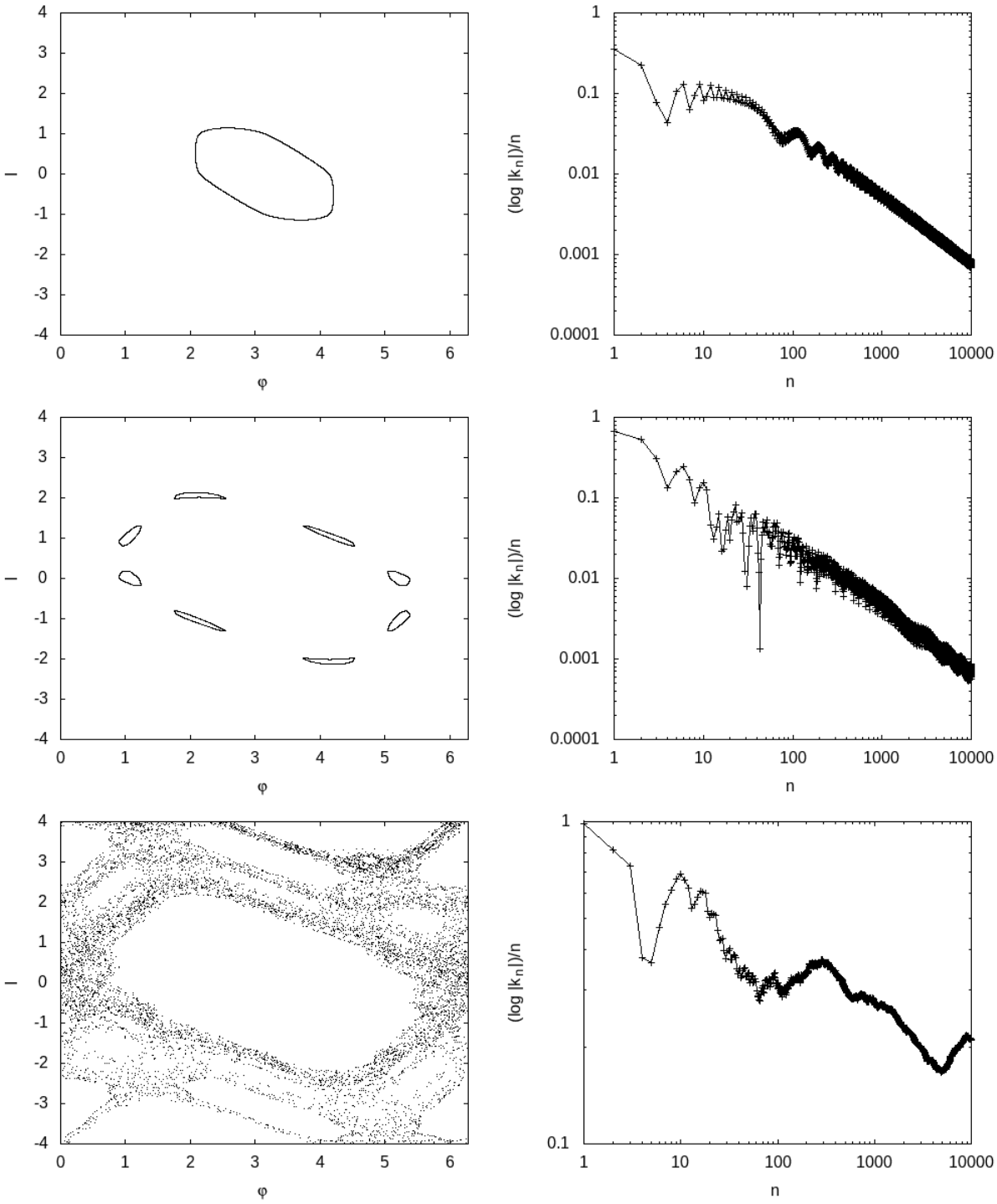

Figure 1.7: Some orbits of the standard map with $\epsilon = 1.2$ and the evolution of the function (1.117).

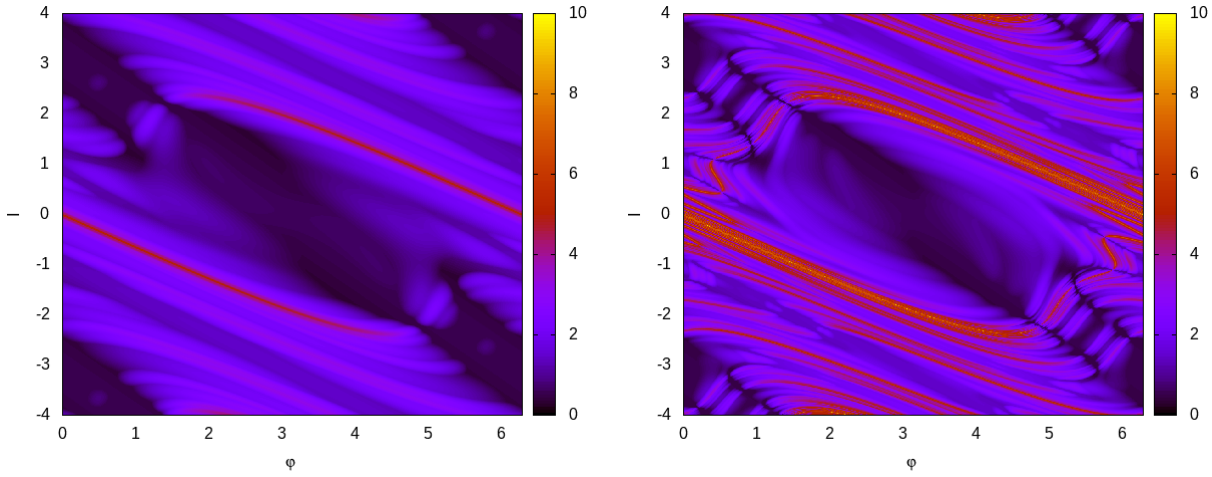

(a) $N = 5$.

(b) $N = 10$.

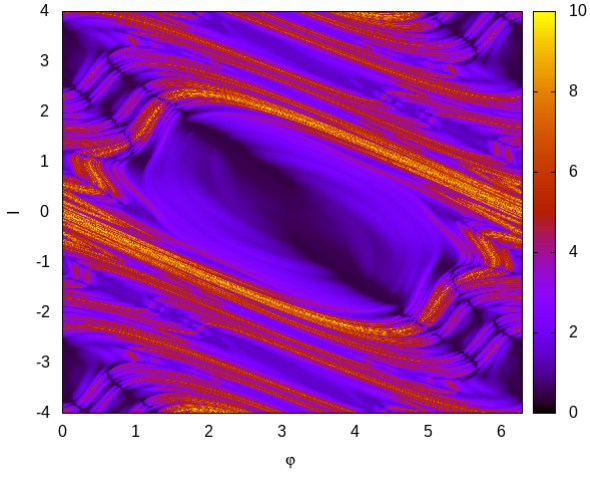

(c) $N = 15$.

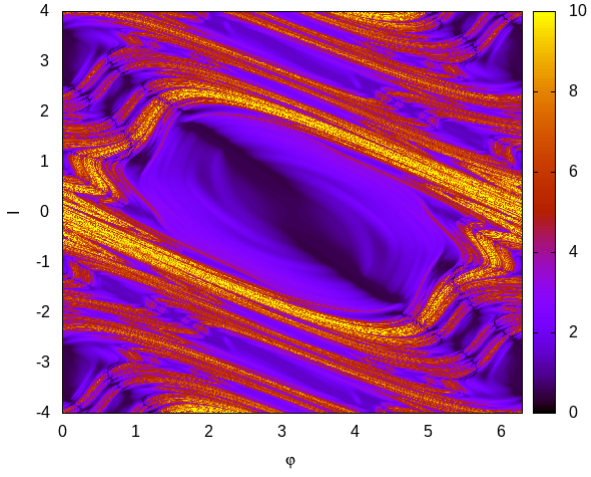

(d) $N = 20$.

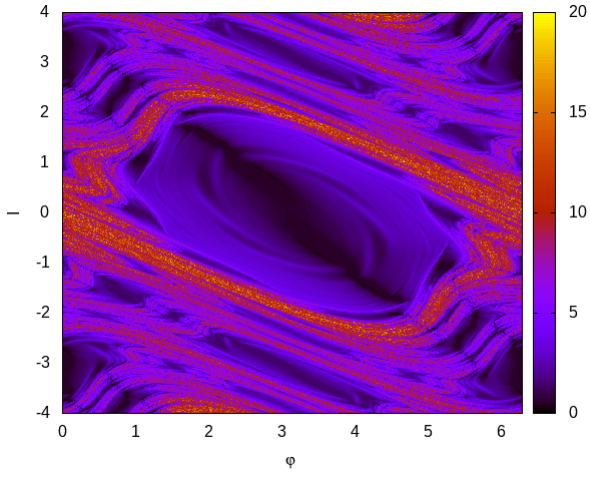

(e) $N = 30$.

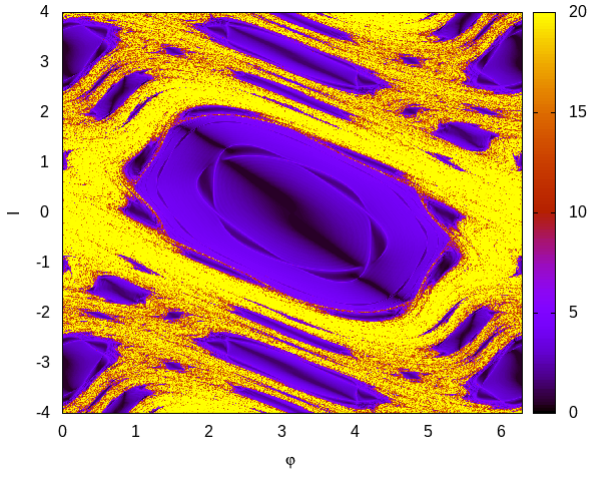

(f) $N = 100$.

Figure 1.8: FLI chart of the standard map for different number of iterations.

With this example, we show that the computation of the FLI for a grid on initial data allows to discriminate regular and chaotic orbits in a relatively small time-span. As a matter of fact the FLI method represents a useful tool to numerically analyze the phase-portrait of complex systems, for example we mention the following applications to astronomy (Guzzo, 2005, 2006; Gawlik et al., 2009; Celletti and Gales, 2014; Celletti et al., 2016; Celletti and Gales, 2016; Daquin et al., 2016; Celletti et al., 2017; Rosengren et al., 2017; Daquin et al., 2018; Gkolias et al., 2019; Todorović et al., 2020; Daquin et al., 2021a,b).

A major modification of the FLI has been introduced in Guzzo and Lega (2014); Lega and Guzzo (2016b) and latter applied in Guzzo and Lega (2018, 2015, 2017); Scantamburlo and Guzzo (2020) to enhance the computation of the stable and unstable manifolds tubes in the CR3BP, analyze the past dynamics and the collisional manifolds of comet 67P/Churyumov-Gerasimenko, and detect libration orbits around the Sun–Earth L_3 point in a model of the Solar System that is compatible with the ephemerides provided by the JPL digital service. As already remarked with the example of the standard map, the application of a traditional definition of FLI, such as the (1.112) and (1.118) allows to detect the stable and unstable manifolds of several hyperbolic periodic orbits and fixed points of the phase-space. Therefore, it is not sharp in the detection of the specific stable/unstable manifold of a periodic orbit of interest. Moreover, in Guzzo and Lega (2014) it is provided an example where the traditional definitions of the FLI completely miss the computation of the manifolds. To solve the problems, Guzzo and Lega introduced a major modification of the FLI, in which one considered the contribution to the new modified FLI only for the time intervals in which the orbit belongs to a neighbourhood $\mathcal{B}$ of the selected hyperbolic orbits. In such a way, the modified FLI provided a sharp computation of the stable/unstable manifolds of the selected orbit. The method has been successfully applied to compute the manifold tube of L_1, L_2 in the CR3BP (Lega and Guzzo, 2016b; Guzzo and Lega, 2018) to compute the collision manifolds of comet 67P/Churyumov-Gerasimenko with the planets (Guzzo and Lega, 2017, 2018), and in this thesis it will be used to compute orbits of libration around the Lagrangian point L_3 of the Sun–Earth system.

Specifically, the modification consists in the introduction of a window function w that is equal to one inside a suitable neighbourhood $\mathcal{B}$ of an hyperbolic target orbit γ, and converges rapidly to zero otherwise. This modification requires an integral formulation of the FLI since it takes into account to weight the growth of the chaos indicator depending on the distance of the the solution $\boldsymbol{x}(t)$ from the neighbourhood $\mathcal{B}$. As example, in Guzzo and Lega (2014) the detection of the stable and unstable manifold tubes originating at L_1 and L_2 in the CR3BP was done through a modified FLI defined as

$$\mathrm{mFLI}_w(\boldsymbol{x}_0, \boldsymbol{k}_0, T) = \max_{t\in[0,T]} \int_0^t w(\boldsymbol{x}(s)) \frac{\boldsymbol{k}(s)\cdot\dot{\boldsymbol{k}}(s)}{\|\boldsymbol{k}(s)\|^2} ds \tag{1.119}$$

where

$$w(\boldsymbol{x}) = \begin{cases} 1 & \text{if } \mathrm{dist}(\boldsymbol{x},\gamma) \le \frac{r}{2} \\ \frac{1}{2}\left[\cos\left(\left(\frac{\mathrm{dist}(\boldsymbol{x},\gamma)}{r} - \frac{1}{2}\right)\pi\right) + 1\right] & \text{if } \frac{r}{2} < \mathrm{dist}(\boldsymbol{x},\gamma) \le \frac{3r}{2} \\ 0 & \text{if } \mathrm{dist}(\boldsymbol{x},\gamma) > \frac{3r}{2} \end{cases}, \tag{1.120}$$

where $\mathrm{dist}(\boldsymbol{x},\gamma)$ denotes respectively the distance between $\boldsymbol{x}$ and γ, and r represents a parameter. We note that for orbits that never exit from the neighbourhood $\mathcal{B}$, the indicator (1.119) reduced to the classic FLI.

In Fig. 1.9 we represent the modified FLI computed for the standard map, with window function centered at $(0, 0)$, and $r = 0.4$. We appreciate a sharper computation of the stable manifold.

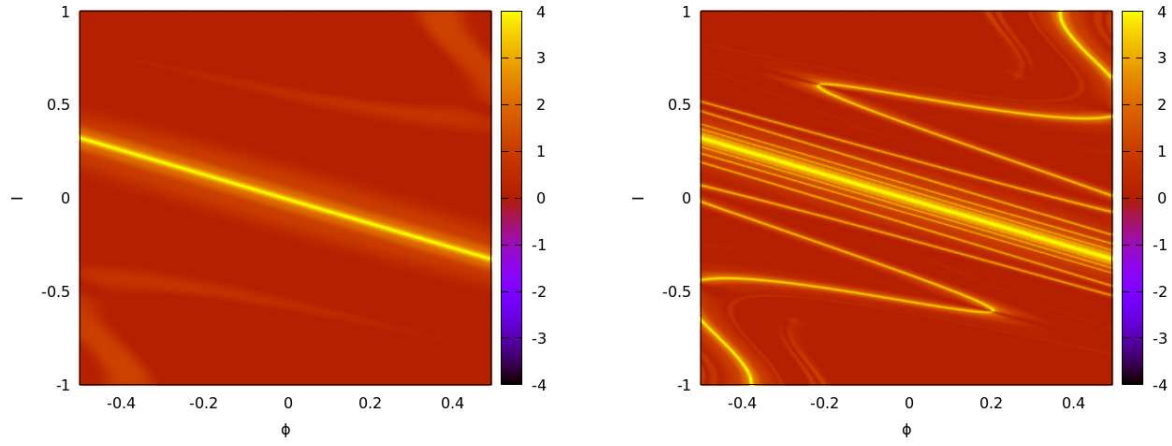

(a) $N = 5$.

(b) $N = 10$.

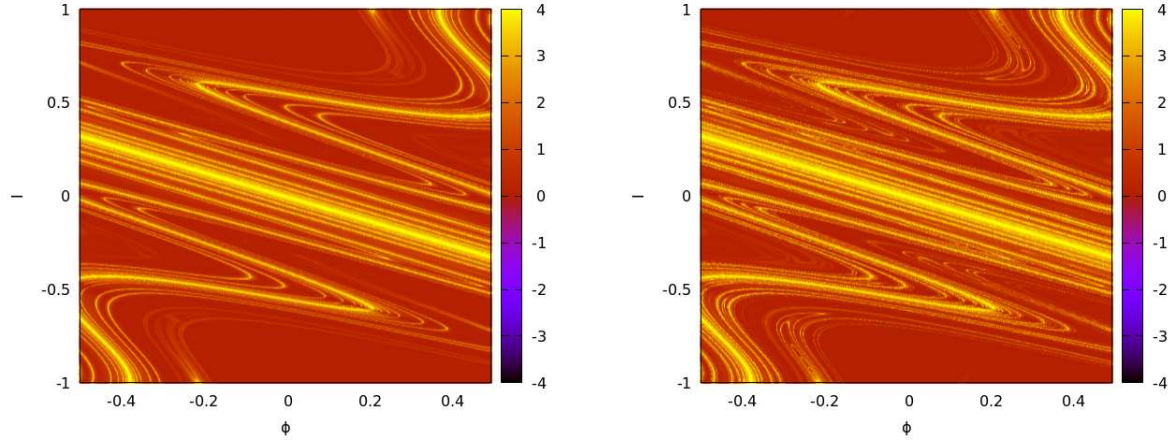

(c) $N = 15$.

(d) $N = 20$.

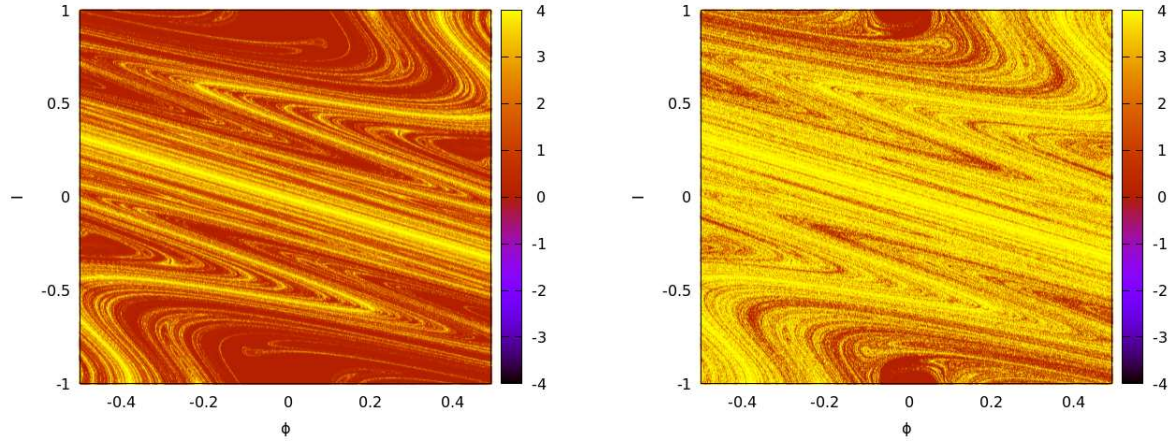

(e) $N = 30$.

(f) $N = 100$.

Figure 1.9: Modified FLI chart of the standard map for different number of iterations.

1.5 Impulsive orbital maneuvers

Since the solutions of the Kepler problem are conics sections, the only possibility in a two-body context for a spacecraft to transfer from one orbit to another one is through orbital maneuvers that

produce a change of the velocity. There exist several maneuvers that can be used for an orbital transfer, but during the PhD project we consider only *impulsive maneuvers*, i.e. we assume that the velocity change is instantaneous. The change of the velocity is practically performed by the propulsion system of the spacecraft through a consumption of the propellant, i.e. through a loss of the spacecraft mass Δm; if m denotes the spacecraft initial mass, Δv the norm of the change of the velocity, I_{sp} the specific impulse (quantity measuring the performance of a propulsion system), and g_0 is the sea-level standard acceleration, then

$$\frac{\Delta m}{m} = 1 - e^{-\frac{\Delta v}{I_{sp} g_0}}. \tag{1.121}$$

Eq. (1.121) is known as the *Tsiolkovsky rocket equation*. In Fig. 1.10 there is a representation of

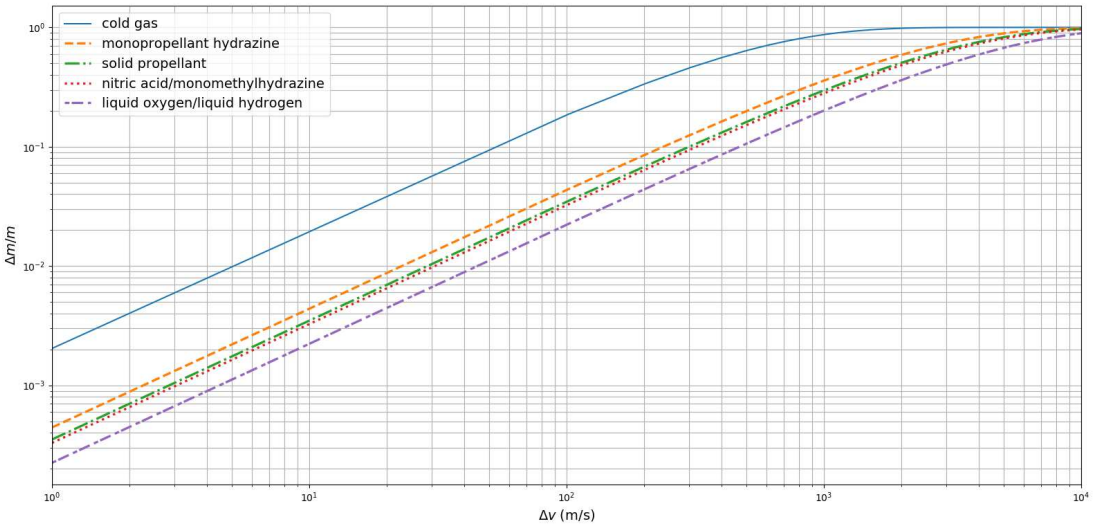

Figure 1.10: Loss mass rate $\Delta m/m$ of the spacecraft for different and common propellants. The values used of the specific impulse I_{sp} for the computation of the plot were taken in Curtis (2005).

the loss mass rate $\Delta m/m$ versus the change of the velocity Δv by using cold gas ($I_{sp} \sim 50\,\mathrm{s}$), monopropellant hydrazine ($I_{sp} \sim 230\,\mathrm{s}$), solid propellant ($I_{sp} \sim 290\,\mathrm{s}$), nitric acid/monomethylhydrazine ($I_{sp} \sim 310\,\mathrm{s}$), and liquid oxygen/hydrogen ($I_{sp} \sim 455\,\mathrm{s}$) as propellants[2].

There are several impulsive orbital maneuvers; the most famous one is the Hohmann transfer. Such maneuvers aims to realize a transfer between two coplanar circular orbits. The transfer is performed by an half-ellipse whose perihelion and aphelion are the radius of the two circular orbits; the reader is referred to Fig. 1.11 for a better comprehension. Let A and B be the departing and arrival locations of the spacecraft respectively; we denote by the subscript 1, 2, and 3 the quantities related to the departing, transfer, and arrival ellipses. Since the maneuver is impulsive,

$$\begin{cases} \rho_{A1} = \rho_{A2} \\ \rho_{B3} = \rho_{B2} \end{cases} = \begin{cases} a_1 = a_2(1 - e_2) \\ a_3 = a_2(1 + e_2) \end{cases} \implies e_2 = \frac{a_3 - a_1}{a_3 + a_1}, \quad a_2 = \frac{a_1 + a_3}{2}.$$

the total Δv is given by $\Delta v = \Delta v_A + \Delta v_B$, where $\Delta v_A = |v_{A2} - v_{A1}|$, and $\Delta v_B = |v_{B3} - v_{B2}|$. By

[2]The values of the specific impulses were taken in Curtis (2005).

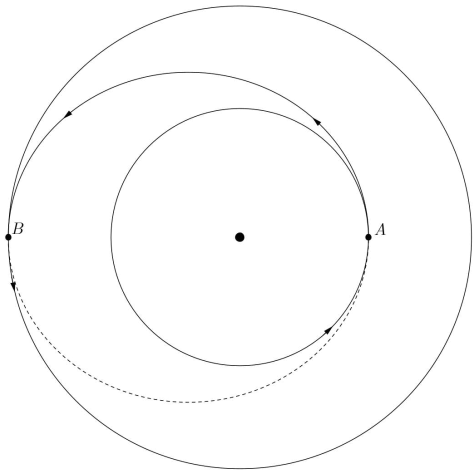

Figure 1.11: Representation of the Hohmann transfer between two coplanar circular orbits.

expressing these quantities using the orbital parameters of the orbits (1) and (3) we have:

$$\Delta v_A = \left| \sqrt{\frac{\mu}{a_1}} \left(\sqrt{\frac{2a_3}{a_1 + a_3}} - 1 \right) \right|, \quad \Delta v_B = \left| \sqrt{\frac{\mu}{a_3}} \left(1 - \sqrt{\frac{2a_1}{a_1 + a_3}} \right) \right|,$$

where μ denotes the sum of the gravitational parameters of the two bodies. The Hohmann transfer can be generalized to the case in which the departing and the arrival orbits are elliptic, coplanar and coaxial. Let A and A' be the perihelion or the aphelion of the starting ellipse, and let B and B' be the aphelion or perihelion of the arrival ellipse. The Δv of the transfer can be expressed in terms of the radius vector r_A, $r_{A'}$, r_B, and $r_{B'}$ associated to A, A', B, and B'. The delta-v for the transfer from A to B is

$$\Delta v = \sqrt{2\mu} \left(\left| \sqrt{\frac{r_B}{r_A(r_A + r_B)}} - \sqrt{\frac{r_{A'}}{r_A(r_A + r_{A'})}} \right| + \left| \sqrt{\frac{r_{B'}}{r_B(r_B + r_{B'})}} - \sqrt{\frac{r_A}{r_B(r_A + r_B)}} \right| \right)$$

while the delta-v for the transfer from A' to B' is

$$\Delta v' = \sqrt{2\mu} \left(\left| \sqrt{\frac{r_{B'}}{r_{A'}(r_{A'} + r_{B'})}} - \sqrt{\frac{r_A}{r_{A'}(r_A + r_{A'})}} \right| + \left| \sqrt{\frac{r_B}{r_{B'}(r_B + r_{B'})}} - \sqrt{\frac{r_{A'}}{r_{B'}(r_{A'} + r_{B'})}} \right| \right)$$

By defining the auxiliary variables

$$K := \frac{r_{A'}}{r_A}, \quad \xi := \frac{r_B}{r_A}, \quad \eta := \frac{r_{B'}}{r_A}$$

we obtain that

$$\Delta v = \sqrt{\frac{2\mu}{r_A}} \left(\left| \sqrt{\frac{\xi}{\xi + 1}} - \sqrt{\frac{K}{K + 1}} \right| + \left| \sqrt{\frac{\eta}{\xi(\xi + \eta)}} - \sqrt{\frac{1}{\xi(\xi + 1)}} \right| \right)$$

$$\Delta v' = \sqrt{\frac{2\mu}{r_A}} \left(\left| \sqrt{\frac{\eta}{K(\eta + K)}} - \sqrt{\frac{1}{K(K + 1)}} \right| + \left| \sqrt{\frac{\xi}{\eta(\xi + \eta)}} - \sqrt{\frac{K}{\eta(\eta + K)}} \right| \right).$$

To understand if the transfer from A to B is more efficient than the transfer from A' to B', it is useful to plot the function $\Upsilon(K, \xi, \eta) := \Delta v / \Delta v'$. If $\Upsilon > 1$ then the transfer from A to B is

cheaper; if $\Upsilon < 1$ the transfer from A' to B' is more efficient. In Fig. 1.12 we plot Υ for $K = 1$, $K = 4$ and $K = 1/4$. In particular we note that

- for $K = 1$ the starting orbit is a circle. Υ is equal to one only when $\xi = \eta$, i.e. when also the arrival orbit is a circle. $\Upsilon < 1$ for $\xi < \eta$ and $\eta \in (1, 10)$, namely the transfer to B' is more efficient when the arrival orbit is external to the starting one, and it has B' as aphelion;
- for $K = 4$ the starting orbit is an ellipse, where A and A' denote the perihelion and the aphelion respectively. $\Upsilon > 1$ for $\xi > 4$ and $\eta \in (1, 10)$, i.e. the transfer from A to B is more efficient when the arrival ellipse is outer to the starting one. $\Upsilon < 1$ for $\xi < 4$ and $\eta \in (1, 10)$, i.e. the transfer from A' to B' is more efficient when $r_B < 4r_A$ and $r_{B'} > r_A$ (the perihelion of the arrival ellipse is outer to the starting ellipse, and the aphelion of the arrival ellipse is inner to the starting ellipse);
- for $K = 1/4$ the starting orbit is an ellipse having A' as perihelion. The transfer from A' to B' is more efficient when the arrival ellipse is outer to the starting one.

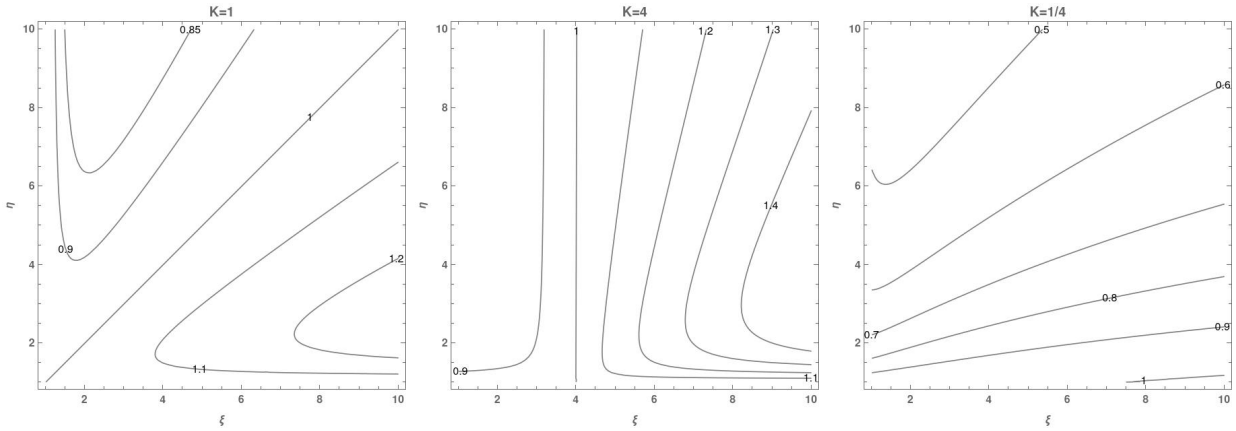

Figure 1.12: Plot of Υ for different values of K.

Chapter 2

Short-period effects of the planetary perturbations on the Sun–Earth L_3 point

2.1 Introduction

In the last two decades the dynamics close to the Lagrangian points L_1 and L_2 of the Sun-Earth circular restricted three-body problem (CR3BP) have been widely studied in connection with space mission design (Farquhar, 1968; Breakwell, 1970; Euler and Yu, 1971; Farquhar et al., 1977, 1979; Lukjanov, 1980; Heuberger, 1977; Muhanen, 1983; Farquhar, 1998; Gómez et al., 2001; Martin et al., 2010; van Damme et al., 2010; Koon et al., 2008; Parker and Anderson, 2013; Gómez et al., 2004). ISEE-3, SOHO, WMAP, Genesis, Herschel and Planck are just few examples of missions in which the spacecraft reached the vicinity of the Sun–Earth L_1 and L_2 points during its journey. While L_3 is also potentially useful for astrodynamics (Gómez et al., 2001; Gómez and Mondelo, 2001; Barrabés and Ollé, 2006; Terra et al., 2014; Paez and Efthymiopoulos, 2015; Jorba and Nicolás, 2020), no significant attention has been paid to the Sun–Earth L_3 point even if its Lyapunov orbits have been proposed as an ideal place for spacecraft because of the possibility to obtain data for the Sun, the inner planets, and the main belt from a new perspective (Hou et al., 2007; Tantardini et al., 2010). The aim of this study is to find orbits close to the Sun–Earth L_3 point that are useful for applications of astrodynamics. In particular, this refers to orbits that remain close to L_3 within useful distances at least for several decades in a model of the Solar System whose ephemerides are comparable with those provided by the JPL computation service. Because the planetary perturbations on the Sun–Earth Lagrangian point L_3 are stronger than the Earth's attraction itself, the CR3BP is not a realistic approximation of the dynamics close to L_3. The main differences between the real Solar System and the Sun–Earth CR3BP are caused by the planetary perturbations (mainly from Venus and Jupiter) and in the elliptic orbit of the Earth. To quantify the effects of planetary perturbations, we first consider a multicircular restricted problem (MCR8BP), where the eight planets of our Solar System (from Mercury to Neptune) perform circular motions around the Sun. Using Hamiltonian perturbation theory we find that the Hamiltonian of the MCR8BP is conjugate by a canonical transformation to an averaged Hamiltonian system that still has an equilibrium point close to L_3 (within terms of second order in the planetary masses and fourth order in eccentricity). This equilibrium, which we denote by $\mathcal{L}_3$, is still aligned in the Sun–

Earth direction. The individual contribution of each planet to the displacement of $\mathcal{L}_3$ from L_3 is reported in the first column of Table 2.1: it is remarkable that while Venus and Jupiter each move the position of this equilibrium by about 218 and 176 km respectively in opposite directions, in the model where both planets are included their effects almost perfectly compensate for one another, leaving a displacement of about 40 km only (the contributions of the other planets being smaller by about two orders of magnitude). Since the conjugation of the original Hamiltonian to the averaged one will be obtained with a canonical transformation depending on the planetary phases, the equilibrium $\mathcal{L}_3$ is then mapped in the original system to a quasi-periodic dynamical substitute; the contributions of each planet to the amplitude of this quasi-periodic libration around L_3, which are reported in the second column of Table 2.2, are quite large and sum to about $d = 10^{-4}$ AU $\sim 15\,000$ km. Since the linear stability of $\mathcal{L}_3$ is the same as that of L_3, the averaged Hamiltonian, approximated within terms of second order in the planetary masses, has close to $\mathcal{L}_3$ a dynamics similar to that of L_3 in the CR3BP; this means that in the vicinity of $\mathcal{L}_3$ there are periodic and quasi-periodic orbits. The image of these orbits in the original MCR8BP are orbits librating around L_3 of amplitudes larger than the amplitude of the dynamical substitute, which we denote hereafter by d.

Since the MCR8BP is still a rough approximation of the real Solar System, we use the fast Lyapunov indicators (FLI) to look for orbits of this kind in a model of the Solar System that is compatible with the precision of JPL digital ephemerides. In the last decades, the FLI have been used to find orbits related to the dynamics close to the Lagrangian points of the restricted three-body problem (Lega et al., 2011; Guzzo and Lega, 2013, 2014, 2018) and to close encounters in cometary dynamics (Guzzo and Lega, 2015, 2017). The method provides orbits that remain, within a given time-span, in a neighbourhood $\mathcal{B}$ of the dynamical substitute obtained from an approximated model. In order to construct the neighbourhood $\mathcal{B}$, we must also consider the differences between the real Solar System and the Sun–Earth CR3BP caused by the elliptic orbit of the Earth. As explained in Chapter 1, Sec. 1.2, the CR3BP is traditionally compared to the elliptic restricted three-body problem (ER3BP) by introducing a rotating-pulsating Cartesian reference frame which we denote by $OXYZ$ in which the primary and the secondary bodies remain in fixed locations of the X axis (Szebehely, 1967); moreover, the equations of motion in the rotating-pulsating reference frame are written in a simple Hamiltonian form if the mean anomaly of the planet is used as independent variable. In particular, in the rotating-pulsating reference frame, the Hamilton equations of the ER3BP still have the Lagrange equilibria in the same positions as the circular problem.

We therefore proceed as follows: for any given libration amplitude $\alpha > d$, we first compute a Lyapunov orbit of the CR3BP of amplitude α, hereafter referred to as the planar Lyapunov orbit. We use this orbit as an input of the FLI method to find orbits of the ER3BP that, in the pulsating frame, remain close to the previous Lyapunov orbit for up to 200 years. We then consider the motions of the Sun and the Earth in the realistic model of the Solar System, and we introduce a new rotating-pulsating reference frame $OXYZ$ in which the Sun and the Earth remain in fixed locations of the X axis, and we map the previous orbit to this reference frame. Finally, since the planetary perturbations introduce oscillations of amplitude d, we define the set $\mathcal{B}$ as a neighbourhood of the previous orbit of amplitude $\rho \in (d, \alpha/10)$, and we find orbits of the realistic model of the Solar System which remain in the set $\mathcal{B}$ for a minimum of 200 years. For $\alpha < 10d$ we apply the method using a ball $\mathcal{B}$ centered at $\mathcal{L}_3$ of radius α. For the minimum value of $\alpha = 2d$ we find an orbit stable up to 250 years in a neighbourhood of $\mathcal{L}_3$.

These results have been published in Scantamburlo and Guzzo (2020), presented at "Asteroid exploration and exploitation - Stardust-R Global Virtual Workshop I" (September 8, 2020), and partially presented at the XLIV Summer School on Mathematical Physics organized by "Gruppo Nazionale per la Fisica Matematica" (September 3, 2019).

2.2 The dynamical substitute of L_3 in the planar multicircular restricted planetary problem

2.2.1 The planar multicircular restricted eight-body problem

As a simplification of our Solar System, we consider a model in which the eight planets of our Solar System (from Mercury to Neptune) are performing circular motions around the Sun in the same orbital plane. We denote by μ and ε_j the gravitational parameters of the Sun and the j-th planet respectively, while by n_j, d_j and ϕ_j the mean motion, orbital radius and the initial phase displacement of the j-th planet. In the heliocentric inertial reference frame Oxy the position of the j-th planet is $\boldsymbol{r}_j(t) = d_j(\cos(n_j t + \phi_j), \sin(n_j t + \phi_j))$, while the position vector of the spacecraft is denoted by $\boldsymbol{r} = (x, y)$. The Lagrangian function describing the dynamics of the spacecraft in the heliocentric inertial reference frame is

$$\mathcal{L}(\boldsymbol{r}, \dot{\boldsymbol{r}}; t) = \frac{\|\dot{\boldsymbol{r}}\|^2}{2} + \frac{\mu}{\|\boldsymbol{r}\|} - \sum_j \varepsilon_j \left(\frac{\boldsymbol{r} \cdot \boldsymbol{r}_j(t)}{\|\boldsymbol{r}_j(t)\|^3} - \frac{1}{\|\boldsymbol{r} - \boldsymbol{r}_j(t)\|} \right) \tag{2.1}$$

In order to compare the dynamics of the system with the dynamics of the Sun-Earth CR3BP, we introduce the co-rotating reference frame OXY, in which the Earth is always located at $(d_3, 0)$ (see Fig. 2.1). For this purpose we introduce the rotation matrix

$$\mathcal{R} = \begin{pmatrix} \cos(n_3 t + \phi_3) & -\sin(n_3 t + \phi_3) \\ \sin(n_3 t + \phi_3) & \cos(n_3 t + \phi_3) \end{pmatrix} \tag{2.2}$$

such that the position vector $\boldsymbol{R}$ of the spacecraft and $\boldsymbol{R}_j$ of the planets in the co-rotating reference frame are given by

$$\boldsymbol{R} = \mathcal{R}^T \boldsymbol{r}, \quad \boldsymbol{R}_j = \mathcal{R}^T \boldsymbol{r}_j. \tag{2.3}$$

We note that $\boldsymbol{R}_j = d_j(\cos(\overline{n}_j t + \overline{\phi}_j), \sin(\overline{n}_j t + \overline{\phi}_j))$, where $\overline{n}_j := n_j - n_3$, $\overline{\phi}_j := \phi_j - \phi_3$, while $\|\boldsymbol{R}\| = \|\boldsymbol{r}\|$, $\|\boldsymbol{R} - \boldsymbol{R}_j\| = \|\boldsymbol{r} - \boldsymbol{r}_j\|$ and

$$\|\dot{\boldsymbol{r}}\|^2 = \|\dot{\boldsymbol{R}}\|^2 + n_3^2 \|\boldsymbol{R}\|^2 + \boldsymbol{R}\dot{\mathcal{R}}^T \mathcal{R}\dot{\boldsymbol{R}} + \dot{\boldsymbol{R}}\mathcal{R}^T \dot{\mathcal{R}}\boldsymbol{R}. \tag{2.4}$$

Since

$$\dot{\mathcal{R}}^T \mathcal{R} = \begin{pmatrix} 0 & n_3 \\ -n_3 & 0 \end{pmatrix}, \quad \mathcal{R}^T \dot{\mathcal{R}} = -\dot{\mathcal{R}}^T \mathcal{R} \tag{2.5}$$

relation (2.4) becomes

$$\|\dot{\boldsymbol{r}}\|^2 = \|\dot{\boldsymbol{R}}\|^2 + n_3^2 \|\boldsymbol{R}\|^2 + 2n_3(X\dot{Y} - \dot{X}Y). \tag{2.6}$$

Then, the Lagrangian function describing the spacecraft dynamics in the heliocentric co-rotating reference frame is

$$\mathcal{L}(X,Y,\dot{X},\dot{Y};t) = \frac{\dot{X}^2+\dot{Y}^2}{2} + \frac{n_3^2}{2}(X^2+Y^2) + n_3(X\dot{Y}-\dot{X}Y) + \frac{\mu}{\sqrt{X^2+Y^2}}$$
$$- \varepsilon_3\left(\frac{X}{d_3^2} - \frac{1}{\sqrt{(X-d_j)^2+Y^2}}\right)$$
$$- \sum_{j\neq 3}\varepsilon_j\left(\frac{X\cos(\overline{n}_j t+\overline{\phi}_j)+Y\sin(\overline{n}_j t+\overline{\phi}_j)}{d_j^2} - \frac{1}{\sqrt{(X-d_j\cos(\overline{n}_j t+\overline{\phi}_j))^2+(Y-d_j\sin(\overline{n}_j t+\overline{\phi}_j))^2}}\right). \tag{2.7}$$

Let us now introduce the Hamiltonian formulation of the problem by computing the Legendre

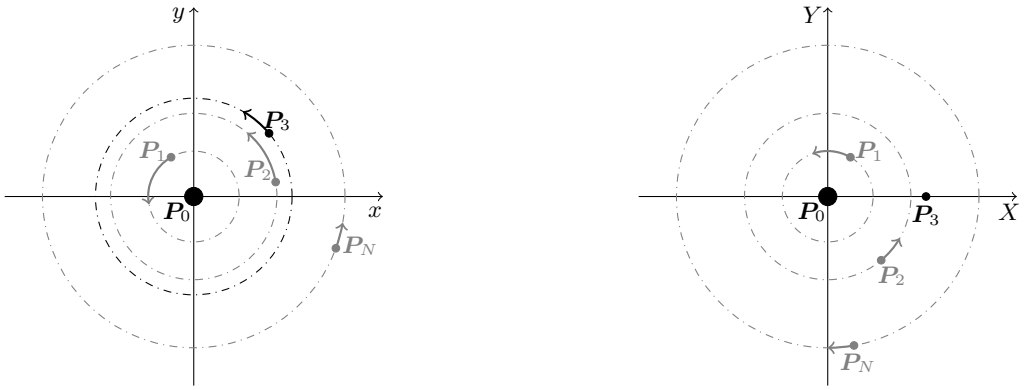

Figure 2.1: Representation of the multicircular restricted N-body model in the heliocentric inertial reference frame (left-hand side) and the heliocentric co-rotating reference frame (right-hand side).

transform of $\mathcal{L}$. Since the conjugate momenta to X and Y are

$$P_X = \frac{\partial \mathcal{L}}{\partial \dot{X}} = \dot{X} - n_3 Y, \quad P_Y = \frac{\partial \mathcal{L}}{\partial \dot{Y}} = \dot{Y} + n_3 X, \tag{2.8}$$

the Hamiltonian function describing the dynamics of the spacecraft in the heliocentric co-rotating reference frame is

$$H(P_X,P_Y,X,Y;t) = H_0(P_X,P_Y,X,Y) + \varepsilon_3 H_3(X,Y) + \sum_{j\neq 3}\varepsilon_j H_j(X,Y;t) \tag{2.9}$$

where

$$H_0 := \frac{P_X^2+P_Y^2}{2} - n_3(XP_Y - YP_X) - \frac{\mu}{\sqrt{X^2+Y^2}} \tag{2.10}$$

$$H_3 := \frac{X}{d_3^2} - \frac{1}{\sqrt{(X-d_3)^2+Y^2}} \tag{2.11}$$

$$H_j := \frac{X\cos(\overline{n}_j t+\overline{\phi}_j)+Y\sin(\overline{n}_j t+\overline{\phi}_j)}{d_j^2} - \frac{1}{\sqrt{(X-d_j\cos(\overline{n}_j t+\overline{\phi}_j))^2+(Y-d_j\sin(\overline{n}_j t+\overline{\phi}_j))^2}}, \tag{2.12}$$

for $j \neq 3$. We note that the Hamiltonian function (2.9) reduces to the Hamiltonian function of the Sun-Earth CR3BP when $\varepsilon_j = 0$ for $j \neq 3$. For this reason, we treat $\sum_{j\neq 3}\varepsilon_j H_j(X,Y;t)$ as

a quasi-periodic time-dependent perturbation of the Sun-Earth CR3BP, which will be reduced to normal form using Hamiltonian perturbation theory.

Precisely, we define a time-dependent close to the identity canonical transformation

$$(P_X, P_Y, X, Y) = \mathcal{C}(\tilde{P}_X, \tilde{P}_Y, \tilde{X}, \tilde{Y}; t) \tag{2.13}$$

conjugating Hamiltonian (2.9) to a new Hamilton function of the form:

$$\tilde{\mathcal{H}}(\tilde{P}_X, \tilde{P}_Y, \tilde{X}, \tilde{Y}; t) = \overline{\mathcal{H}}(\tilde{P}_X, \tilde{P}_Y, \tilde{X}, \tilde{Y}) + \sum_{j\neq 3} \mathcal{R}'(\tilde{P}_X, \tilde{P}_Y, \tilde{X}, \tilde{Y}) + \mathcal{R}''(\tilde{P}_X, \tilde{P}_Y, \tilde{X}, \tilde{Y}; t) \tag{2.14}$$

where

- $$\begin{aligned}\overline{\mathcal{H}} =& \frac{\tilde{P}_X^2 + \tilde{P}_Y^2}{2} - \frac{\mu}{\sqrt{\tilde{X}^2 + \tilde{Y}^2}} - n_3(\tilde{X}\tilde{P}_Y - \tilde{Y}\tilde{P}_X) + \varepsilon_3 \left(\frac{\tilde{X}}{d_3^2} - \frac{1}{\sqrt{(\tilde{X} - d_3)^2 + \tilde{Y}^2}} \right) \\ & - \sum_{j\neq 3} \frac{2\varepsilon_j}{\pi |\sqrt{\tilde{X}^2 + \tilde{Y}^2} - d_j|} \mathcal{K}\left(- \frac{4 d_j \sqrt{\tilde{X}^2 + \tilde{Y}^2}}{(\sqrt{\tilde{X}^2 + \tilde{Y}^2} - d_j)^2} \right)\end{aligned} \tag{2.15}$$

  and:

  $$\mathcal{K}(x) := \int_0^{2\pi} \frac{d\xi}{\sqrt{1 - x \sin^2(\xi)}} \tag{2.16}$$

  is the elliptic function of first kind;

- all the terms $\mathcal{R}'_j$ are of first order in the planetary masses, fourth order in the eccentricity of the spacecraft, and of order $\varepsilon_j \Delta_j^{36}$ where Δ_j^{36} is defined as $\frac{1}{a}\left(\frac{d_j}{a}\right)^{36}$ for $j < 3$, and $\frac{1}{d_j}\left(\frac{a}{d_j}\right)^{36}$ for $j > 3$ (where a denotes the semi-major axis of the spacecraft). We remark that that exponent $N = 36$ of Δ_j has been chosen so that $\varepsilon_j \Delta_j^{36}$ is suitably small;

- $\mathcal{R}''$ is of second order in the planetary masses.

Since $\mathcal{R}'_j$ and $\mathcal{R}''$ are negligible with respect to $\overline{H}$, we consider $\overline{H}$ as the Hamiltonian which captures the main effects of the planetary perturbation on the Lagrangian point L_3 of the CR3BP. In particular, $\overline{H}$ is the sum of the Hamiltonian of the CR3BP and the perturbation

$$- \sum_{j\neq 3} \frac{2\varepsilon_j}{\pi |\sqrt{\tilde{X}^2 + \tilde{Y}^2} - d_j|} \mathcal{K}\left(- \frac{4 d_j \sqrt{\tilde{X}^2 + \tilde{Y}^2}}{(\sqrt{\tilde{X}^2 + \tilde{Y}^2} - d_j)^2} \right). \tag{2.17}$$

In the following we will refer to the Hamiltonian $\overline{H}$ as the averaged Hamiltonian.

2.2.2 Dynamics of the averaged Hamiltonian close to the collinear equilibrium point L_3

The Hamiltonian (2.15) admits an equilibrium point on the axis $\tilde{Y} = 0$ close to the Lagrangian point L_3 of the CR3BP, which we denote by $\mathcal{L}_3$. More precisely, Hamiltonian (2.15) is a small perturbation of the Hamiltonian of the Sun–Earth CR3BP depending on $\tilde{Y}^2$. Therefore, on the

Planet	$X_{\mathcal{L}_3} - X_{L_3}$	$(\eta_{\mathcal{L}_3} - \eta_{L_3})/\eta_{L_3}$	$(\sigma_{\mathcal{L}_3} - \sigma_{L_3})/\sigma_{L_3}$
Mercury	-6.26×10^{-8} AU ~ -9 km	-2.53×10^{-8}	9.18×10^{-9}
Venus	-1.46×10^{-6} AU ~ -218 km	-3.93×10^{-6}	4.66×10^{-6}
Mars	2.85×10^{-8} AU ~ 4 km	-1.99×10^{-7}	2.77×10^{-7}
Jupiter	1.18×10^{-6} AU ~ 176 km	-5.45×10^{-6}	7.73×10^{-6}
Saturn	5.56×10^{-8} AU ~ 8 km	-2.52×10^{-7}	3.58×10^{-7}
Uranus	1.03×10^{-9} AU ~ 0.2 km	-4.66×10^{-9}	6.61×10^{-9}
Neptune	3.16×10^{-10} AU ~ 0.05 km	-1.42×10^{-9}	2.02×10^{-9}

Table 2.1: This table shows the displacement $X_{\mathcal{L}_3} - X_{L_3}$ between the equilibrium point $\mathcal{L}_3$ of the averaged MCR8BP and the L_3 point of the Sun–Earth CR3BP, and the differences between the eigenvalues of $\mathcal{L}_3$ and L_3 for each planet.

one hand the equation:

$$\frac{\partial \overline{H}}{\partial \tilde{Y}}(\tilde{P}_X, \tilde{P}_Y, \tilde{X}, \tilde{Y}) = 0 \tag{2.18}$$

is satisfied by any $(\tilde{P}_X, \tilde{P}_Y, \tilde{X}, \tilde{Y})$ with $\tilde{Y} = 0$, $\tilde{P}_X = 0$; on the other hand the equation

$$\frac{\partial \overline{H}}{\partial \tilde{X}}(0, \tilde{P}_Y, \tilde{X}, 0) = 0 \tag{2.19}$$

has a solution $X_{\mathcal{L}_3}, \tilde{P}_Y = n_3 X_{\mathcal{L}_3}$, with $X_{\mathcal{L}_3}$ close to X_{L_3}. By including in the model all the planets from Mercury to Neptune, we find $X_{\mathcal{L}_3} - X_{L_3} \sim -2.58 \times 10^{-7}$ AU ~ -39 km. More precisely, by computing the individual contribution of each planet to the displacement of $\mathcal{L}_3$ from L_3 (see Table 2.1, where the individual contribution of a planet is computed by setting to zero the masses of all other planets, excepts for the Earth) we find that Venus and Jupiter each move the position of this equilibrium by about 218 and 176 km, respectively, in opposite directions; in the model where both the planets are included, their effects almost perfectly compensate for one another, leaving a displacement of about 40 km only. Table 2.1 shows that the individual contributions of the planets to the eigenvalues of the linearization matrix at $\mathcal{L}_3$ are very small, and do not affect the nature of the equilibrium, which remains partially hyperbolic. As a consequence, around $\mathcal{L}_3$ we find a family of periodic orbits, namely the Lyapunov orbits of $\mathcal{L}_3$.

Before mapping back $\mathcal{L}_3$ to the Cartesian variables, we need to provide the details of the definition of the canonical transformation $\mathcal{C}$.

2.2.3 Averaging the planetary anomalies

The first step to average from the Hamiltonian (2.9) the dependence on the planetary anomalies $\theta_j := \overline{n}_j t + \overline{\phi}_j$ for $j \neq 3$ is to represent it using the *modified Delaunay variables* $(\Lambda, \Phi, \lambda, \varphi)$, which are defined from the Delaunay variables (L, G, l, g) through the relations

$$\Lambda = L, \quad \Phi = L - G, \quad \lambda = l + g, \quad \varphi = -g. \tag{2.20}$$

Let us recall that the Delaunay variables (L, G, l, g) that here we consider in their planar version, are the action-angle variables of the Kepler problem. For example, by considering the Hamiltonian:

$$H(\boldsymbol{p}, \boldsymbol{q}) = \frac{\|\boldsymbol{p}\|^2}{2} - \frac{\mu}{\|\boldsymbol{q}\|}, \tag{2.21}$$

and by denoting with a, e, M, ω the semi-major axis, the eccentricity, the mean anomaly, and the argument of perihelion of its elliptic solutions, the variables:

$$L := \sqrt{\mu a}, \quad G := \sqrt{\mu a(1-e^2)}, \quad l := M, \quad g := \omega \tag{2.22}$$

are canonical (L and G are the momenta conjugate to l and g respectively) and conjugate the Hamiltonian (2.21) to

$$\mathcal{H}(L) = -\frac{\mu^2}{2L^2}. \tag{2.23}$$

Both the angles l, g are not defined on the circular orbits. Therefore, it is more convenient to use the modified Delaunay variables (2.20), since the angle λ is well defined also if $e = 0$.

Next, we need to explicitly represent the perturbation as a function of these variables so that the Hamiltonian (2.9) is conjugate to:

$$\mathcal{W}(\Lambda, \Phi, \Theta, \lambda, \varphi, \theta) = \mathcal{W}_0(\Lambda, \Phi) + \sum_{j\neq 3} \overline{n}_j \Theta_j + \varepsilon_3 \mathcal{W}_3(\Lambda, \Phi, \lambda, \varphi) + \sum_{j\neq 3} \varepsilon_j \mathcal{W}_j(\Lambda, \Phi, \lambda, \varphi, \theta_j) \tag{2.24}$$

where Θ_j, θ_j are convenient additional conjugate variables so that $\mathcal{W}$ is autonomous and depends periodically on the angles θ_j,

$$\mathcal{W}_0 := -\frac{\mu^2}{2\Lambda^2} - n_3(\Lambda - \Phi). \tag{2.25}$$

$\mathcal{W}_j$ are conjugate to $\mathcal{H}_j$. We remark that $\mathcal{W}_3$ does not depend on any θ_3, and therefore it will not be averaged with respect to the planetary anomalies, while for $j \neq 3$, $\mathcal{W}_j$ depends periodically on θ_j.

Let us now consider the Fourier expansion of $\mathcal{W}_j$ with respect to the angles $\lambda, \varphi, \theta_j$. As a consequence of the well known D'Alembert rules, the expansion is limited to cosine terms:

$$\cos(i_1\lambda + i_2\varphi + i_3\theta_j), \quad i_1, i_2, i_3 \in \mathbb{Z}, \tag{2.26}$$

with $i_1 = i_2 + i_3$. As a matter of fact, this is a consequence of the invariance of $\mathcal{W}_j$ with respect to rotations around the axis passing at the origin and perpendicular to the xy plane. For further reference about the D'Alembert rules, the reader is referred to Morbidelli (2011). Therefore, the function $\mathcal{W}_j$ has the following Fourier series representation:

$$\mathcal{W}_j = \sum_{i_2, i_3 \in \mathbb{Z}} \hat{\mathcal{W}}^j_{i_2,i_3}(\Lambda, \Phi) \cos((i_2 + i_3)\lambda + i_2\varphi + i_3\theta_j). \tag{2.27}$$

In the explicit computations the expansion is limited to $|i_2| \leq 3$, and $|i_3| \leq 35$, which corresponds to neglect the terms which are of order e^4 and Δ_j^{36}. Precisely, the explicit computation of the Fourier coefficients $\hat{\mathcal{W}}^j_{i_2,i_3}(\Lambda, \Phi)$ is done by first representing H_j using the orbital parameters a, e, f, ω, and then by representing f as a function of M and e, and by computing the Taylor expansion up to order 3. Finally, we replace a, e, M, ω with the modified Delaunay elements.

For this purpose, we first write the perturbations H_j in terms of the orbital elements:

$$H_j = \frac{\rho}{d_j^2}\cos(f + \omega - n_j t - \phi_j) - \frac{1}{\sqrt{\rho^2 + d_j^2 - 2\rho d_j \cos(f + \omega - n_j t - \phi_j)}} \tag{2.28}$$

where $\rho = \frac{a(1-e^2)}{1+e\cos(f)}$. Then, by using the well known series expansion

$$\frac{1}{\sqrt{1+\eta^2-2\eta\cos(\gamma)}} = \sum_{i\geq 0} P_i(\cos(\gamma))\eta^i \qquad \eta \in (-1,1),\ \gamma \in [0,2\pi], \tag{2.29}$$

where P_i represents the Legendre polynomial of i-th degree, we obtain

$$H_j = \frac{\rho\cos(f+\omega-n_3t-\phi_3)}{d_3^2} - \frac{1}{\rho}\sum_{i\geq 0}\left(\frac{d_j}{\rho}\right)^i P_i(\cos(f+\omega-n_jt-\phi_j)) \qquad \text{for } j<3 \tag{2.30}$$

as well as:

$$H_j = \frac{\rho\cos(f+\omega-n_3t-\phi_3)}{d_3^2} - \frac{1}{d_j}\sum_{i\geq 0}\left(\frac{\rho}{d_j}\right)^i P_i(\cos(f+\omega-n_jt-\phi_j)) \qquad \text{for } j>3. \tag{2.31}$$

Next, the true anomaly f is written in term of the mean anomaly l; using the standard formula:

$$l = \int_0^f \frac{(1-e^2)^{3/2}}{(1+e\cos(x))^2}dx. \tag{2.32}$$

For small values of the eccentricity e, the integrand is expanded in in power series of e:

$$l = \int_0^f \sum_{i\geq 0} e^i v_i(x)dx \tag{2.33}$$

with $v_i(x) = \frac{1}{i!}\frac{\partial^i}{\partial e^i}\left(\frac{(1-e^2)^{3/2}}{(1+e\cos(x))^2}\right)\Big|_{e=0}$. Hence, the relation (2.33) assumes the form

$$l = f + e\xi(f) \tag{2.34}$$

where $\xi = \int_0^f \left(\sum_{i\geq 0} e^{i-1}v_i(x)\right)dx - f$; then $f = l - e\xi(f) = l - e\xi(l - e\xi(f)) = \ldots$, and by expanding in terms of the eccentricity, we obtain the series:

$$f = l + \sum_{k\geq 1} e^k \xi_k(l) \tag{2.35}$$

where ξ_k are functions which are explicitly computed.

The canonical transformation averaging from the terms $\mathcal{W}_j$ the dependence on the planetary mean anomalies is constructed using the standard Lie method, which has been described in Sec. 1.3.2. Given a generating function χ, suitably small, its Hamiltonian flow ϕ_χ^1 at time 1 is a canonical transformation:

$$\phi_\chi^1(\tilde{\Lambda},\tilde{\Phi},\tilde{\Theta},\tilde{\lambda},\tilde{\varphi},\tilde{\theta}) = (\Lambda,\Phi,\Theta,\lambda,\varphi,\theta) \tag{2.36}$$

which is close to the identity, satisfies

$$\begin{aligned}
\Lambda &= \tilde{\Lambda} + \{\tilde{\Lambda}, \chi\} + \mathcal{O}_2(\chi) \\
\Phi &= \tilde{\Phi} + \{\tilde{\Phi}, \chi\} + \mathcal{O}_2(\chi) \\
\Theta &= \tilde{\Theta} + \{\tilde{\Theta}, \chi\} + \mathcal{O}_2(\chi) \\
\lambda &= \tilde{\lambda} + \{\tilde{\lambda}, \chi\} + \mathcal{O}_2(\chi) \\
\varphi &= \tilde{\varphi} + \{\tilde{\varphi}, \chi\} + \mathcal{O}_2(\chi) \\
\theta &= \tilde{\theta},
\end{aligned} \tag{2.37}$$

and conjugates the Hamiltonian function $\mathcal{W}$ to

$$\tilde{\mathcal{W}} = \mathcal{W} \circ \phi^1_\chi(\tilde{\Lambda}, \tilde{\Phi}, \tilde{\Theta}, \tilde{\lambda}, \tilde{\varphi}, \tilde{\theta}) = \mathcal{W} + \{\mathcal{W}, \chi\} + \mathcal{O}_2(\chi). \tag{2.38}$$

By defining

$$\chi := \sum_{j \neq 3} \varepsilon_j \chi_j \tag{2.39}$$

with

$$\chi_j := \sum_{|i_2| \leq 3, |i_3| \leq 35} \hat{\chi}^j_{i_2,i_3}(\tilde{\Lambda}, \tilde{\Phi}) \sin\Big((i_2 + i_3)\tilde{\lambda} + i_2\tilde{\varphi} + i_3\tilde{\theta}_j\Big)$$

and

$$\hat{\chi}^j_{i_2,i_3} := \delta_{i_3} \frac{\mathcal{W}^j_{i_2,i_3}}{(i_2 + i_3)\omega_\lambda + i_2\omega_\varphi + i_3\omega_{\theta_j}} \tag{2.40}$$

$\delta_0 = 0$ and $\delta_i = 1$ for $i \neq 0$, while

$$\omega_\lambda := \frac{\partial \mathcal{W}_0}{\partial \tilde{\Lambda}}, \quad \omega_\varphi := \frac{\partial \mathcal{W}_0}{\partial \tilde{\Phi}}, \quad \omega_{\theta_j} := \overline{n}_j,$$

we obtain

$$\mathcal{W} \circ \phi^1_\chi(\tilde{\Lambda}, \tilde{\Phi}, \tilde{\Theta}, \tilde{\lambda}, \tilde{\varphi}, \tilde{\theta}) = \overline{\mathcal{W}}(\tilde{\Lambda}, \tilde{\Phi}, \tilde{\lambda}, \tilde{\varphi}) + \sum_{j \neq 3} \overline{n}_j \tilde{\Theta}_j + \mathcal{O}(\varepsilon_j^2) \tag{2.41}$$

where

$$\overline{\mathcal{W}} = \mathcal{W}_0(\tilde{\Lambda}, \tilde{\Phi}) + \varepsilon_3 \mathcal{W}_3(\tilde{\Lambda}, \tilde{\Phi}, \tilde{\lambda}, \tilde{\varphi}) + \sum_{j \neq 3} \sum_{i_2 \in \mathbb{Z}} \varepsilon_j \hat{\mathcal{W}}^j_{i_2,0}(\tilde{\Lambda}, \tilde{\Phi}) \cos\Big(i_2(\tilde{\lambda} + \tilde{\varphi})\Big) \tag{2.42}$$

does not depend on $\tilde{\theta}_j$. The averaged Hamiltonian $\overline{\mathcal{W}}$ has a convenient Cartesian representation. Therefore, let us consider the transformation $(\tilde{P}_X, \tilde{P}_Y, \tilde{X}, \tilde{Y}) = \mathcal{D}(\tilde{\Lambda}, \tilde{\Phi}, \tilde{\lambda}, \tilde{\varphi})$ mapping the averaged modified Delaunay variables to the averaged Cartesian coordinates $(\tilde{P}_X, \tilde{P}_Y, \tilde{X}, \tilde{Y})$; then $\overline{H} := \mathcal{W} \circ \mathcal{D}^{-1}$ is computed from:

$$\mathcal{W}_0 \circ \mathcal{D}^{-1} = \frac{\tilde{P}_X^2 + \tilde{P}_Y^2}{2} - \frac{\mu}{\sqrt{\tilde{X}^2 + \tilde{Y}^2}} - n_3(\tilde{X}\tilde{P}_Y - \tilde{Y}\tilde{P}_X) \tag{2.43}$$

$$\varepsilon_3 \mathcal{W}_3 \circ \mathcal{D}^{-1} = \varepsilon_3 \left(\frac{\tilde{X}}{d_3^2} - \frac{1}{\sqrt{(\tilde{X} - d_3)^2 + \tilde{Y}^2}} \right) \tag{2.44}$$

$$\sum_{i_2\in\mathbb{Z}} \varepsilon_j \hat{\mathcal{W}}^j_{i_2,0} \cos\Big(i_2(\tilde{\lambda}+\tilde{\varphi})\Big)\circ\mathcal{D}^{-1} = \frac{\varepsilon_j}{2\pi}\int_0^{2\pi}\left[\frac{\tilde{X}\cos\tilde{\theta}_j+\tilde{Y}\sin\tilde{\theta}_j}{d_j^2} - \frac{1}{\sqrt{(\tilde{X}-d_j\cos\tilde{\theta}_j)^2+(\tilde{Y}-d_j\sin\tilde{\theta}_j)^2}}\right]d\tilde{\theta}_j \tag{2.45}$$
$$= -\frac{\varepsilon_j}{2\pi}\int_0^{2\pi}\frac{d\tilde{\theta}_j}{\sqrt{(\tilde{X}-d_j\cos\tilde{\theta}_j)^2+(\tilde{Y}-d_j\sin\tilde{\theta}_j)^2}}.$$

The last of equations (2.45) represents the main effects of the planetary perturbation on the Sun–Earth L_3. It corresponds to the Fourier average of $\mathcal{W}_j$ with respect to θ_j, represented with Cartesian variables. Therefore, it can be obtained by computing the Fourier average of H_j directly using the Cartesian variables. The right hand side of the third equation in (2.45) can be further expressed using an elliptic function. Precisely, by representing $\tilde{X}=\sqrt{\tilde{X}^2+\tilde{Y}^2}\cos\tilde{f}$ and $\tilde{Y}=\sqrt{\tilde{X}^2+\tilde{Y}^2}\sin\tilde{f}$, where $\tilde{f}$ is the polar angle associated to $(\tilde{X},\tilde{Y})$ in the $O\tilde{X}\tilde{Y}$ reference frame, we have:

$$\begin{aligned}(\tilde{X}-d_j\cos\tilde{\theta}_j)^2+(\tilde{Y}-d_j\sin\tilde{\theta}_j)^2 &= \tilde{X}^2+\tilde{Y}^2+d_j^2-2d_j\sqrt{\tilde{X}^2+\tilde{Y}^2}\Big(\cos\tilde{f}\cos\tilde{\theta}_j+\sin\tilde{f}\sin\tilde{\theta}_j\Big)\\ &= \tilde{X}^2+\tilde{Y}^2+d_j^2-2d_j\sqrt{\tilde{X}^2+\tilde{Y}^2}\cos(\tilde{f}-\tilde{\theta}_j)\\ &= \Big(\sqrt{\tilde{X}^2+\tilde{Y}^2}-d_j\Big)^2+2d_j\sqrt{\tilde{X}^2+\tilde{Y}^2}\Big(1-\cos(\tilde{f}-\tilde{\theta}_j)\Big)\\ &= \Big(\sqrt{\tilde{X}^2+\tilde{Y}^2}-d_j\Big)^2+4d_j\sqrt{\tilde{X}^2+\tilde{Y}^2}\sin^2\tilde{\beta}_j\end{aligned} \tag{2.46}$$

where $\tilde{\beta}_j := \frac{\tilde{f}-\tilde{\theta}_j}{2}$. Then we obtain

$$\begin{aligned}\int_0^{2\pi}\frac{d\tilde{\theta}_j}{\sqrt{(\tilde{X}-d_j\cos\tilde{\theta}_j)^2+(\tilde{Y}-d_j\sin\tilde{\theta}_j)^2}} &= 4\int_0^{\pi/2}\frac{d\tilde{\beta}_j}{\sqrt{\Big(\sqrt{\tilde{X}^2+\tilde{Y}^2}-d_j\Big)^2+4d_j\sqrt{\tilde{X}^2+\tilde{Y}^2}\sin^2\tilde{\beta}_j}}\\ &= \frac{4}{|\sqrt{\tilde{X}^2+\tilde{Y}^2}-d_j|}\mathcal{K}\left(-\frac{4d_j\sqrt{\tilde{X}^2+\tilde{Y}^2}}{\Big(\sqrt{\tilde{X}^2+\tilde{Y}^2}-d_j\Big)^2}\right),\end{aligned} \tag{2.47}$$

as well as:

$$\sum_{i_2\in\mathbb{Z}} \varepsilon_j \hat{\mathcal{W}}^j_{i_2,0} \cos\Big(i_2(\tilde{\lambda}+\tilde{\varphi})\Big)\circ\mathcal{D}^{-1} = -\frac{2\varepsilon_j}{\pi|\sqrt{\tilde{X}^2+\tilde{Y}^2}-d_j|}\mathcal{K}\left(-\frac{4d_j\sqrt{\tilde{X}^2+\tilde{Y}^2}}{\Big(\sqrt{\tilde{X}^2+\tilde{Y}^2}-d_j\Big)^2}\right). \tag{2.48}$$

Therefore, the Hamiltonian averaged with respect to the mean anomalies of all the planets, except for the Earth, is:

$$\begin{aligned}\overline{\mathcal{H}} =& \frac{\tilde{P}_X^2+\tilde{P}_Y^2}{2}-\frac{\mu}{\sqrt{\tilde{X}^2+\tilde{Y}^2}}-n_3(\tilde{X}\tilde{P}_Y-\tilde{Y}\tilde{P}_X)+\varepsilon_3\left(\frac{\tilde{X}}{d_3^2}-\frac{1}{\sqrt{(\tilde{X}-d_3)^2+\tilde{Y}^2}}\right)\\ &-\sum_{j\neq 3}\frac{2\varepsilon_j}{\pi|\sqrt{\tilde{X}^2+\tilde{Y}^2}-d_j|}\mathcal{K}\left(-\frac{4d_j\sqrt{\tilde{X}^2+\tilde{Y}^2}}{(\sqrt{\tilde{X}^2+\tilde{Y}^2}-d_j)^2}\right).\end{aligned} \tag{2.49}$$

2.2.4 Mapping $\mathcal{L}_3$ in the original phase-space: the dynamical substitute of L_3

Finally, we map back $\mathcal{L}_3$ to the original phase-space through the flow at time 1 of the generating function χ defined in Eq. (2.39). We note that $\mathcal{L}_3$ is characterized by a small value of the eccentricity[1] (about 10^{-6}). Since for $e = 0$ the angle $\tilde{\varphi}$ is not defined (the argument of perihelion is not defined for circular motions) and the action $\tilde{\Phi}$ is null, it is mandatory to introduce the canonical Poincaré variables $(\tilde{\Lambda}, \tilde{p}, \tilde{\lambda}, \tilde{q})$, where

$$\tilde{p} = \sqrt{2\tilde{\Phi}}\cos\tilde{\varphi}, \quad \tilde{q} = \sqrt{2\tilde{\Phi}}\sin\tilde{\varphi}, \tag{2.50}$$

that are well defined also for $e = 0$. Since the time-span of interest for astrodynamics is limited at most by few centuries, in the transformation mapping the averaged to the original variables, we neglect the terms proportional to the product of two gravitational parameters; i.e. we approximate the Lie series by retaining only the first two terms, i.e.

$$\begin{aligned} \Lambda &= \tilde{\Lambda} + \{\tilde{\Lambda}, \chi\} \\ p &= \tilde{p} + \{\tilde{p}, \chi\} \\ \lambda &= \tilde{\lambda} + \{\tilde{\lambda}, \chi\} \\ q &= \tilde{q} + \{\tilde{q}, \chi\}. \end{aligned} \tag{2.51}$$

Moreover, we emphasize that for small values of the eccentricity $\tilde{e}$ we get $\tilde{\Phi} \sim \frac{\tilde{e}^2}{2}$; hence when the eccentricity is small, both $\tilde{p}$ and $\tilde{q}$ are proportional to $\tilde{e}$. Taking advantage of the small value of the eccentricity of $\mathcal{L}_3$, the numerical computation of the right-hand sides of Eq. (2.51) can be done by neglecting the terms depending on $\tilde{p}, \tilde{q}$ at orders equal to or higher than four and for $\tilde{\theta} = (\overline{n}_1 t + \overline{\phi}_1, \ldots, \overline{n}_8 t + \overline{\phi}_8)$. Finally, we transform back to the Cartesian variables and we obtain the dynamical substitute of $\mathcal{L}_3$ as a quasi-periodic function of time:

$$(P_{X,\mathcal{L}_3}(t), P_{Y,\mathcal{L}_3}(t), X_{\mathcal{L}_3}(t), Y_{\mathcal{L}_3}(t)) := (P_X(\tilde{\theta}), P_Y(\tilde{\theta}), X(\tilde{\theta}), Y(\tilde{\theta})). \tag{2.52}$$

In the simpler bicircular four-body problems, Sun–Earth–(j-th planet) (for further details, the reader is referred to Andreu, 1998; Jorba, 2012; Barrabés et al., 2016; A.F.B de Almeida Prado, 2005; Jorba and Nicolás, 2020), the dynamical substitute $(P_{X,\mathcal{L}_3}(t), P_{Y,\mathcal{L}_3}(t), X_{\mathcal{L}_3}(t), Y_{\mathcal{L}_3}(t))$ is a periodic function of time with frequency $\overline{n}_j$.

In order to verify that there is a real orbit for the restricted problem that remains close to the dynamical substitute $(X_{\mathcal{L}_3}(t), Y_{\mathcal{L}_3}(t))$ for times that are of interest for astrodynamics, we numerically integrate the equations of motion of the restricted problem with initial conditions $(P_X(0), P_Y(0), X(0), Y(0)) = (P_{X,\mathcal{L}_3}(0), P_{Y,\mathcal{L}_3}(0), X_{\mathcal{L}_3}(0), Y_{\mathcal{L}_3}(0))$. In Fig. 2.2 we present the dynamical substitutes of $\mathcal{L}_3$ computed by integrating the initial datum for four cases: the Sun–Earth–Venus, Sun–Earth–Jupiter, Sun–Earth–Venus–Jupiter, and the complete system (namely the system containing all eight planets) with $\overline{\phi}_j = 0$ for all $j \neq 3$. In Table 2.2 we also present the libration amplitudes for each restricted Sun–Earth–(j-th planet) problem. We find that in the MCR8BP, the orbit is a quasi-periodic oscillation around L_3 with amplitude $d \sim 10^{-4}$ AU. Each orbit in a neighbourhood of $\mathcal{L}_3$ can be mapped back to the original Cartesian variables using the canonical transformation (2.51) and $\mathcal{D}$; for example, the periodic Lyapunov orbits will be mapped

[1] The reader is referred to Appendix A for more details on the computation of the orbital elements.

Planet	Dynamical substitute amplitude
Mercury	6.28×10^{-8} AU ~ 9 km
Venus	4.42×10^{-5} AU ~ 6612 km
Mars	1.07×10^{-5} AU ~ 1595 km
Jupiter	4.17×10^{-5} AU ~ 6245 km
Saturn	2.26×10^{-6} AU ~ 338 km
Uranus	5.47×10^{-8} AU ~ 8 km
Neptune	2.04×10^{-8} AU ~ 3 km

Table 2.2: Amplitudes of the dynamical substitutes for each bicircular restricted four-body Sun–Earth–planet problem.

back to quasi-periodic orbits of amplitudes larger than d. Therefore, in the MCR8BP we have a family of quasi-periodic oscillations around L_3 of amplitudes $\alpha > d$.

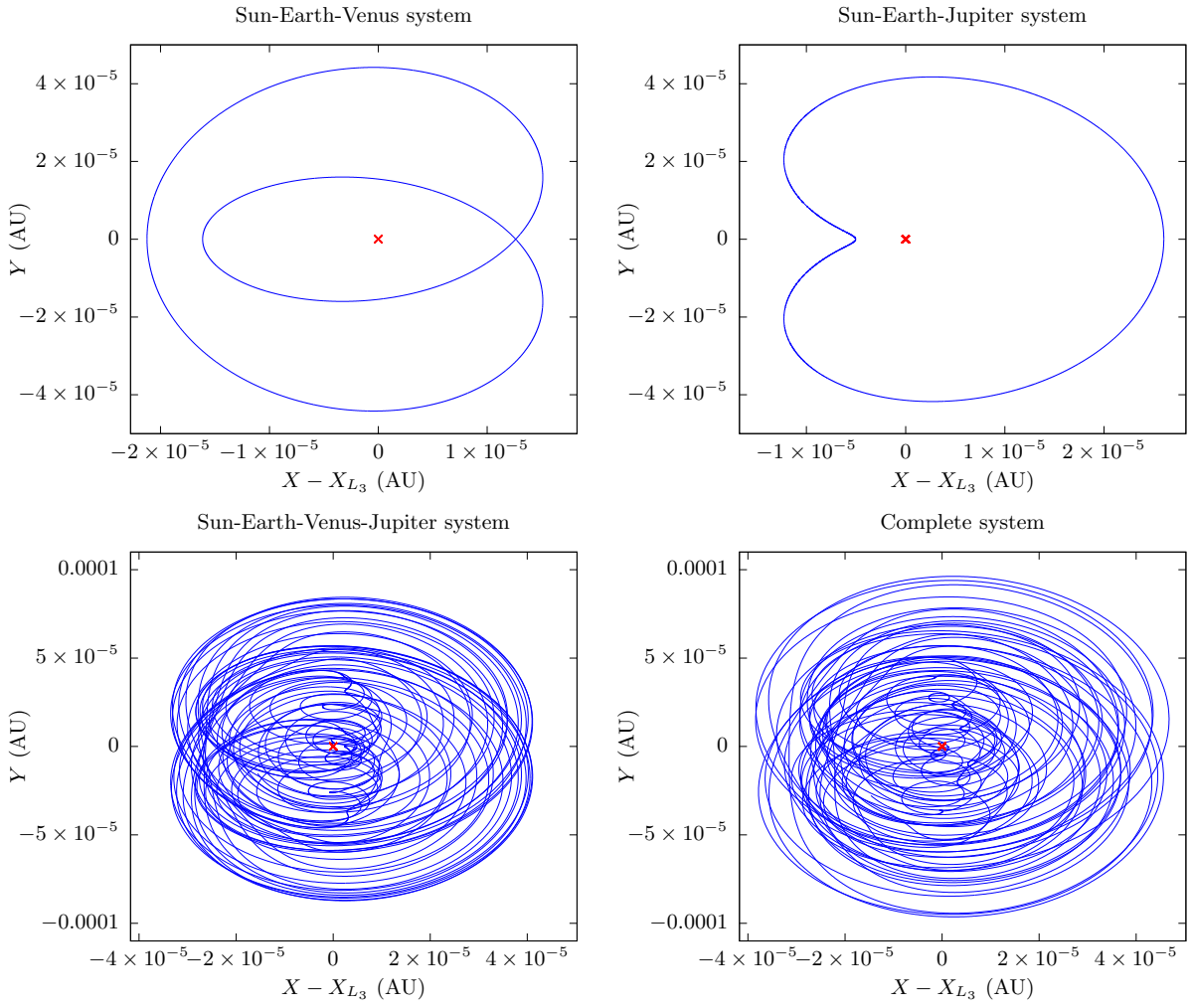

Figure 2.2: Dynamical substitutes of L_3 obtained via numerical integration in the Sun–Earth–Venus, Sun–Earth–Jupiter, Sun–Earth–Venus–Jupiter and complete systems; for all the four panels we considered $\overline{\phi}_j = 0$ for all $j \neq 3$. The time-span for both the Sun–Earth–Venus–Jupiter and the complete system is about 50 years. The red point indicates the location of the Sun–Earth L_3 point. Credit: E. Scantamburlo and M. Guzzo, A&A, 638, A137, 2020, reproduced with permission ©ESO.

2.3 Librations in a realistic model of the Solar System

2.3.1 A realistic model of the Solar System and the rotating-pulsating reference frame

As the restricted multicircular model represents just a simplified model of our Solar System, we must investigate whether or not orbits close to L_3 exist when the trajectories of the planets are realistic. Furthermore, as the effects of Mercury on both the dynamical substitute and in the change of the other planets ephemerides are negligible for the short time intervals that we are taking into account, we consider a model of the Solar System that includes the planets from Venus to Neptune.

Let $\boldsymbol{r} = (x, y, z)$ and $\boldsymbol{v} = (v_x, v_y, v_z)$ denote the position and velocity vectors of the spacecraft, and let $\boldsymbol{r}_j = (x_j, y_j, z_j)$ and $\boldsymbol{v}_j = (v_{x,j}, v_{y,j}, v_{z,j})$ denote the position and velocity vectors of the j-th planet[2] in the Heliocentric inertial reference frame. The equation of motion of the ten-body problem in the Heliocentric inertial reference frame are

$$\begin{aligned} \ddot{\boldsymbol{r}} &= -\sum_j \varepsilon_j \left(\frac{\boldsymbol{r} - \boldsymbol{r}_j}{\|\boldsymbol{r} - \boldsymbol{r}_j\|^3} + \frac{\boldsymbol{r}_j}{\|\boldsymbol{r}_j\|^3} \right) - \mu \frac{\boldsymbol{r}}{\|\boldsymbol{r}\|^3} \\ \ddot{\boldsymbol{r}}_j &= -\sum_{i \neq j} \varepsilon_i \left(\frac{\boldsymbol{r}_j - \boldsymbol{r}_i}{\|\boldsymbol{r}_j - \boldsymbol{r}_i\|^3} + \frac{\boldsymbol{r}_i}{\|\boldsymbol{r}_i\|^3} \right) - (\mu + \varepsilon_j) \frac{\boldsymbol{r}_j}{\|\boldsymbol{r}_j\|^3} \qquad \text{for } j = \{2, \ldots, 8\}, \end{aligned} \tag{2.53}$$

where μ and ε_j denote the gravitational parameter of the Sun and the j-th planet respectively. The equations of motion for the planets will be numerically integrated for initial conditions provided by the JPL digital ephemerides service at some selected initial epochs. In particular, for the numerically computed planetary solution, the orbit of the Earth is not circular, and we have to identify a configuration generalizing the Lagrangian point L_3 of the CR3BP in this more realistic system. First we introduce a Heliocentric rotating-pulsating reference frame $OXYZ$, whose Cartesian axes are parallel, at any time t, to the unit vectors

$$\boldsymbol{e}_r := \frac{\boldsymbol{r}_3}{\|\boldsymbol{r}_3\|}, \quad \boldsymbol{e}_n := \frac{\boldsymbol{v}_3 \times \boldsymbol{r}_3}{\|\boldsymbol{v}_3 \times \boldsymbol{r}_3\|}, \quad \boldsymbol{e}_t := \frac{\boldsymbol{r}_3 \times \boldsymbol{e}_n}{\|\boldsymbol{r}_3 \times \boldsymbol{e}_n\|}. \tag{2.54}$$

In such a reference frame, the Earth state vector is $(1, 0, 0, 0, 0, 0)$ at any time t. We apply the FLI method in order to find orbits staying close to L_3 in the realistic model for centuries; this method provides initial conditions of trajectories remaining in a given neighbourhood $\mathcal{B}$ of a libration orbit found in an approximated model. For the definition of $\mathcal{B}$ we have to consider both the amplitude of the libration orbit and the differences between the realistic model and the CR3BP due to Earth's elliptic orbit. Hence, for the application of the FLI method we first compute a planar Lyapunov orbit of the CR3BP with amplitude α and then we use this orbit to find librations in the ER3BP remaining close to it. We denote these librations by $\ell(\alpha)$ and the details of their computation are explained in Sec. 2.3.3. By assuming that the planetary perturbations introduce additional oscillations of amplitude d comparable to those found in the MCR8BP, we finally look for hyperbolic orbits of the realistic model which remain in a neighbourhood of radius $2d$ of the reference orbit $\ell(\alpha)$ for centuries (Sec. 2.3.4). We compute both $\ell(\alpha)$ of the ER3BP for different orders of the amplitude and the libration orbits in the realistic model of the Solar System using the recent version

[2] $j = 2$ indicates Venus, $j = 3$ the Earth, $j = 4$ Mars, $j = 5$ Jupiter, $j = 6$ Saturn, $j = 7$ Uranus and $j = 8$ Neptune.

of the modified FLI method. For a schematic description of the intermediate models use, the reader

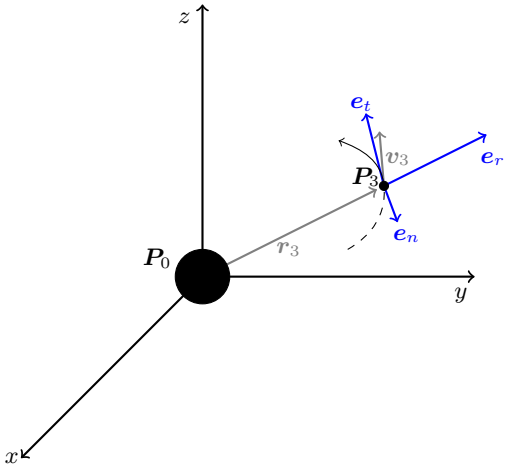

Figure 2.3: Representation of the Heliocentric reference frame and the rotating-pulsating reference frame unit vectors.

is referred to Fig. 2.4.

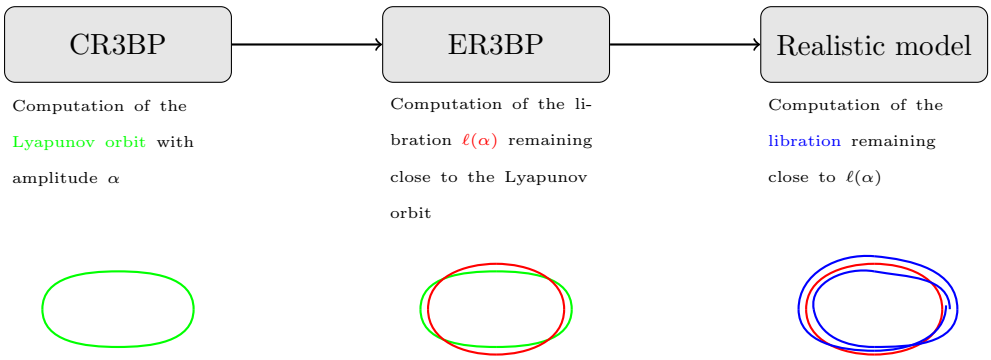

Figure 2.4: Use of the intermediate models for the computation of the libration orbits in the realistic model.

2.3.2 The modified FLI method

The FLI method was originally introduced by Froeschlé et al. (1997b,a) to numerically distinguish between regular and chaotic orbits. In recent years, the method has been modified in order to compute hyperbolic orbits of dynamical systems and their asymptotic solutions: Guzzo and Lega (2014, 2018) and Lega and Guzzo (2016a); Guzzo and Lega (2021) provide a detailed theoretical justification of the method, with a focus on the computation of transit orbits of the Sun–Jupiter system in the CR3BP; in Guzzo and Lega (2015, 2017) the method has been adapted to compute the collision manifold of the comet 67P/Churyumov-Gerasimenko in a model of the Solar System that is compatible with the JPL digital ephemerides. We refer to Chapter 1 for more details about the FLI method, in its different formulations. We continue here to discuss its application to the problem of finding orbits which librate around the equilibrium L_3 of the Sun–Earth system, in a model which is compatible with the ephemerides of the Solar System. At this purpose, we describe an implementation of the method which considers the theoretical results previously described for the intermediate models, starting from the CR3BP and then considering the ER3BP and the MCR8BP.

We recall that in this context, since we are considering the point L_3 of the Sun–Earth system, the CR3BP provides only a very preliminary approximation. The extension from the CR3BP to the realistic one required a new strategy based on the preliminary study of intermediate models to include the planetary perturbations and the eccentricity of the Earth's orbit. In this way we first find the orbit $\ell(\alpha)$ of the Sun–Earth ER3BP, and then the libration orbits of the realistic model of the Solar System. In particular, this usage of the chaos indicator provides an innovative and novel application of dynamical systems theory to astrodynamics, where the short-periodic perturbations represent a relevant part of the model.

Let us recall how the modified FLI is introduced. We first consider the spacecraft equations of motion written as a system of first-order differential equations:

$$\dot{\boldsymbol{\xi}} = F(\boldsymbol{\xi}, t), \tag{2.55}$$

where $\boldsymbol{\xi}$ denotes the state vector of the spacecraft. For simplicity, we choose as epoch $t = 0$ the time of the Earth passage to the perihelion. The variational equations of (2.55) are

$$\dot{\boldsymbol{\Xi}} = \left[\frac{\partial F}{\partial \boldsymbol{\xi}}(\boldsymbol{\xi}, t)\right] \boldsymbol{\Xi} \qquad \boldsymbol{\Xi} \in \mathbb{R}^6, \tag{2.56}$$

where $\frac{\partial F}{\partial \boldsymbol{\xi}}$ denotes the Jacobian matrix of F.

Since we aim to find orbits that remain in a neighbourhood $\mathcal{B}$ of a given target hyperbolic (or partially hyperbolic) orbit γ as long as possible, we introduce the window function $w(\boldsymbol{R})$ and the modified FLI defined as

$$w(\boldsymbol{R}) = \begin{cases} 1 & \text{if } \boldsymbol{R} \in \mathcal{B} \\ 0 & \text{otherwise} \end{cases}, \tag{2.57}$$

$$\mathrm{mFLI}(\boldsymbol{\xi}_0, \boldsymbol{\Xi}_0; T) := \max_{t \in [0,T]} \int_0^t \max\left(0, w(\boldsymbol{R}(s)) \frac{\boldsymbol{\Xi}(s) \cdot \dot{\boldsymbol{\Xi}}(s)}{\|\boldsymbol{\Xi}(s)\|^2}\right) ds, \tag{2.58}$$

respectively, where $\boldsymbol{R}(s)$ denotes the position vector of the spacecraft in the rotating-pulsating reference frame (computed from the numerical solution of the differential equations (2.55) with initial condition $\boldsymbol{\xi}_0$) and $\boldsymbol{\Xi}(s)$ is the solution of the variational equations (2.56) with $\boldsymbol{\Xi}_0$ as initial tangent vector.

When the target orbit γ is partially hyperbolic and $\mathcal{B}$ is suitably small, the only possibility for an orbit to increase the modified FLI to the highest possible values is to remain very close to the target over the whole time interval $[0, T]$. Here, we have two possible cases:

i) a large measure set $\mathcal{B}_I \subset \mathcal{B}$ of initial conditions corresponds to solutions that exit from $\mathcal{B}$ in a short time T_0 and whose mFLI does not increase for $T > T_0$;

ii) a small measure set $\mathcal{B}_{II} \subset \mathcal{B}$ corresponds to solutions which do not exit from $\mathcal{B}$, remain close to a partially hyperbolic orbit of $\mathcal{B}$, and whose mFLI increases linearly with the T (for further details, the reader is referred to Guzzo and Lega, 2014).

Orbits that come back to or enter the set $\mathcal{B}$, but do not stay close to the target orbit over the time interval of interest $[0, T]$ necessarily enter the set $\mathcal{B}_I$ and exit from $\mathcal{B}$ in a short time T_0. Therefore the modified FLI sharply identifies the orbit of ii) when it is computed on grids of initial conditions that are transverse to $\mathcal{B}_{II}$. The key factor for the success of the method is the suitable choice

of the set $\mathcal{B}$ and of the grid of initial conditions, which is clearly suggested by the application of perturbation theories to the approximated models that we have previously studied.

2.3.3 Computation of libration orbits in the ER3BP

The Sun–Earth ER3BP deals with the study of the dynamics of a spacecraft which is gravitationally attracted by the Sun and the Earth while the latter performs an elliptic motion around the Sun. In order to compare the ER3BP with the CR3BP, the equations of motion of the ER3BP have been formulated in the rotating-pulsating reference frame.

In order to find the orbits $\ell(\alpha)$ of the ER3BP, we use the modified FLI (2.58) using a planar Lyapunov orbit of the CR3BP of libration amplitude α as target orbit γ. The set $\mathcal{B}$ is then defined as a neighbourhood of γ with amplitude $\tilde{d}$; if $(X_0, 0, 0, 0, V_{Y,0}, 0)$ is a point of the target Lyapunov orbit, we choose the grid of initial data as the set $(X_0, 0, 0, 0, V_Y, 0)$, where V_Y is evenly spaced over some interval. The extrema of this latter interval are chosen such that it contains a strict maximum of the modified FLI. We then restrict this interval around the maximum and repeat the computation of the FLI for the new grid and for a longer time. The procedure is iterated until we achieve a sufficiently long integration time.

In Fig. 2.5 we show the results of the method for a time-span of 1000 years, and for values of α equal to $3 \times 10^{-2}, 10^{-3}, 10^{-4}$ AU, correspondingly to $\tilde{d}$ equal to $10^{-3}, 7 \times 10^{-5}, 10^{-5}$ AU. We note that such orbits are slowly drifting along the Y axis (the drift speed is about $2 \times 10^{-6}, 5 \times 10^{-8}$ and 4.5×10^{-9} AU/year for $\alpha = 3 \times 10^{-2}, 10^{-3}, 10^{-4}$ AU respectively): these drifts can be reduced by further refining the interval of the initial data.

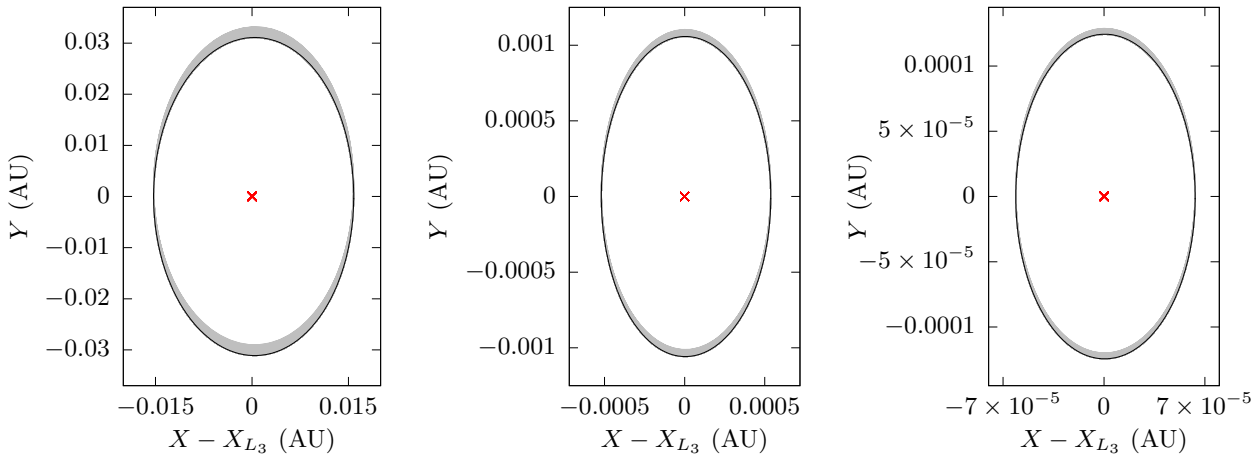

Figure 2.5: Representation of the libration orbits $\ell(\alpha)$ (gray curves) found in the ER3BP with $\alpha = 3 \times 10^{-2}, 10^{-3}, 10^{-4}$ AU for a time-span of 1000 years. The amplitude of the neighbourhood $\mathcal{B}$ is $\tilde{d} = 10^{-3}, 7 \times 10^{-5}, 10^{-5}$ AU for the three different cases. The black curves denote the restriction of $\ell(\alpha)$ to 1 year, while the red points indicate the location of the Sun–Earth L_3 point. Credit: E. Scantamburlo and M. Guzzo, A&A, 638, A137, 2020, reproduced with permission ©ESO.

2.3.4 Computation of the librations in the realistic model

To study the spacecraft dynamics in a model whose ephemerides are comparable with those provided by the JPL digital service, we consider the spacecraft equations of motion (2.53), which include all

the planets from Venus to Neptune[3].

To illustrate how to find libration orbits in such a realistic model, we apply the FLI method and we consider $\ell(3\times10^{-2}$ AU) and $\ell(10^{-3}$ AU) as target orbits and take $\mathcal{B}$ as a neighbourhood of $\ell(3\times10^{-2}$ AU) and $\ell(10^{-3}$ AU) of amplitude $\tilde{d}$ equal to 10^{-3} and 2×10^{-4} AU, respectively. The computation of the modified FLI is stopped once we have restricted the set of initial data such that the interval along the V_Y is smaller than 5×10^{-9} AU day^{-1} and once we achieve an integration time of centuries (in the cases of the librations with amplitude of 3×10^{-2} and 10^{-3} AU the time-spans for the modified FLI computation are 1000 and 400 years respectively). When we conclude this iterative method, we obtain the modified FLI profile, in which the maximum is sharply identified by the initial datum $(X_0,0,0,0,V_Y^*,0)$. For example, the modified FLI profile for the research of the libration with amplitude 3×10^{-2} AU is represented in Fig. 2.6. The trajectory associated to the initial datum with the maximum mFLI value (blue point in Fig. 2.6) represents the orbits that remains the closest to the target one. Moreover, this trajectory (see the first two panels in Fig. 2.7) is librating around L_3 with an amplitude of 3×10^{-2} AU. To appreciate the precision of the method, we also considered the orbits associated to another two initial data with values of the modified FLI that are different from the maximum (the magenta and brown points in Fig. 2.6). Such orbits, shown in Fig. 2.8, are not librations around L_3, even if the variation of the initial velocity $V_Y-V_Y^*$ is very small (about 3×10^{-12} and -3×10^{-11} AU day^{-1}, respectively). Now, we focus our attention on the orbits associated to the maximum value of mFLI for both the case of $\ell(3\times10^{-2}$ AU) and $\ell(10^{-3}$ AU) as target orbits. These trajectories are shown in Fig. 2.7 in the time-span of 650 and 200 years respectively. In the same figure we also show the representations of such trajectories restricted to a time-span of 20 years (black curves) which highlight the drift along the Y axis (about 4×10^{-6} AU yr^{-1}) caused by the planetary perturbations. The relative drift is greater for the libration with amplitude 10^{-3} AU and is smaller for the orbit with greater amplitude. Hence, the orbit with the greater amplitude remains closer to its target orbit. Moreover, the value $\tilde{d}$ for the orbit with smaller amplitude is close to the amplitude of the oscillation introduced by the planetary perturbations (last panel in Fig. 2.2): this implied that values of $\tilde{d}<2d$ are too small and for such a choice of $\tilde{d}$, the FLI method does not converge to a libration orbit around L_3. Therefore, to find oscillations around L_3 with amplitude smaller than $2d$ it is necessary to apply the FLI method by using a sphere in (X,Y,Z) centered at L_3 with radius $\tilde{d}\leq2d$ as $\mathcal{B}$. We note also that the application of the modified FLI method with a one-dimensional grid of initial data is not sufficient, for the research of librations because of the degrees of freedom of the problem: we have to use a two-dimensional grid of initial data $(X,0,0,0,V_Y,0)$ centered at L_3. Therefore, we applied this method with $\tilde{d}=10^{-3}$ and $\tilde{d}=2\times10^{-4}$ AU and found (see e.g., Fig. 2.9) that the bigger values of the mFLI lie on a line not parallel to the X and V_Y axis. This complicates the procedure of refining the initial data, which is summarized in the caption of the figure. Finally, Fig. 2.10 shows the librations obtained using the two-dimensional grid with $\tilde{d}=10^{-3}$ and $\tilde{d}=2\times10^{-4}$ AU: the time-spans of these two orbits are 700 and 250 years respectively. Hence, the FLI method allows us to find libration orbits of the realistic models with amplitudes bigger than d (up to 0.03 AU) for time-spans of centuries.

[3]The initial conditions of the celestial bodies are provided by the JPL digital ephemerides, with P_3 identified with the Earth–Moon barycenter.

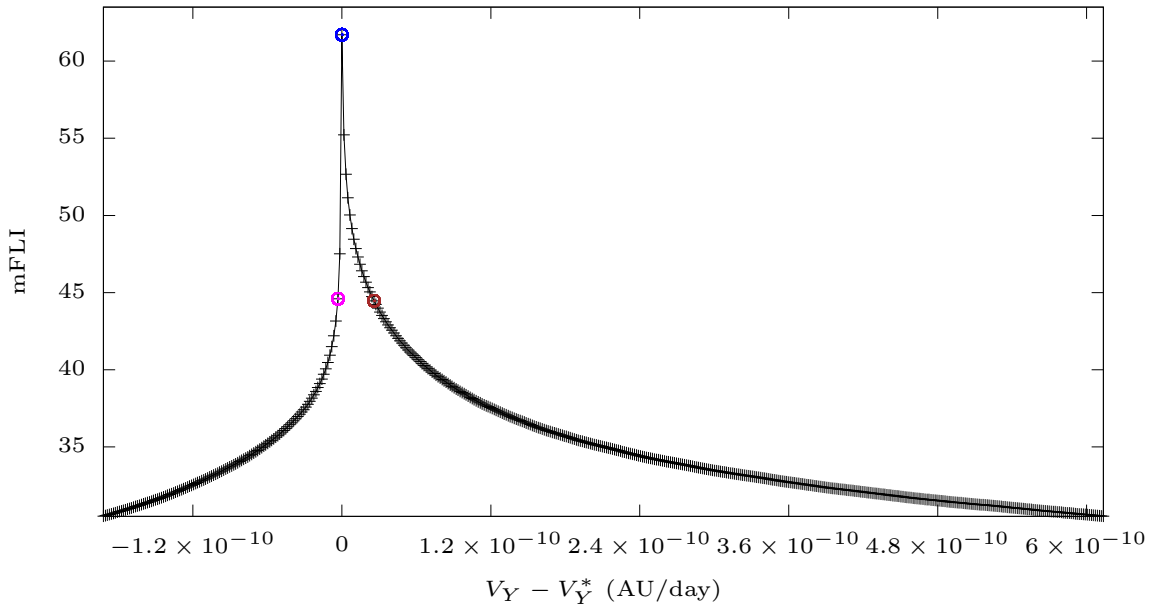

Figure 2.6: mFLI profile computed for 1000 years for the research of the libration of amplitude 3×10^{-2} AU. The blue point denotes the location of V_Y^*, i.e. the velocity component characterized by the maximum value of mFLI. The trajectory with initial datum $(X_0, 0, 0, 0, V_Y^*, 0)$ is shown in the first two panels of Fig. 2.7. We display also the location of another two initial conditions (the magenta and brown points) having a different value of the mFLI; their trajectories are shown in Fig. 2.8. Credit: E. Scantamburlo and M. Guzzo, A&A, 638, A137, 2020, reproduced with permission ©ESO.

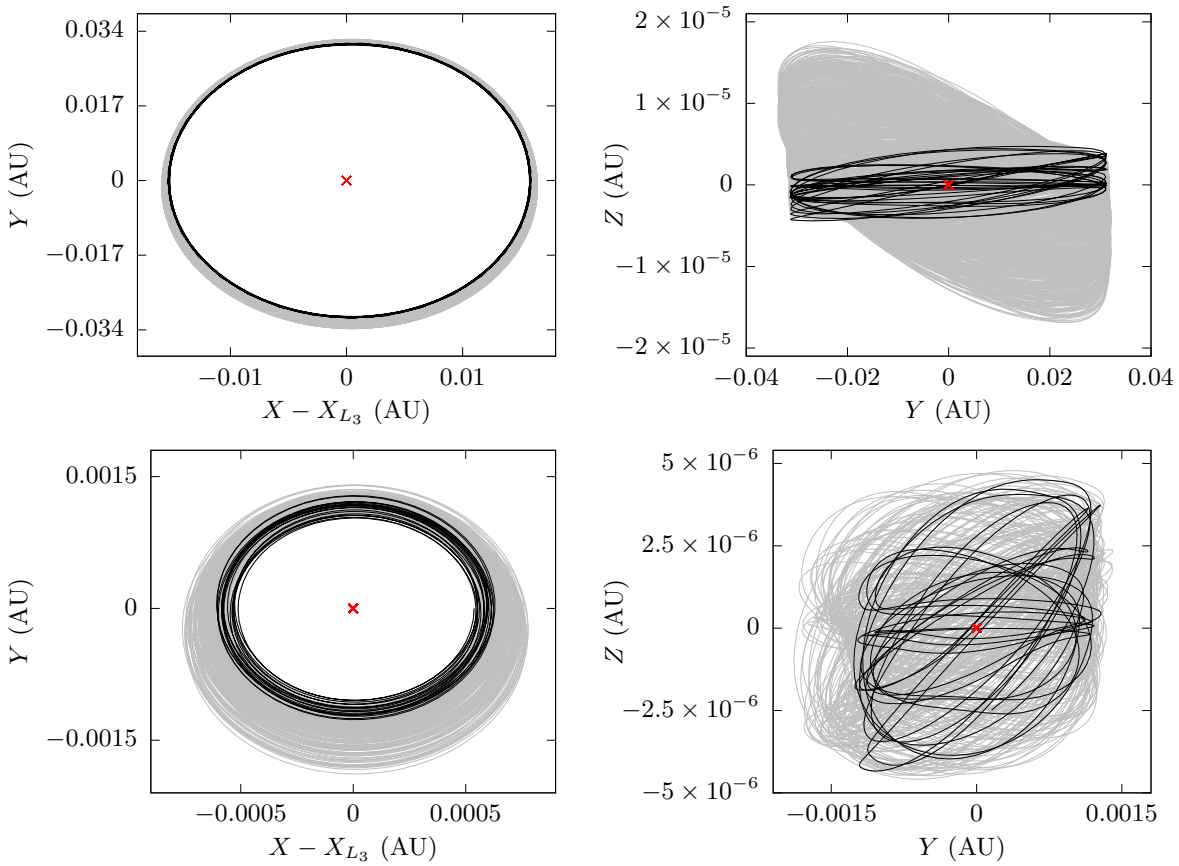

Figure 2.7: Libration orbits found in the realistic model obtained by using $\ell(3 \times 10^{-2}$ AU) and $\ell(10^{-3}$ AU) as target orbits; the time spans are 650 and 200 years respectively. The black lines represent the restriction of the two librations to 20 years. The red point denotes the location of L_3. Credit: E. Scantamburlo and M. Guzzo, A&A, 638, A137, 2020, reproduced with permission ©ESO.

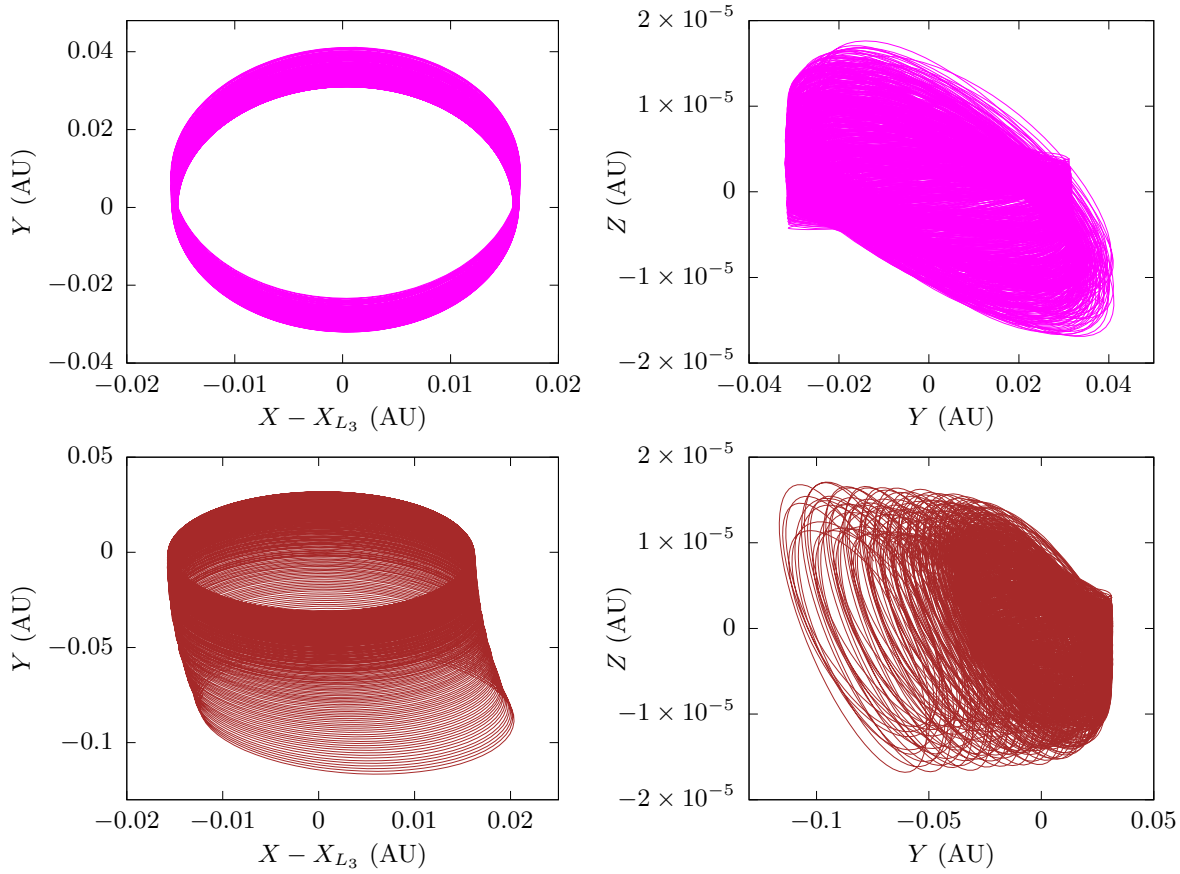

Figure 2.8: Trajectories associated to the magenta and brown point in Fig. 2.6. The integration time is 650 years for both orbits. Credit: E. Scantamburlo and M. Guzzo, A&A, 638, A137, 2020, reproduced with permission ©ESO.

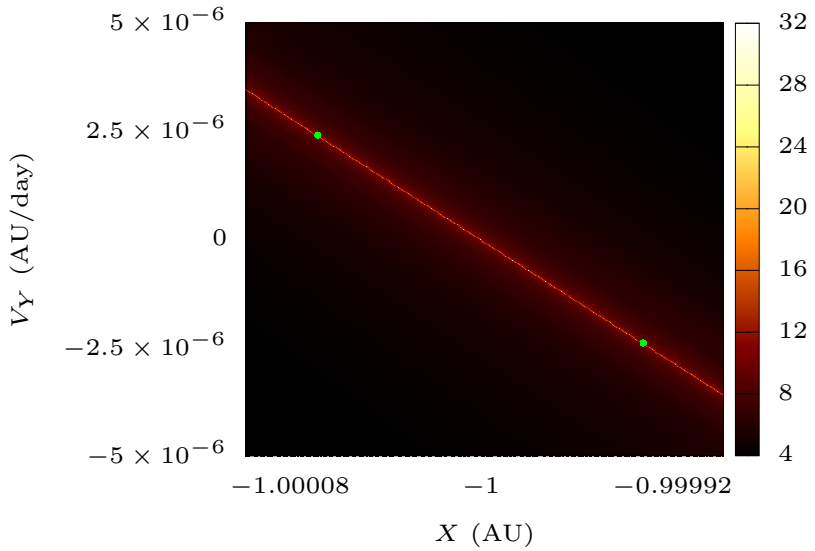

Figure 2.9: Representation of the mFLI map associated to the bidimensional grid of initial data in the case in which L_3 is the reference point and $\tilde{d} = 10^{-3}$ AU; the colors indicate the value of the chaos indicator computed in the time-span of 1000 years. We note that the maximum values of mFLI are not in a line parallel to the X or V_Y axis. For this reason, if we want to have a good refinement of the two-dimensional grid, we need to isolate two points $P_0 = (X_0, V_{Y,0})$, $P_1 = (X_1, V_{Y,1})$ (green points) of the two-dimensional grid characterized by a high value of the modified FLI and then take points X and V_Y such that $X = X_0 + \delta(X_1 - X_0) + \epsilon(V_{Y,1} - V_{Y,0})$, $V_Y = V_{Y,0} + \delta(V_{Y,1} - V_{Y,0}) - \epsilon(X_1 - X_0)$ with $\delta \in [0, 1]$ and $\epsilon \in [-\Delta\epsilon, \Delta\epsilon]$: we used $\Delta\epsilon$ equal to 2×10^{-5} for the refinement of the grid shown in this figure. Credit: E. Scantamburlo and M. Guzzo, A&A, 638, A137, 2020, reproduced with permission ©ESO.

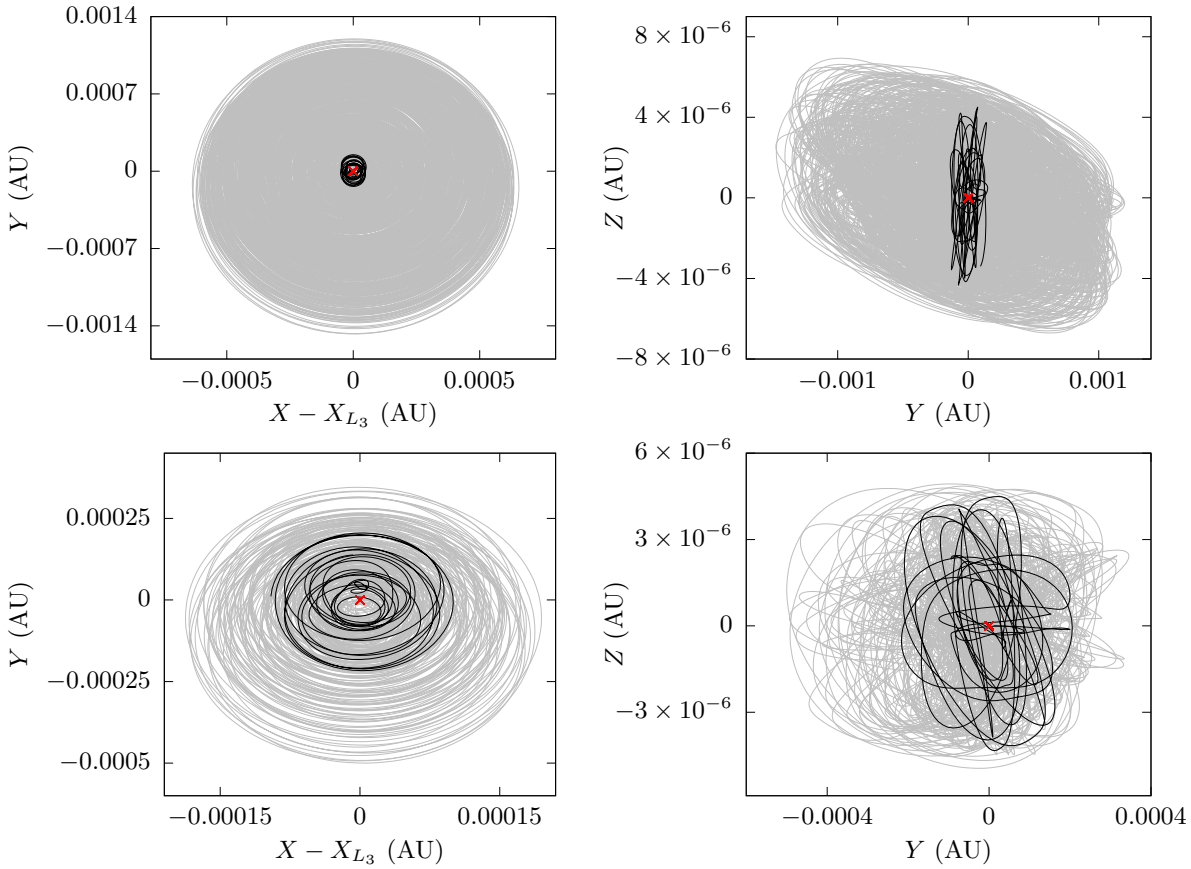

Figure 2.10: Representation of the librations in the realistic model obtained assuming a neighbourhood of L_3 with amplitude $\tilde{d}$ equal to 10^{-3} and 2×10^{-4} AU respectively. The time-span of the two orbits are 700 and 250 years respectively. The black line represent the restriction of the trajectories to 20 years. The red point indicated the position of the Sun–Earth L_3 point in the rotating-pulsating reference frame. Credit: E. Scantamburlo and M. Guzzo, A&A, 638, A137, 2020, reproduced with permission ©ESO.

2.4 Conclusions

Since close to the Sun–Earth Lagrangian point L_3 the planetary perturbations (mainly from Jupiter and Venus) are stronger than Earth's attraction, it is not evident that the dynamics close to L_3 defined within the circular restricted three-body problem can be continued to a realistic model of the Solar System. We analyze in particular the effects of the planetary perturbations and of the eccentricity of the Earth. The planetary perturbations provide oscillations of about 15 000 km, while the effect of the eccentricity of the Earth, apart from a small oscillation, is absorbed by considering a rotating-pulsating frame. Using a combination of the Hamiltonian averaging method with the FLI method we find orbits that remain close to L_3 for at least 200 years in a model of the Solar System whose dynamics are compatible with JPL digital ephemerides, with libration amplitudes ranging from 2.5×10^{-4} to 3×10^{-2} AU.

Chapter 3

Interplanetary transfers using stable and unstable manifold tubes originating at L_1 and L_2 in the elliptic restricted three-body problems

3.1 Introduction

In the last decades, the solutions originating at the Lagrangian points L_1 and L_2 of the circular restricted three-body problem (CR3BP) have been widely analyzed in connection to transport phenomena, close encounters of comets and asteroids as well as low-energy transfer orbits (for example, see Celletti and Giorgilli, 1990; Celletti and Froeschlé, 1998; Jorba and Masdemont, 1999; Palacián and Yanguas, 2004; Ren et al., 2012; Guzzo and Lega, 2013, 2015; Celletti et al., 2015; Guzzo and Lega, 2017, 2018; Paez and Guzzo, 2020; Ceccaroni et al., 2016; Pucacco, 2019 and Simó, 1999; Gómez et al., 2000, 2004; Topputo et al., 2005; Koon et al., 2008; Zanzottera et al., 2012; Pergola et al., 2009; Belbruno et al., 2010; Topputo et al., 2005; Parker and Anderson, 2013; Farquhar et al., 2004; Howell et al., 2006; Howell and Kakoi, 2006; Pergola et al., 2009; Belbruno et al., 2010; Zanzottera et al., 2012; Parker and Anderson, 2013). As a matter of fact several space missions (such as ISEE-3, Wind, SOHO, WMAP, Genesis, Herschel and Planck) were designed by exploiting the Sun–Earth Lagrangian points L_1 and L_2, and other planned future missions will reach the vicinity of such Lagrangian points. The use of the Lagrangian solutions for Solar System applications requires to consider hierarchical extension of the model (see for example Barrabés et al., 2016; Jorba and Nicolás, 2020; Jorba et al., 2020; Scantamburlo and Guzzo, 2020; Kumar et al., 2021; Gawlik et al., 2009). In fact, we consider the Sun–Mercury or the Sun–Mars systems, the CR3BP provides only a crude approximation of the dynamics; as a matter of fact the eccentricities of the two planets are currently about 0.2 and 0.09; for this reason, if we plan to apply the space manifold dynamics between the Sun–Earth to the Sun–Mercury or Sun–Mars Lagrangian points, a deep analysis of the solutions originating at L_1 and L_2 in the elliptic restricted three-body problem (ER3BP) is required. For example, in connection to space flight dynamics the ER3BP has been studied to design transfers between halo orbits of a Lagrangian point (Hiday-Johnston and Howell, 1994; Howell and Hiday-Johnston, 1994), gravity-assist (de Almeida Prado, 1997; de Almeida Prado

and Neto, 2006; Qi and de Ruiter, 2018; Ferreira et al., 2017) and ballistic captures (Hyeraci and Topputo, 2010). When we consider a generalization of space manifold dynamics to the ER3BP several difficulties appear which on the one hand are of substantial nature (such as the lack of a constant of motion generalizing the Jacobi integral), on the other hand are of technical nature (the development of perturbation theories is complicated by the implementation of a partially hyperbolic Floquet theory). In Paez and Guzzo (2021) a generalization of the space manifold dynamics to the solutions originating at L_1, L_2 of the ER3BP was done through the construction of Hamiltonian Floquet-Birkhoff normal forms.

The aim of the paper is to analyze the differences of the manifold tubes originating at the Lagrangian solutions in the planar ER3BP and the CR3BP, and to discuss the impact they have in the design of interplanetary transfers. Using the definition and the computation of the manifold tubes provided in Paez and Guzzo (2021), we first characterize the evolution of the orbital elements of a spacecraft whose motion is described by a solution of the ER3BP that belong to the manifold tubes of a generic Sun–P_j system. Specifically, we consider any solution whose initial condition belongs to the local unstable manifold tube originating at L_1 or L_2. For an initial time-span the solution remains close to the Lagrangian one, oscillating around it. Then, the spacecraft exits from the planet's Hill sphere and we follow its evolution until it arrives sufficiently far from the planet so that its dynamics is well approximated by the Sun–spacecraft two-body problem. After that moment, the solution is well approximated by a Keplerian one up to an eventual additional close encounter with P_j, and therefore the semi-major axis, eccentricity and longitude of perihelion of the spacecraft remain approximately constant. The solutions whose initial condition belong to the local stable manifold tube are characterized by the same behaviour with reference to negative time-spans. We denote by $\mathcal{K}^s_{j,L_i}$ and $\mathcal{K}^u_{j,L_i}$ the family of all these Keplerian orbits which are obtained for all the possible initial conditions in the local stable or unstable manifold tubes originating at L_i of the Sun–P_j ER3BP, and for all the values of initial true anomaly of the planet. The idea is to exploit the orbits in the sets $\mathcal{K}^{s/u}_{h,L_i}$ and $\mathcal{K}^{s/u}_{k,L_m}$ for the design of an interplanetary transfer between the two planets P_h and P_k.

With evidence, the construction of the families $\mathcal{K}^{s/u}_{j,L_i}$ can be defined using the simpler CR3BP, and one may argue if indeed the more complicated ER3BP is worthy to be considered. Here we find the main differences between the two models: depending on the value of the eccentricity e_j of the orbit of planet P_j, we find a big difference in the distribution of the orbital parameters of the Keplerian orbits in the sets $\mathcal{K}^{s/u}_{j,L_i}$ when computed using the ER3BP rather than the CR3BP. Precisely, we find that for:

$$e_j \gtrsim \frac{3r_{\text{Hill}}}{a_j}, \tag{3.1}$$

where a_j, e_j denote the semi-major axis and eccentricity of the planet P_j and r_{Hill} the Hill radius, the distribution of the longitudes of perihelion of the orbits in the above families is bounded; conversely, for $e_j \lesssim (3r_{\text{Hill}}/a_j)$ the distribution is spread in $[0, 2\pi]$ (the latter case, for $e_j = 0$, corresponds to the CR3BP). From a space flight dynamics point of view, this implies that:

- if both the eccentricities of the planets P_h and P_k are large (i.e. inequality (3.1) is satisfied for P_h, P_k), then the distribution of longitudes of the perihelion for the orbits in the families $\mathcal{K}^{s/u}_{h,L_i}$ and $\mathcal{K}^{s/u}_{k,L_m}$ of each planet is bounded in some intervals, and if such intervals do not match it is not possible to perform an Hohmann transfer[1] between P_h and P_k via the families

[1]Since we find that all the orbits in the families have eccentricity different from 0 (see Sections 3.2 and 3.3

$\mathcal{K}^{s/u}_{h,L_i}, \mathcal{K}^{s/u}_{k,L_m}$; in such a case, other types of transfers may be considered, in the context of the ER3BP.

- if both the eccentricities of the planets P_h and P_k are small (i.e. inequality (3.1) is not satisfied for P_h, P_k), then the distribution of longitudes of the perihelion for the orbits in the families $\mathcal{K}^{s}_{h,L_i}, \mathcal{K}^{s}_{k,L_m}$ of each planet is distributed in $[0, 2\pi]$, and we have an abundance of co-axial orbits in the families which are suitable for an Hohmann transfer. This is the situation where the CR3BP is a suitable model for the transfer.

- the most interesting situation arises when one planet satisfies the inequality (3.1), while the other does not. In such a case the longitudes of perihelion of the orbits in the families $\mathcal{K}^{s/u}_{h,L_i}$ of the latter planet spread in $[0, 2\pi]$, and therefore we still find an abundance of co-axial orbits suitable for the Hohmann transfer. Nevertheless, since the longitudes of perihelion of the orbits in the families $\mathcal{K}^{s/u}_{k,L_m}$ of the former planet are in a bounded interval, it is necessary to properly synchronize the maneuvers of the transfer in suitable time windows. This is the situation where the ER3BP must be considered for the transfer.

We apply these results to the Sun–Mercury, Sun–Earth and Sun–Mars systems: since both Mercury and Mars satisfy inequality (3.1), while the Earth (as well as Venus) does not fulfill such condition, the distribution of the longitudes of perihelion is bounded in the Mercury and Mars systems, and is spread in $[0, 2\pi]$ in the Earth system. This implies that it is possible to determine an Hohmann transfer between the manifold tubes originating at a Lagrangian points of the Sun–Earth and Sun–Mercury, or Sun–Mars ER3BP. Then, we calculate the transfer between the Sun–Earth L_1 and the Sun–Mercury L_2, and between the Sun–Earth L_2 and the Sun–Mars L_1 points using the decoupled ER3BPs[2]. Finally we check that the transfers, whose initial conditions are analytically computed using two decoupled ER3BPs, remain effective also in the bi-elliptic four body problem (BE4BP), namely a model in which a spacecraft is gravitationally attracted by the Sun and the two planets that are performing an elliptic motion around the Sun, for the whole considered time interval.

The paper is organized as follow: in Sec. 3.2 we first define the planar BER4BP, and then we briefly summarize the procedure used in Paez and Guzzo (2021) for the computation of the solutions originating at the Lagrangian points L_1 and L_2 in the ER3BP. Then we analyze the orbital elements evolution of the manifold tubes. Finally, in Sec. 3.3 we apply the results found to an interplanetary transfer between the Earth and Mercury, and the Earth and Mars systems using both the decoupled ER3BPs and the BER4BP.

for details, and also Fig. 3.7), here we need to refer to the extended definition of Hohmann transfers between co-axial elliptic orbits (see, for example, Curtis, 2005). Precisely a transfer between two different co-axial elliptic orbits is obtained with two impulsive maneuvers: the first maneuver is obtained by applying a tangential Δv at a pericenter/apocenter of the first orbit; the spacecraft is thus injected into the transfer orbit and when it arrives to the next pericenter/apocenter it is injected into the final Keplerian orbit with an additional tangential Δv.

[2]We do not compute transfers between the Sun–Earth and Sun–Venus Lagrangian points since both planets do not satisfy inequality (3.1), and therefore the transfers are suitably described with the CR3BP.

3.2 Study of the spacecraft orbital elements around L_1 and L_2 in the elliptic restricted three-body problem

3.2.1 The planar bi-elliptic restricted four-body problem

To model the transfer of a spacecraft between the manifold tubes of the planets P_h, P_k we first simplify the equations of motion in the full Solar System to the planar bi-elliptic restricted four-body problem (BER4BP). Denoting by $\boldsymbol{r}_j$ and $\boldsymbol{r}$ the position vectors of the j-th planet and of the spacecraft in a heliocentric reference frame $Oxyz$, by μ and ε_j the gravitational parameters of the Sun and of the j-th planet, and by $(a_j, e_j, \varpi_j, f_j)$ the orbital elements of planet P_j, the equations of motion of the spacecraft are

$$\ddot{\boldsymbol{r}} = -\mu \frac{\boldsymbol{r}}{\|\boldsymbol{r}\|^3} - \sum_{j=h,k} \varepsilon_j \left(\frac{\boldsymbol{r}_j}{\|\boldsymbol{r}_j\|^3} + \frac{\boldsymbol{r} - \boldsymbol{r}_j}{\|\boldsymbol{r} - \boldsymbol{r}_j\|^3} \right). \tag{3.2}$$

Then, we compare the dynamics of the BER4BP with that of the two decoupled Sun–P_h and Sun–P_k elliptic restricted three-body problems (ER3BPs). For this reason, for each planet we introduce the Sun–planet heliocentric rotating-pulsating reference frame OXY which is centered at the Sun, and whose axes are parallel to the unit vectors

$$\boldsymbol{u}_{r,j} = \frac{\boldsymbol{r}_j}{\|\boldsymbol{r}_j\|}, \quad \boldsymbol{u}_{t,j} = \frac{\boldsymbol{r}_j \times \boldsymbol{u}_{n,j}}{\|\boldsymbol{r}_j \times \boldsymbol{u}_{n,j}\|}, \tag{3.3}$$

where $\boldsymbol{u}_{n,j} = \frac{\dot{\boldsymbol{r}}_j \times \boldsymbol{r}_j}{\|\dot{\boldsymbol{r}}_j \times \boldsymbol{r}_j\|}$ and $j = h, k$; in such a reference frame, the planet P_j is located on the X axis.

We investigate the dynamics close to the Lagrangian solutions of the Sun–P_j ER3BP using the Floquet-Birkhoff normal forms defined in Paez and Guzzo (2021).

3.2.2 The Floquet-Birkhoff normal form in the elliptic restricted three-body problem

It is usual to describe the planar ER3BP using a rotating-pulsating reference frame and standard Sun–planet units of measure (so that the sum of Sun and planet gravitational parameters is one, the semi-major axis of the planet orbit is one, and the revolution period of the planet is 2π). The Hamilton function of the ER3BP in the heliocentric rotating-pulsating reference frame is:

$$\begin{aligned}\mathcal{H}(X, Y, P_X, P_Y, f_j; \varepsilon_j, e_j) =& \frac{1}{2}\left[(P_X + Y)^2 + (P_Y - X)^2\right] - \frac{1}{1 + e_j \cos(f_j)} \left[\frac{1}{2}(X^2 + Y^2) + \frac{1}{\sqrt{X^2 + Y^2}}\right] \\ &+ \frac{\varepsilon_j}{1 + e_j \cos(f_j)} \left(X + \frac{1}{\sqrt{X^2 + Y^2}} - \frac{1}{\sqrt{(X-1)^2 + Y^2}} \right)\end{aligned} \tag{3.4}$$

where ε_j denotes the gravitational parameter of the planet, and P_X and P_Y represent the conjugate momenta to X and Y respectively. We remark that the Hamiltonian is not autonomous since it depends explicitly on the planet true anomaly f_j, which is also the independent variable of

Hamilton's equations:

$$\frac{dX}{df_j} = \frac{\partial \mathcal{H}}{\partial P_X}, \quad \frac{dY}{df_j} = \frac{\partial \mathcal{H}}{\partial P_Y}, \quad \frac{dP_X}{df_j} = -\frac{\partial \mathcal{H}}{\partial X}, \quad \frac{dP_Y}{df_j} = -\frac{\partial \mathcal{H}}{\partial Y}. \tag{3.5}$$

The advantage of the rotating-pulsating reference frame formulation is that the Hamiltonian system (3.5) has five equilibrium points $L_1, \ldots, L_5$ in the same location of the Lagrangian points computed in the Sun–planet CR3BP. We focus our attention on the two collinear equilibria L_1 and L_2 (located at $(X, Y, P_X, P_Y) = (X_{L_i}, 0, 0, X_{L_i})$, $i = 1, 2$). Following Paez and Guzzo (2021) we construct the manifold tubes originating at L_1, L_2 of the ER3BP using a suitable Floquet-Birkhoff normal form. We here summarize the construction of such normal forms.

Let us first rewrite the Hamiltonian (3.4) using the translated Cartesian variables:

$$q_1 := X - X_{L_i}, \quad q_2 := Y, \quad p_1 := P_X, \quad p_2 := P_Y - X_{L_i} \tag{3.6}$$

and then we expand it in Taylor series at the origin:

$$H(\boldsymbol{q}, \boldsymbol{p}; f_j) := \sum_{\alpha=2}^{\infty} H_\alpha(\boldsymbol{q}, \boldsymbol{p}; f_j) \tag{3.7}$$

where $H_\alpha(\boldsymbol{q}, \boldsymbol{p}; f_j)$ is a polynomial of degree α in $(\boldsymbol{q}, \boldsymbol{p})$. In the paper Paez and Guzzo (2021), a canonical transformation:

$$(\boldsymbol{q}, \boldsymbol{p}; f_j) = \mathcal{C}(\boldsymbol{Q}, \boldsymbol{P}; f_j) \tag{3.8}$$

has been constructed conjugating the Hamiltonian (3.7) to:

$$K(\boldsymbol{Q}, \boldsymbol{P}; f_j) = \sum_{\nu=1}^{N/2} K_{2\nu}(\boldsymbol{Q}, \boldsymbol{P}) + R_{N+1}(\boldsymbol{Q}, \boldsymbol{P}; f_j) \tag{3.9}$$

where $K_{2\nu}(\boldsymbol{Q}, \boldsymbol{P})$ denotes an autonomous polynomial of degree 2ν depending on $(\boldsymbol{Q}, \boldsymbol{P})$ only through the combinations of the terms $\frac{Q_1^2+P_1^2}{2}$ and Q_2P_2; the remainder $R_{N+1}(\boldsymbol{Q}, \boldsymbol{P}; f_j)$ is a polynomial of order $N+1$, possibly dependent on f_j; N is such that the frequencies of the problem do not satisfy resonances of order smaller than N (see the paper Paez and Guzzo, 2021, for details). Since the transformation $\mathcal{C}(\boldsymbol{Q}, \boldsymbol{P}; f_j)$ is obtained from the composition of a Floquet transformation and $N-2$ Birkhoff transformations, the Hamiltonian (3.9) has been called Floquet-Birkhoff normal form.

A classification of the orbits in a neighborhood of the equilibrium L_i is provided by the flow of the integrable Hamiltonian:

$$\mathcal{K}(\boldsymbol{Q}, \boldsymbol{P}) := \sum_{\nu=1}^{N/2} K_{2\nu}(\boldsymbol{Q}, \boldsymbol{P}), \tag{3.10}$$

which is obtained from (3.9) by neglecting the remainder $R_{N+1}(\boldsymbol{Q}, \boldsymbol{P}; f_j)$. We emphasize that when the variables (Q_1, P_1) represent the elliptic motion, while (Q_2, P_2) the hyperbolic one, the lowest order approximation of $\mathcal{K}$ is

$$K_2(\boldsymbol{Q}, \boldsymbol{P}) = \sigma \frac{Q_1^2 + P_1^2}{2} + \lambda Q_2 P_2 \qquad \sigma, \lambda > 0. \tag{3.11}$$

The flow of the approximated normal form (3.11) has a family of periodic orbits, the planar Lyapunov orbits identified by $Q_2, P_2 = 0$ and $(Q_1, P_1) = \sqrt{2I_1}(\sin\phi_1, \cos\phi_1)$, with $\phi_1 \in [0, 2\pi]$ and $I_1 > 0$ suitably small. These Lyapunov orbits have local stable manifold identified by $(Q_1, P_1) = \sqrt{2I_1}(\sin\phi_1, \cos\phi_1)$, $P_2 \neq 0$ suitably small and $Q_2 = 0$, while the local unstable manifold is identified by $(Q_1, P_1) = \sqrt{2I_1}(\sin\phi_1, \cos\phi_1)$, $Q_2 \neq 0$ suitably small and $P_2 = 0$.

When we map back these sets to the Cartesian rotating-pulsating reference frame with the canonical transformation

$$(X, Y, P_X, P_Y; f_j) = (X_{L_i}, 0, 0, X_{L_i}; 0) + \mathcal{C}(\boldsymbol{Q}, \boldsymbol{P}; f_j)$$

we obtain:

- the planar Lyapunov tori:

$$\begin{aligned}\mathcal{T}_{I_1} = \bigcup_{f_j, \phi_1 \in [0,2\pi]} \{(X, Y, P_X, P_Y; f_j) = (X_{L_i}, 0, 0, X_{L_i}; 0) + \mathcal{C}(\boldsymbol{Q}, \boldsymbol{P}; f_j) : \\ (Q_1, P_1) = \sqrt{2I_1}(\sin\phi_1, \cos\phi_1), Q_2, P_2 = 0\};\end{aligned} \tag{3.12}$$

- the local unstable tubes of $\mathcal{T}_{I_1}$:

$$\begin{aligned}\mathcal{W}^{u_{loc}}_{I_1} = \bigcup_{f_j, \phi_1 \in [0,2\pi]} \{(X, Y, P_X, P_Y; f_j) = (X_{L_i}, 0, 0, X_{L_i}; 0) + \mathcal{C}(\boldsymbol{Q}, \boldsymbol{P}; f_j) : \\ (Q_1, P_1) = \sqrt{2I_1}(\sin\phi_1, \cos\phi_1), |Q_2| \in (0, \epsilon), P_2 = 0\},\end{aligned} \tag{3.13}$$

  where ϵ is such that $(\boldsymbol{Q}, \boldsymbol{P})$ is in the domain of the transformation $\mathcal{C}(\boldsymbol{Q}, \boldsymbol{P}; f_j)$;

- the local stable tubes of $\mathcal{T}_{I_1}$:

$$\begin{aligned}\mathcal{W}^{s_{loc}}_{I_1} = \bigcup_{f_j, \phi_1 \in [0,2\pi]} \{(X, Y, P_X, P_Y; f_j) = (X_{L_i}, 0, 0, X_{L_i}; 0) + \mathcal{C}(\boldsymbol{Q}, \boldsymbol{P}; f_j) : \\ (Q_1, P_1) = \sqrt{2I_1}(\sin\phi_1, \cos\phi_1), |P_2| \in (0, \epsilon), Q_2 = 0\},\end{aligned} \tag{3.14}$$

  where ϵ is such that $(\boldsymbol{Q}, \boldsymbol{P})$ is in the domain of the transformation $\mathcal{C}(\boldsymbol{Q}, \boldsymbol{P}; f_j)$.

Then, we define the global stable and unstable manifolds $\mathcal{W}^s_{I_1}$, $\mathcal{W}^u_{I_1}$ of the planar Lyapunov tori by propagating the initial conditions in the sets $\mathcal{W}^{s_{loc}}_{I_1}$, $\mathcal{W}^{u_{loc}}_{I_1}$ with the flow of the ER3BP.

Remark. We remark that the Lyapunov torus is indeed invariant, and the solutions in $\mathcal{W}^s_{I_1}$, $\mathcal{W}^u_{I_1}$ converge (in the future or in the past) to it only in the approximation which is obtained by neglecting the remainder of the Floquet-Birkhoff normal form R_{N+1}. The errors introduced by such an approximation are negligible for space flight dynamics, as soon N is suitably large (we will use $N = 6$).

In Fig. 3.1 we show the projection of the manifold tubes originating at L_1 and L_2 in the Sun–Earth and Sun–Mercury ER3BP (first four panels) on the plane OXY; the initial conditions have been chosen in the local stable and unstable manifolds W^s_{loc}, W^u_{loc} with $f_{j0} = 0$, and then are propagated with the flow of the ER3BP till the orbits arrive at the first aphelion (or perihelion respectively) which is sufficiently far from the planet. We note that the manifold tube in the

Sun–Mercury system enlarges when the solution $(X(f_j), Y(f_j))$ is getting away from the planet (panel d)); this behaviour is less evident for the Sun–Earth system (panel c)). This is an effect introduced by the rotating-pulsating reference frame; as a matter of fact the representation of the same manifold tube in the rescaled variables $\frac{1-e_j^2}{1+e_j \cos f}(X(f_j), Y(f_j))$ (panel f)) are not affected by this enlargement, while we appreciate the oscillation due to the motion of the Lagrangian solutions in the non-pulsating reference frame.

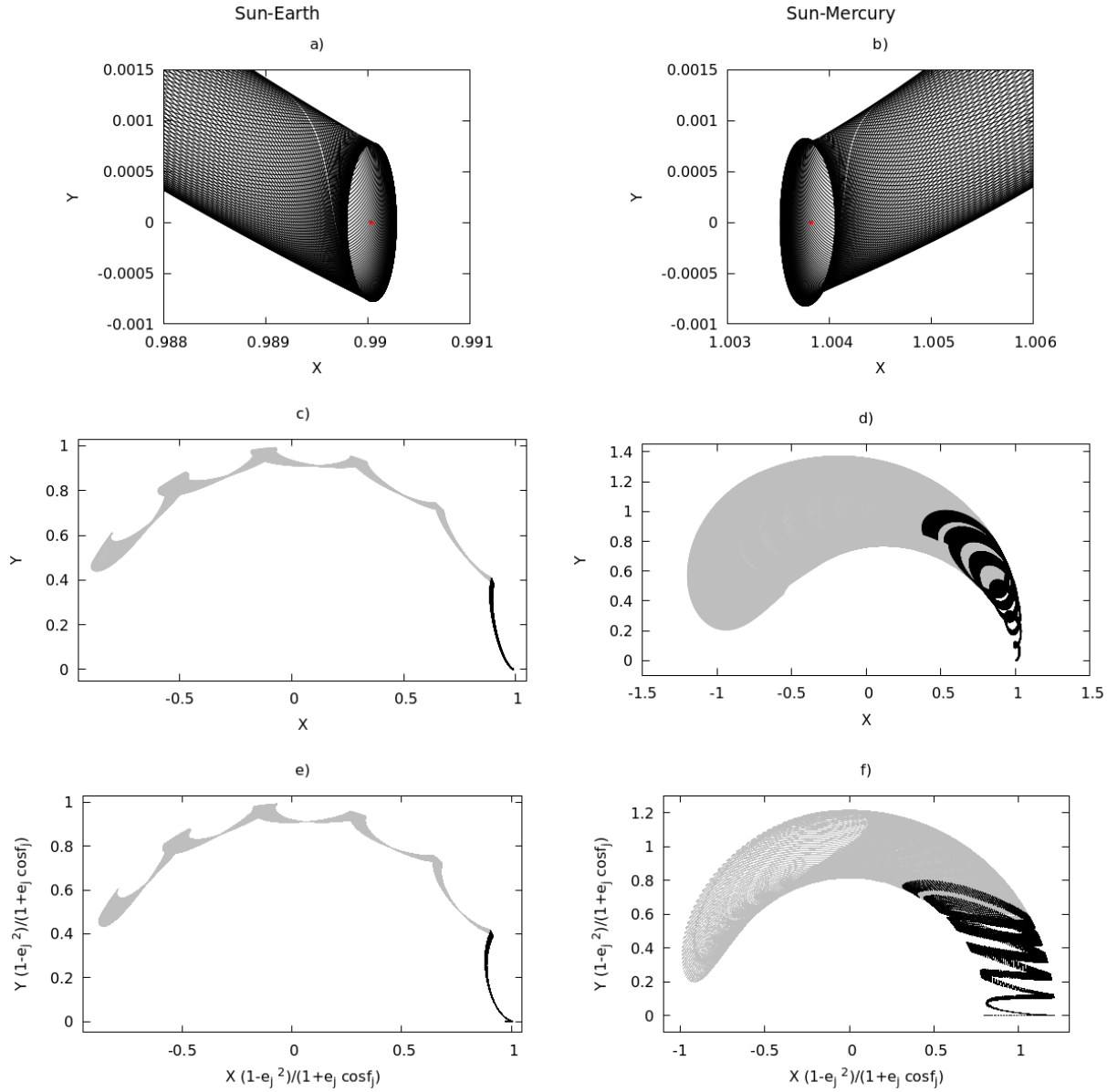

Figure 3.1: Panels a) and c) show the unstable manifold tube originating at the Sun–Earth L_1 for $I_1 = 5 \times 10^{-7}$, $Q_2 = 10^{-6}$, $f_{j0} = 0$ and $\phi_1 \in [0, 2\pi]$, while panels b) and d) panel show the stable manifold tube originating at the Sun–Mercury L_2 for $I_1 = 5 \times 10^{-7}$, $P_2 = 10^{-6}$, $f_{j0} = 0$ and $\phi_1 \in [0, 2\pi]$. The black dots belong to the orbits in the manifold tubes up to the stopping points (aphelion for the Sun–Earth system, perihelion for the Sun–Mercury system), while the gray dots belong to the same orbits, but for a later time. The red points indicate the location of the Lagrangian point. Panels e) and f) display the same manifolds using the rescaled coordinates associated to the Sun–Earth and Sun–Mercury systems respectively (the reference frame is still a rotating, but not pulsating, one).

3.2.3 Orbital element representation of the manifold tubes of the ER3BP in the inertial reference frame

In this subsection we provide evidence that there exists a threshold value for the eccentricity and the gravitational parameter of the planet P_j which changes drastically the distribution of the longitude of perihelion of the orbits in the manifold tubes originating at L_1 and L_2 in the ER3BP. For example, if the Sun–P_h and the Sun–P_k systems fulfill such threshold value, and the distributions of the longitude of perihelion do not match in the two ER3BPs, this implies that a Hohmann transfer can not be used to transfer a spacecraft from the unstable manifold tube originating at a collinear Lagrangian point of P_h to the stable manifold tube originating at a Lagrangian point of P_k. Conversely, Hohmann transfer exists when at least one of the planets has eccentricity below the threshold value.

For this reason we study the representation of the manifold tubes of both Sun–P_h and Sun–P_k ER3BPs using the orbital elements computed in the same heliocentric (non-rotating and non-pulsating) reference frame. The transformation from the rotating-pulsating reference frame of planet P_j to such a heliocentric (non-rotating and non-pulsating) reference frame is denoted by:

$$(x, y, v_x, v_y) = T_j(X, Y, P_X, P_Y; f_j) := T(X, Y, P_X, P_Y; a_j, e_j, f_j, \varpi_j) \tag{3.15}$$

where X, Y, P_X, P_Y represent the canonical coordinates and momenta of the rotating-pulsating reference frame; $v_x := dx/dt$, $v_y := dy/dt$ denote the Cartesian components of the velocity in the heliocentric reference frame; the dependence on the planet P_j is absorbed by a_j, e_j, f_j, ϖ_j.

A family of orbits in the manifold tubes. Let us consider a solution $(X(f_j), Y(f_j), P_X(f_j), P_Y(f_j), f_j)$ with initial condition in $\mathcal{W}^u_{I_1}$, with $(X(f_{j0}), Y(f_{j0}), P_X(f_{j0}), P_Y(f_{j0}), f_{j0})$ close to the torus $\mathcal{T}_{I_1}$ obtained using the Floquet-Birkhoff normal form. We highlight the evolution of the solution in different time intervals:

(i) For an initial interval $\Delta f_1 = [f_0, f_1]$ the solution remains close to the Lagrangian point, and oscillates around it. In this time interval the representation of the solution on the Oxy reference frame using the transformation T_j (see (3.15)) is characterized by orbital elements oscillating close to the orbital elements of the Lagrangian solution.

(ii) In a following interval $\Delta f_2 = [f_1, f_2]$ the solution exits from the Hill sphere of the planet abandoning the local unstable manifold, and arrives to a distance from the planet where the spacecraft-Sun two body problem provides a good approximation of the dynamics. The stopping point f_2 is easily identified since the time evolution of the orbital elements of the spacecraft become almost constant before f_2. Moreover, we choose f_2 to be a perihelion or aphelion (depending on the transfer).

(iii) For a long time interval $\Delta f_3 = [f_2, f_3]$, where the solution does not approach again the Hill sphere of the planet, the orbit of the spacecraft is well approximated by a Keplerian one, with orbital elements determined at f_2. The family $\mathcal{K}^u_{I_1}$ of all these Keplerian orbits, obtained for all the possible initial conditions in the local unstable manifold, can be used for the design of transfers.

The same arguments apply with minor changes to the solutions in the stable manifolds $\mathcal{W}^s_{I_1}$. We

therefore provide a representation of the orbital elements for the Keplerian orbits in the families $\mathcal{K}^u_{I_1}, \mathcal{K}^s_{I_1}$. Depending on the values of the action I_1 and of the phase ϕ_1 which determine the initial conditions on the local manifolds, and on the value of the true anomaly of the planet f_j, we obtain the distribution of the orbital elements of the spacecraft a, e, f, ϖ. We find that for small values of the eccentricity (and therefore including the CR3BP approximation), the longitudes of perihelia in the family spans the full interval $[0, 2\pi]$, thus allowing a simple synchronization of orbital transfers between the manifolds of two planets and a wide choice of orbital maneuvers. The distribution of ϖ in the family becomes a smaller interval for larger values of the eccentricity, thus restricting the possibility of orbital maneuvers and, as a minor consequence, the optimizations of the Δv. The Earth and Venus fulfill the first case, while Mars and Mercury fulfill the second one.

Orbital elements evolution of the Lagrangian solutions. Let us first compute a convenient approximation for the evolution of the orbital elements a, e, f, ϖ of the Lagrangian solutions L_1 and L_2 in the Oxy reference frame, whose orbits is an ellipse described by $\boldsymbol{r}(t) = X_{L_i}\boldsymbol{r}_j(t)$, where $\boldsymbol{r}$ and $\boldsymbol{r}_j$ denote the position vector of the Lagrangian solution and of the planet P_j respectively in the Oxy reference frame (for further details, the reader is referred to Appendix C). By solving $\boldsymbol{r}(t) = X_{L_i}\boldsymbol{r}_j(t)$ for all t, we find immediately

$$f + \varpi = f_j + \varpi_j. \tag{3.16}$$

Moreover, by neglecting the difference in the gravitational parameter of P_j with respect to the gravitational parameter of the Sun, we obtain:

$$a \backsimeq \frac{a_j(e_j^2 - 1)X_{L_i}}{2e_j(X_{L_i}^3 - 1)\cos f_j + (1 + e_j^2)X_{L_i}^3 - 2} \tag{3.17}$$

and, by defining

$$\xi := e\cos f, \quad \eta := e\sin f, \tag{3.18}$$

we get

$$\xi = X_{L_i}^3 - 1 + e_j X_{L_i}^3 \cos f_j, \quad \eta = e_j X_{L_i}^3 \sin f_j; \tag{3.19}$$

i.e. (ξ, η) describes a circumference parameterized by the planet true anomaly f_j, whose radius and center are $e_j X_{L_i}^3$ and $(X_{L_i}^3 - 1, 0)$ respectively; the eccentricity of L_i is provided by $e = \sqrt{\xi^2 + \eta^2}$. We note that the angular momentum h of L_i is constant. To represent the longitude of pericenter of the Lagrangian solutions as a function of f_j we introduce the variables:

$$\tilde{\xi} := e\cos\varpi, \quad \tilde{\eta} := e\sin\varpi \tag{3.20}$$

which satisfy:

$$\begin{aligned} \tilde{\xi} &= \xi\cos(f_j + \varpi_j) + \eta\sin(f_j + \varpi_j) = e_j X_{L_i}^3 \cos\varpi_j + (X_{L_i}^3 - 1)\cos(f_j + \varpi_j) \\ \tilde{\eta} &= \xi\sin(f_j + \varpi_j) - \eta\cos(f_j + \varpi_j) = e_j X_{L_i}^3 \sin\varpi_j + (X_{L_i}^3 - 1)\sin(f_j + \varpi_j) \end{aligned} \tag{3.21}$$

i.e. $(\tilde{\xi}, \tilde{\eta})$ describes a circumference parameterized by f_j whose radius and center are $|X_{L_i}^3 - 1|$ and $(e_j X_{L_i}^3 \cos\varpi_j, e_j X_{L_i}^3 \sin\varpi_j)$ respectively. We emphasize that $|X_{L_i}^3 - 1| \sim 3r_{\text{Hill}}$ where $r_{\text{Hill}} = \sqrt[3]{\frac{\varepsilon_j}{3}}$. The true anomaly f and the longitude of perihelion ϖ of L_i are computed by inversion from ξ, η

and $\tilde{\xi}, \tilde{\eta}$. We note that[3]

$$\begin{aligned} &\text{if } 3r_{\text{Hill}} \gtrsim e_j \Longrightarrow \varpi \in [0, 2\pi],\ f \text{ is bounded} \\ &\text{if } 3r_{\text{Hill}} \lesssim e_j \Longrightarrow \varpi \text{ is bounded}, f \in [0, 2\pi]. \end{aligned} \tag{3.22}$$

Hence, for those planets fulfilling $3r_{\text{Hill}} \lesssim e_j$, the longitude of the perihelion of L_1 and L_2 is bounded on a interval whose length is

$$\Delta\varpi \sim 2 \arctan \frac{3r_{\text{Hill}}}{e_j}. \tag{3.23}$$

In Table 3.1 we write the mass, the semi-major axis, the eccentricity, the longitude of perihelion and $3r_{\text{Hill}}$ of Mercury, the Earth, and Mars. We note that for Mercury and Mars we have $3r_{\text{Hill}} \lesssim e_j$, hence the true anomaly of the Lagrangian points are such that $f \in [0, 2\pi]$ and ϖ is bounded in some interval whose length is 0.11, and 0.30 respectively. In Figure 3.2 we plot the eccentricity, lon-

Celestial body	Mass (kg)	a_j (AU)	e_j	ϖ_j (deg)	$3r_{\text{Hill}}$ (s.u.)	$\frac{\varepsilon_j}{1+e_j}$ (s.u.)	$\frac{\varepsilon_j}{1-e_j}$ (s.u.)
Sun	1.9885×10^{30}	–	–	–	–	–	–
Mercury	3.302×10^{23}	0.387	2.06×10^{-1}	77	0.011	1.38×10^{-7}	2.09×10^{-7}
Earth	5.97237×10^{24}	1	1.67×10^{-2}	463	0.03	2.95×10^{-6}	3.05×10^{-6}
Mars	6.41712×10^{23}	1.52	9.336×10^{-2}	336	0.014	2.95×10^{-7}	3.56×10^{-7}

Table 3.1: Values of mass, semi-major axis, eccentricity, and longitude of perihelion used for the numerical experiments presented in this paper. On the sixth column we wrote the value of $3r_{\text{Hill}}$ in each Sun–planet standard unit (s.u.), On the seventh and eighth columns we wrote (in each Sun–planet standard unit) the minimum and maximum value of $\varepsilon_j(1 + e_j \cos f_j)/(1 - e_j^2)$ with respect to the true anomaly f_j.

gitude of perihelion, and true anomaly associated to the Lagrangian solutions of the Sun–Mercury, Sun–Earth, and Sun–Mars ER3BPs computed through Eqs. (3.19) and (3.21). We remark that in the circular restricted three-body problem (CR3BP), the eccentricity and true anomaly of L_1 and L_2 are constants, while the longitude of perihelion varies linearly in $[0, 2\pi]$. Hence, one of the biggest difference between the CR3BP and the ER3BP is that the values of the longitude of perihelion associated to L_1 and L_2 can be bounded or not.

Computation of the orbital elements evolution for solutions in the manifold tubes. To highlight the properties of the time evolution of the orbital elements for the solution in the manifold tubes we numerically integrate the equations of motion of the spacecraft using the ER3BP, with initial data computed through the Floquet-Birkhoff normal forms for different values of f_j for the Sun–Mercury and Sun–Earth systems, and we calculate numerically the orbital elements using the `swift` package. For both systems we consider three orbits of the stable manifold tube of L_2 whose initial data are computed for $I_1 = 5 \times 10^{-7}$, $P_2 = 10^{-5}$, and $f_j = 1, 3.5$ and 6; the orbits in the rotating-pulsating reference frame, their projection on the Oxy reference frame, and the orbital elements evolution are plotted in Figures 3.3 and 3.4. Accordingly to the previous discussion, we note that:

- when the spacecraft is close to the Lagrangian solution (referring to the labels of the figures, when Δt is close to 0) the orbital elements oscillate around those of the equilibrium;

- some time after the moment in which the spacecraft leaves the planet Hill sphere the orbital

[3]We recall that all the dimensional quantities, such as the Hill radius and the semi-major axis, are expressed in these formulas in the rescaled units of measure so that the planet is at distance 1 from the Sun, referred as *standard units*.

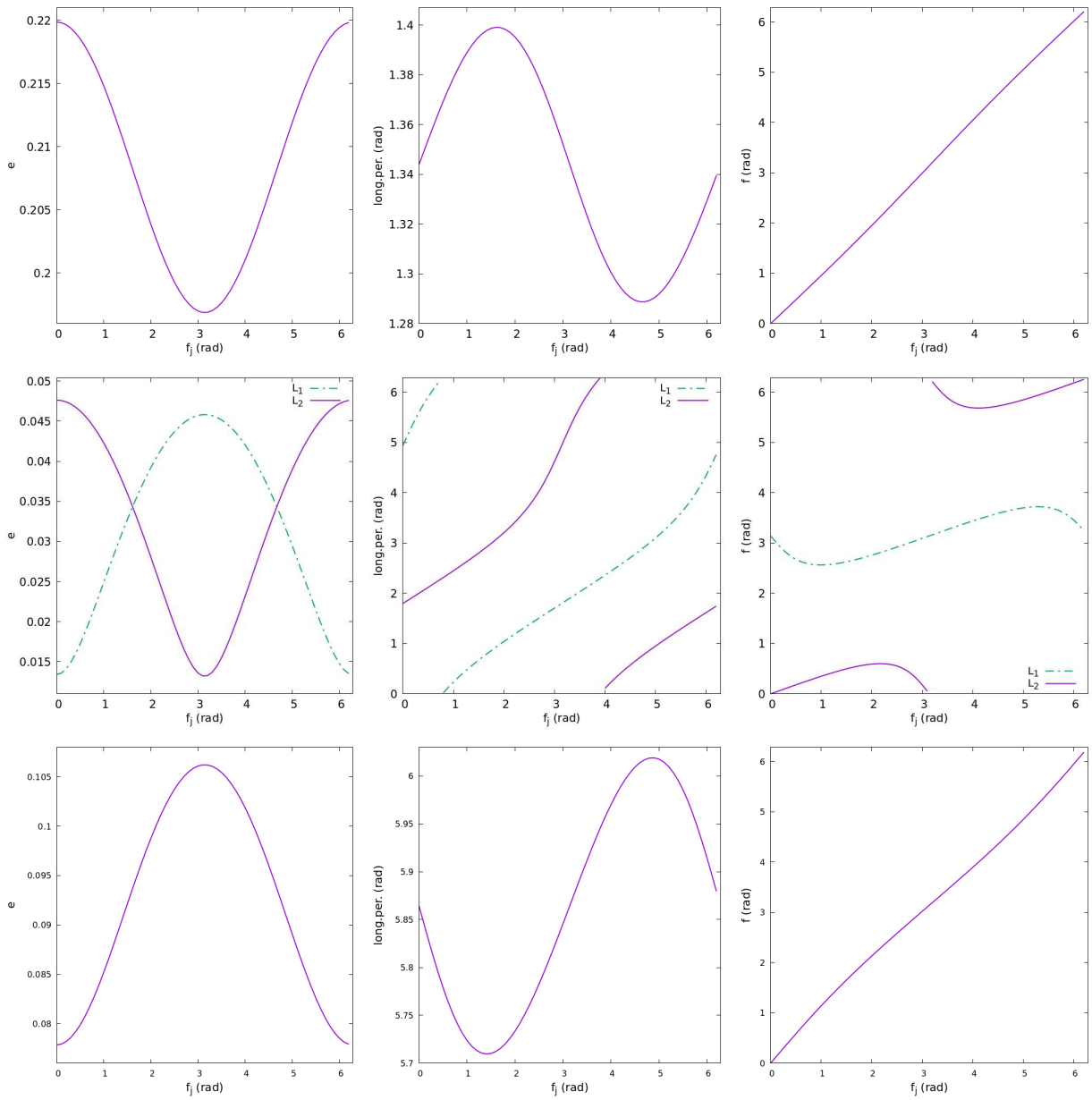

Figure 3.2: Evolution of the eccentricity, longitude of perihelion, and true anomaly of: L_2 in the Sun–Mercury ER3BP (top panels); L_1 (dashed line) and L_2 (continuous line) in the Sun–Earth ER3BP (middle panels); L_1 in the Sun–Mars ER3BP (bottom panels).

elements stabilize and the orbit is well approximated by a Keplerian one (up to an eventual close encounter with the planet). In the figures, we plotted in gray and pink the part of the orbit before such stabilization, in black and red the part of the orbit after such stabilization;

- the eccentricity and the longitude of perihelion stabilize quickly in all the cases. This implies that for those system characterized by $3r_{\text{Hill}} \lesssim e_j$, such as that of Mercury and Mars, the distribution of the longitude of the perihelion of the orbits in the manifold tubes, when they are far from the planet Hill sphere, is bounded.

- in the case of Mercury, the final values of ϖ belong to an interval of amplitude comparable to the value $\Delta\varpi \sim 0.11$ provided by Eq. (3.23).

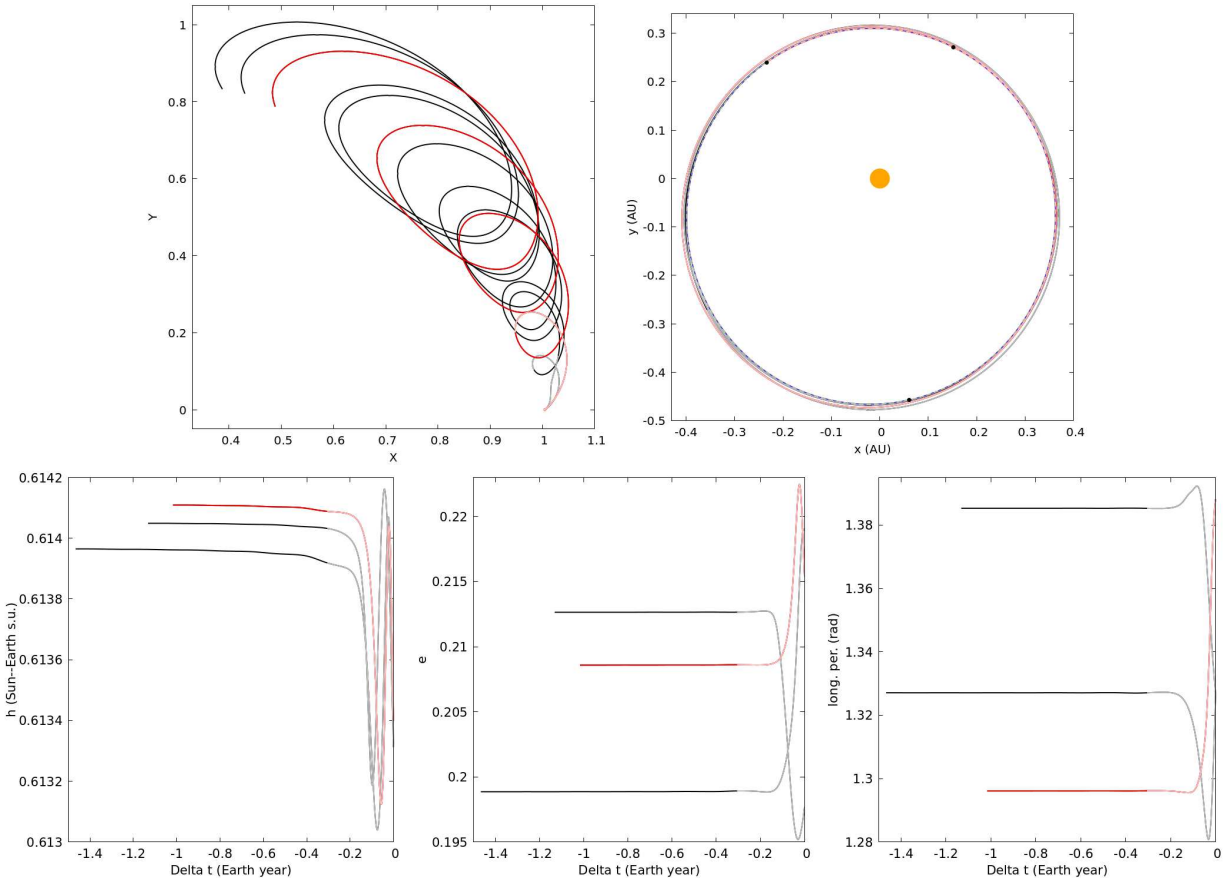

Figure 3.3: Representation of three orbits of the Sun–Mercury L_2 stable manifold tube in the rotating-pulsating and Oxy reference frame (top left and top right panel respectively), and the evolution of the angular momentum, eccentricity, and longitude of perihelion (bottom panels). The orbits were computed by integrating the initial data obtained through the Floquet-Birkhoff normal forms with $I_1 = 5 \times 10^{-7}$, $\phi_1 = 0$, $Q_2 = 0$, $P_2 = 10^{-5}$ and for different values of the initial true anomaly of Mercury; we choose $f_j = 1, 3.5, 6$. The position of the Sun and the initial data in the Oxy reference frame are plotted in the second panel through orange and black filled circles respectively. We plot in gray and pink the part of the orbits that are not in the Keplerian phase (see the previous discussion of the phases (i), (ii), (iii) for a solution in the manifolds tubes) and in black and red the part of the orbits that are in the Keplerian one.

Relevance for Hohmann transfers. From a space flight dynamics point of view, this implies that if the orbits in the families of the manifold tubes of two planets P_h, P_k have both bounded distribution of the longitudes of the perihelion, and if the intervals of these distributions do not match, it is not possible to perform an Hohmann transfer between the unstable manifold tube

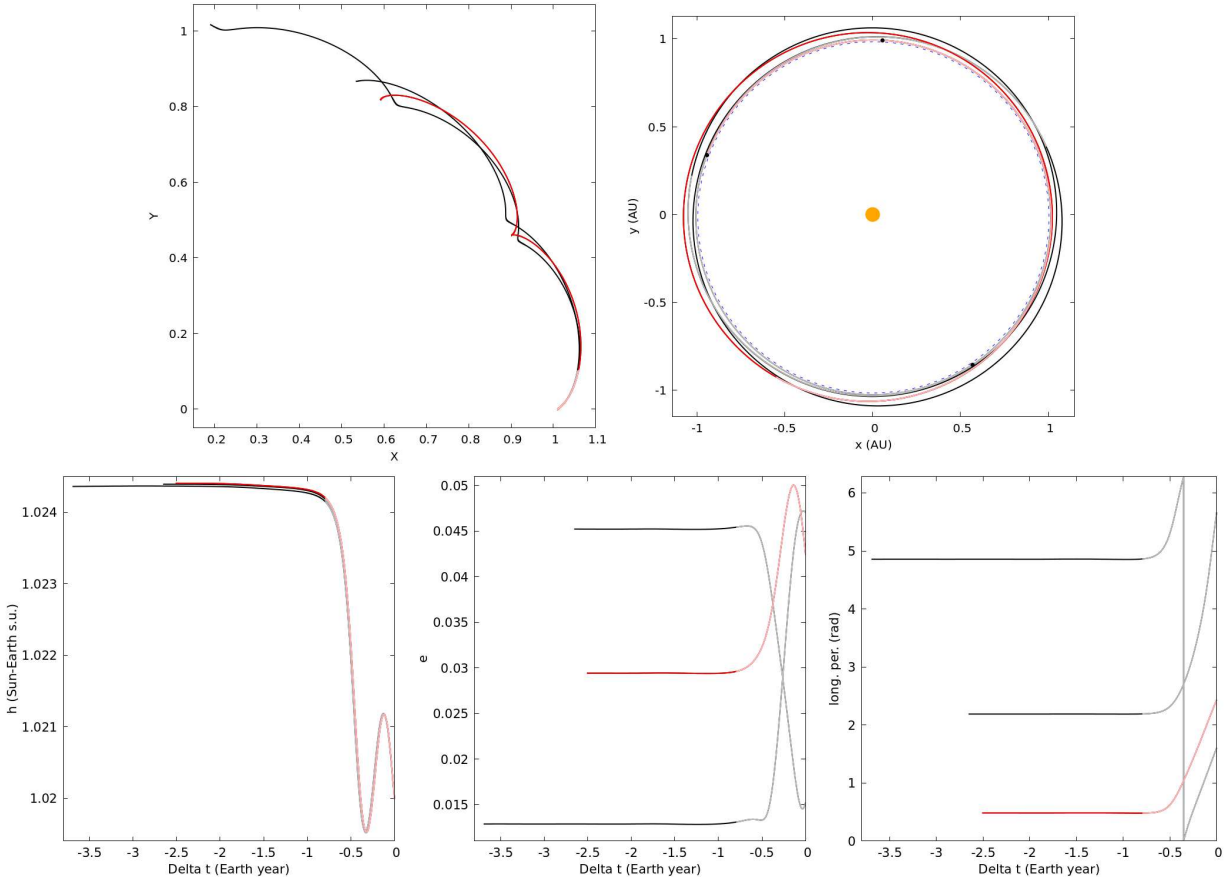

Figure 3.4: Representation of three orbits of the Sun–Earth L_2 stable manifold tube in the rotating-pulsating and Oxy reference frame (top left and top right panel respectively), and the evolution of the angular momentum, eccentricity, and longitude of perihelion (bottom panels). The orbits were computed by integrating the initial data obtained through the Floquet-Birkhoff normal forms with $I_1 = 5 \times 10^{-7}$, $\phi_1 = 0$, $Q_2 = 0$, $P_2 = 10^{-5}$ and for different values of the initial true anomaly of Mercury; we choose $f_j = 1, 3.5, 6$. The position of the Sun and the initial data in the Oxy reference frame are plotted in the second panel through orange and black filled circles respectively. We plot in gray and pink the part of the orbits that are not Keplerian, and in black and red the part of the orbits that are Keplerian. The dashed ellipse in the top right panel represents L_2 position in the Oxy reference frame.

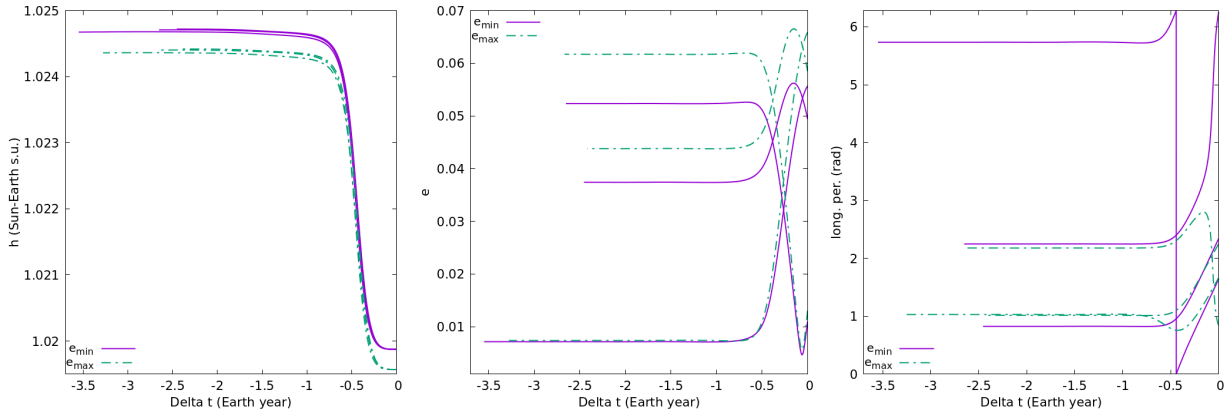

Figure 3.5: Orbital elements evolution for different orbits in two ER3BPs where the planet P_j has the same gravitational parameter of the Earth and eccentricities $e_{\min} = \overline{e}_j - \Delta e$ (continuous line) and $e_{\max} = \overline{e}_j + \Delta e$ (dashed line) with $\Delta e = 5 \times 10^{-3}$.

originating at a collinear point of planet P_h to the stable manifold tube originating at a collinear point of the other planet P_k. In fact, the Hohmann transfer requires that the osculating ellipses of the departing and arrival points are co-axial. In such a case, other types of transfers may be considered, in the context of the ER3BP. If instead the two intervals partially overlap, Hohmann transfers may be found with suitable synchronization of the maneuvers in the context of the ER3BP. We notice that since for the Earth we have $3r_{\text{Hill}} \gtrsim e_h$, then the longitudes of the perihelion of the manifold tubes originating at L_1 and L_2 are distributed in $[0, 2\pi]$, and it is possible to determine an Hohmann transfer pushing the spacecraft from the unstable manifold tubes of the Earth to the stable manifold tubes of Mercury or Mars. In Section 3.3 we provide some sample computations.

A test of the threshold effect. We test the validity of the picture provided above for a fictitious planet having eccentricity e_j close to the threshold value $\overline{e}_j \sim 3r_{\text{Hill}}$. We use as a model problem the gravitational parameter of the Earth, and we consider two values of e_j slightly smaller or larger than $\overline{e}_j$, and we numerically compute backward in time the solutions of the ER3BP with initial data $X = X_{L_2} + 10^{-5}, Y = 0, P_X = 0, P_Y = X_{L_2}$ for different initial true anomalies of the planet, when eccentricities are $e_{\min} = \overline{e}_j - \Delta e$, and $e_{\max} = \overline{e}_j + \Delta e$, with $\Delta e = 5 \times 10^{-3}$; the orbital elements evolution of the numerically computed solutions are shown in Fig. 3.5. From the figure we note that for values of the planet eccentricity slightly smaller or larger than the threshold we obtain a complete different distribution of the longitude of perihelion associated to the manifold tube of the collinear Lagrangian points; in the first case ($e_{\min} \sim 2.5 \times 10^{-2}$) the distribution is spread in $[0, 2\pi]$, in the second case ($e_{\max} \sim 3.5 \times 10^{-2}$) the distribution is bounded on an interval whose length is ~ 1.16. This interval is comparable with the interval $\Delta\varpi \sim 1.42$ provided by Eq. (3.23).

Time evolution of the angular momentum. From the Figures 3.3 and 3.4 we notice that the final values for the angular momentum h for all the orbits are very close (as a matter of fact, much closer than the final values of the eccentricity). In essence, this is a consequence of the fact that already on the Lagrangian solutions the eccentricity has a certain oscillation, while the angular momentum is constant. We therefore compute the time evolution of h as the solution leaves a neighborhood of the Lagrangian one.

By representing the angular momentum and its time derivative using the rotating-pulsating

canonical variables, we have:

$$h = xv_y - yv_x = \sqrt{1-e_j^2}(P_Y X - P_X Y),$$

as well as:

$$\frac{dh}{dt} = \frac{dh}{df_j}\frac{df_j}{dt} = \{h, \mathcal{H}\}\frac{df_j}{dt} = \varepsilon_j \frac{1+e_j\cos f_j}{1-e_j^2}\, Y\left(1 - \frac{1}{((X-1)^2+Y^2)^{3/2}}\right). \tag{3.24}$$

The dependence of $\dot{h}$ on the orbital parameters of the planet appears as a factor multiplying the function:

$$w(X,Y) = Y\left(1 - \frac{1}{((X-1)^2+Y^2)^{3/2}}\right)$$

which depends only on the coordinates X, Y of the rotating-pulsating orbital plane. With evidence, since $\dot{h}$ is proportional to ε_j, far from the planet $|\dot{h}|$ is small; but since the function $w(X,Y)$ is singular for $(X,Y) = (1,0)$, close to the planet $\dot{h}$ is divergent; we also notice that we have $\dot{h} = 0$ for $Y = 0$ (so that we have $\dot{h} = 0$ on the Lagrangian solutions L_1, L_2), and for $(X-1)^2 + Y^2 = 1$. We therefore check the magnitude of the values of $|\dot{h}|$ for (X,Y) in the stable of unstable manifold tubes of interest.

In Fig. 3.6 we represent the values of $w(X,Y)$ using a color scale, and we plot the projection of some unstable manifold tubes of the Sun–Earth system (computed for $I_1 = 5\times10^{-7}$ and $f_3 = 0$) in the vicinity of L_1 and L_2; in the case shown by the figure, the maximum value of $|w(X,Y)|$ in the region visited by the manifold tubes is about 1.3×10^3; since the term $(1+e_j\cos f_j)\varepsilon_j/(1-e_j^2)$ is of order 3×10^{-6} in the Sun–Earth case (the reader is referred to the seventh and eighth columns of Table 3.1), we obtain $|\dot{h}| \sim 4\times10^{-3}$. Moreover, we note that the manifold tubes are going away from the regions characterized by the highest values of $|w(X,Y)|$ (these regions are colored in yellow). For such a reason the values of the angular momentum of the Lagrangian solutions and of the solutions $(X(f_j), Y(f_j), P_X(f_j), P_Y(f_j))$ in the branches of the manifold tubes which go far away from the planet remain very close up to an eventual additional close encounter with the planet. In Figure

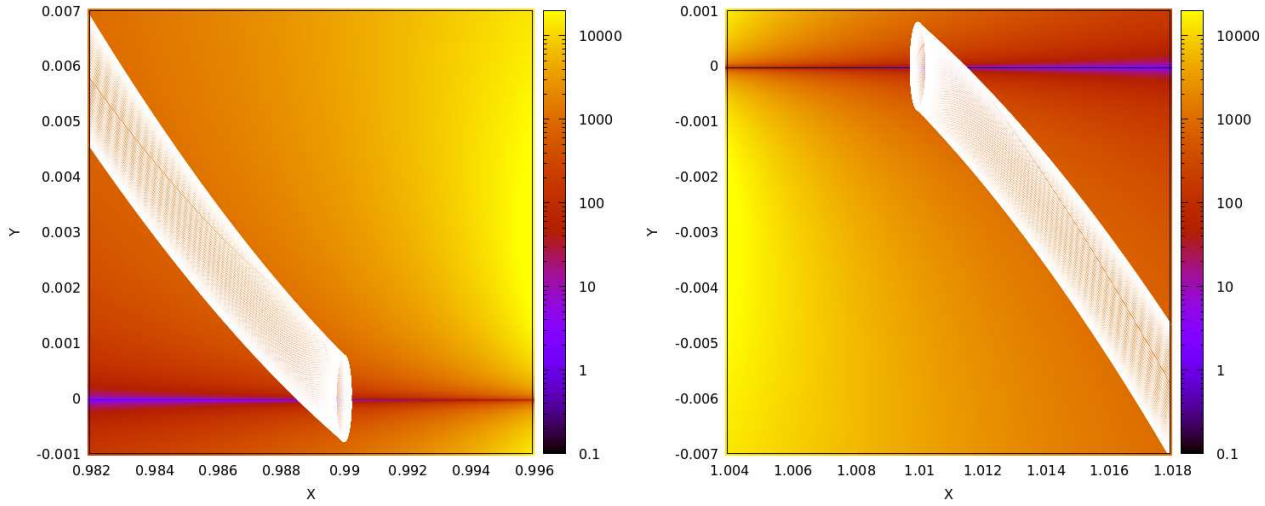

Figure 3.6: Representation of the values of $|w(X,Y)|$ using a logarithmic color scale restricted to the interval $[10^{-1}, 2\times10^4]$. We plot also the the projection of the unstable manifold tubes (white curves) of the Sun–Earth system whose initial data are computed via the Floquet-Birkhoff normal forms at both the Lagrangian points, for $I_1 = 5\times10^{-7}$, $f_j = 0$, $(Q_2, P_2) = (10^{-6}, 0)$ (for L_1), or $(Q_2, P_2) = (-10^{-6}, 0)$ (for L_2), and $\phi_1 \in [0, 2\pi]$.

3.7 we compare the range of the values of the angular momentum with the range of the orbital parameters a, e in for a large set of orbits in the families $\mathcal{K}^u_{I_1}, \mathcal{K}^s_{I_1}$ of the Lagrangian points L_1, L_2 of planets Earth, Mars and Mercury which are of interest for interplanetary transfers from the Earth to Mars or Mercury (i.e. we consider $\mathcal{K}^s_{I_1}$ of the Sun-Mercury L_2 and of the Sun-Mars L_1, and $\mathcal{K}^u_{I_1}$ for both Sun-Earth L_1, L_2). The represented values have been obtained from numerical integrations of the ER3BP with initial conditions in the manifold tubes, computed using the Floquet-Birkhoff normal forms of order $N = 6$, by fixing the values of I_1 and Q_2 (if we are considering the unstable manifold), or P_2 (if we are considering the stable manifold). On this occasion we generated the initial data by changing $\phi_1 \in [0, 2\pi]$ as well as the initial true anomaly of the planet $f_j \in [0, 2\pi]$; in such a way we are considering a large sample of the points of the planar torus $\mathcal{T}_{I_1}$. We generate initial data for two values of $I_1 = 5\times10^{-9}$ and $I_1 = 5\times10^{-7}$, using a uniform sampling of $\phi_1 \in [0, 2\pi]$ and $f_j \in [0, 2\pi]$. The solutions on the unstable manifold tube are numerically integrated for positive times, and the integration is stopped when the spacecraft is at the aphelion and is far from the planet; the solutions on the stable manifold tube are numerically integrated for negative times, and the integration is stopped when the spacecraft is at the perihelion and is far from the planet. The panels of Fig. 3.7 represent the values of the eccentricity and longitude of perihelion (vs the value of the angular momentum) of the spacecraft at these stopping points. We note that for the smaller value of I_1 we obtain a smaller interval for the angular momentum values (because greater amplitudes of the invariant torus represent larger oscillations around the equilibrium solutions), while the intervals for the eccentricity and the longitude of perihelion do not change so much by changing I_1.

3.3 Application to interplanetary missions

The previous theory of computation of the families $\mathcal{K}^u_{I_1}, \mathcal{K}^s_{I_1}$ of Keplerian orbits in the manifold tubes of the Lagrangian solutions L_1, L_2 of the ER3BP has been specifically formulated to design interplanetary transfers. We illustrate an application using the simplest transfer maneuvers, i.e. the Hohmann transfers, between the orbits in the sets $\mathcal{K}^u_{I_1}, \mathcal{K}^s_{I_1}$ of the Lagrangian solutions L_1 or L_2 of the ER3BPs defined by two planets P_h, P_k: from the unstable manifolds of L_1, L_2 of the Sun–Earth ER3BP we transfer to the stable manifold of L_2, L_1 of the Sun–Earth and Sun–Mars ER3BPs respectively (we do not consider transfers from the Earth to Venus only because both planets have a small value of the orbital eccentricity, and the transfers can be conveniently designed using the two related CR3BPs). The initial conditions and the maneuvers of the transfers are computed using the ER3BPs, but we also check the effectiveness of the method with a numerical integration of the BER4BP, accounting of the gravitational interactions of the spacecraft with both planets P_h, P_k during the full time interval needed for the spacecraft to move from a neighborhood of the Lagrangian solution of P_h to a neighborhood of the Lagrangian solution of P_k.

The Hohmann transfer consists in two impulsive orbital maneuvers at two points A and B that are the aphelion and perihelion (or perihelion and aphelion) respectively of two osculating coplanar and co-axial ellipses in the families $\mathcal{K}^u_{I_1}, \mathcal{K}^s_{I_1}$.

We denote by A the aphelion or perihelion of the Keplerian orbit where the first maneuver is performed, and by B the perihelion or aphelion of the Keplerian orbit where the spacecraft is injected after the second maneuver. The possible values for the angular momentum, eccentricity and longitude of perihelion of A and B that can be used for the different transfers have been plotted in

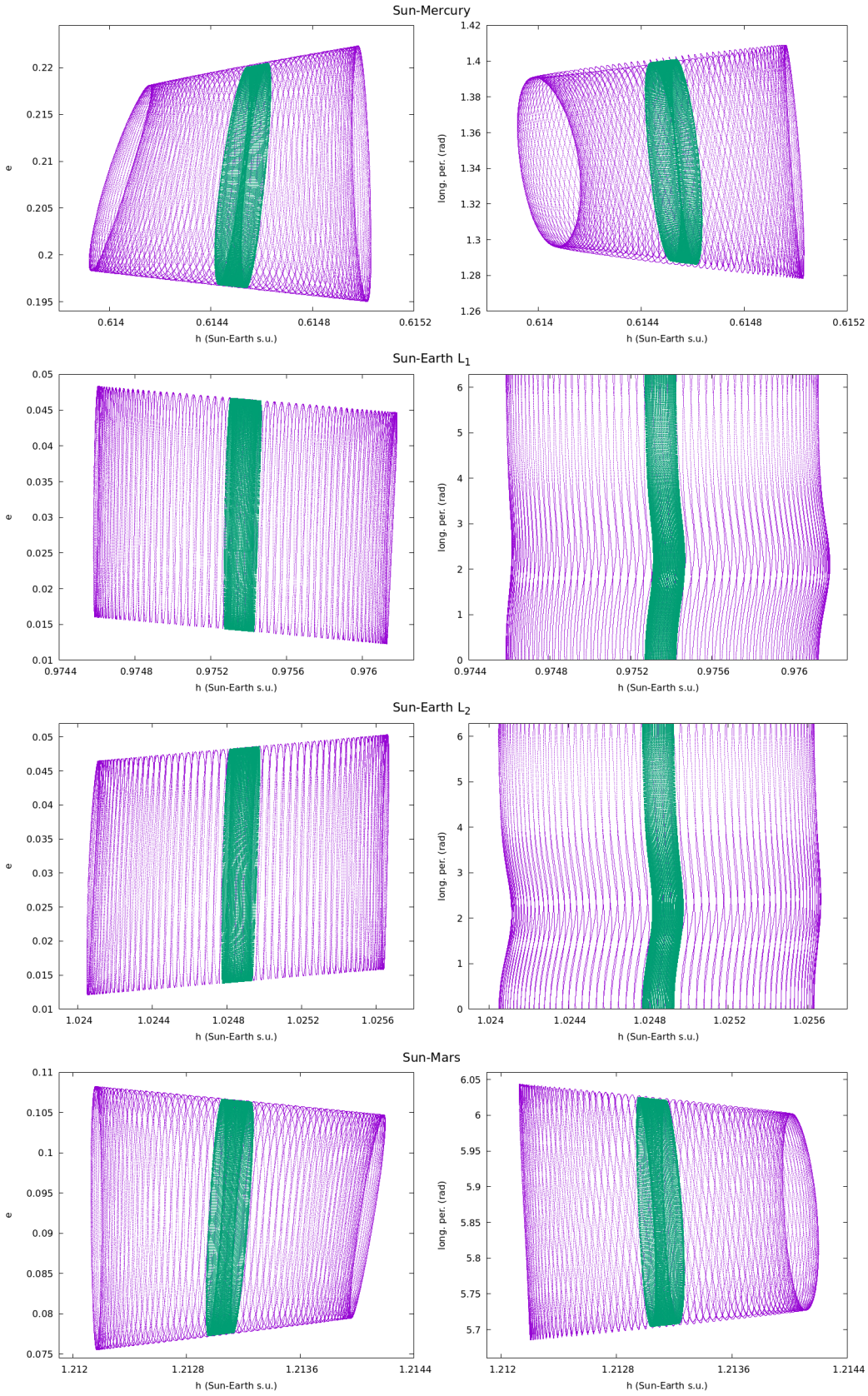

Figure 3.7: Values of the angular momentum, eccentricity, and argument of perihelion at the stopping points for a large set of orbits in the family associated to the stable manifold tubes of the Sun–Mercury L_2 point (top panels), unstable manifold tubes of the Sun–Earth L_1 and L_2 points (middle panels), and the stable manifold tubes of the Sun–Mars L_1 point (below panels). The violet and green points refer the orbital elements of the tube manifolds computed with $I_1 = 5 \times 10^{-7}$ and $I_1 = 5 \times 10^{-9}$ respectively.

Fig. 3.7; we remark that, as explained in the previous Section, the possible longitudes of perihelion of the points A, B of the Sun–Mercury and Sun–Mars systems are distributed in a bounded interval $[\varpi_{\min}, \varpi_{\max}]$, while they spread in $[0, 2\pi]$ in the Sun–Earth case.

Transfers in the two decoupled ER3BPs. We denote by $\mathcal{S}_A$ and $\mathcal{S}_B$ the sets containing the angular momentum, eccentricity, longitude of perihelion, and the value of the true anomaly of the planet associated to the stopping points in the Sun–Earth unstable manifold, and in the Sun–Mercury (or Sun–Mars) stable manifold respectively. Each element in $\mathcal{S}_A$ represents the aphelion of the Keplerian orbit associated to the unstable manifold tube in the Sun–Earth system computed by integrating in the future the ER3BP with initial data $\boldsymbol{r}_{in}$ in the Oxy reference frame, and identifies the time-span Δt_A needed by the spacecraft to depart from $\boldsymbol{r}_{in}$ and reach A. Each element in $\mathcal{S}_B$ represents the perihelion of the Keplerian orbit associated to the stable manifold tube in the Sun–Mercury or Sun–Mars system, computed by integrating in the past the ER3BP with initial data $\boldsymbol{r}_{fin}$, and identifies the time-span Δt_B needed by the spacecraft to depart from B and reach $\boldsymbol{r}_{fin}$. Since the longitudes of perihelion associated both the manifold tube of the Sun–Mercury and Sun–Mars systems are distributed in a bounded interval $[\varpi_{\min}, \varpi_{\max}]$, while they are spread in $[0, 2\pi]$ in the Sun–Earth case (the reader is referred to Sec. 3.2 for further details), we decided to compute the optimal Hohmann transfer between the points defined by $\mathcal{S}_A$ and $\mathcal{S}_B$ by: i) selecting only the points $A' \in \mathcal{S}_A$ characterized by longitudes of perihelion in the interval $[\varpi_{\min}, \varpi_{\max}]$; ii) for each point A', selecting the point $B'' \in \mathcal{S}_B$ whose longitude of perihelion is the closer one in the sampling of the set $\mathcal{S}_A$: then we consider the point B' having the same angular momentum and eccentricity of B'', the same longitude of perihelion of A', and whose time-span to arrive at the vector state in the local stable manifold tube is $\Delta t_{B''}$; iii) once we determined all the possible pair (A', B'), we consider only the pair (A, B) characterized by the minimum value of the Hohmann delta-v. In the first and third panel of Fig. 3.8 we plot the total time-span and the corresponding delta-v needed for the whole transfer between the Earth and Mercury (top panels) and the Earth and Mars (below panels) for all the pairs (A', B') found in $\mathcal{S}_A$ and $\mathcal{S}_B$; for both transfers, we consider the sets $\mathcal{S}_A$ and $\mathcal{S}_B$ defined by $I_1 = 5 \times 10^{-7}$. In the second and fourth panel of Fig. 3.8 we plot the initial true anomalies at epoch $t = 0$ with the corresponding delta-v needed for the transfer of the planets found for the Earth–Mercury and the Earth–Mars transfer respectively. We note from Fig. 3.8 that the difference between the maximum and the minimum delta-v is small (about 0.32 km/s and 0.12 km/s for the Earth–Mercury and the Earth–Mars transfer). In Table 3.2 the minimum values of delta-v in the Earth–Mercury transfers obtained by changing the value of I_1 are written. Once we determine the pair (A, B), we obtain the initial data $\boldsymbol{r}_{in}$, i.e. the initial

Sun–Earth \ **Sun–Mercury**	$\mathbf{5 \times 10^{-7}}$	$\mathbf{5 \times 10^{-9}}$
$\mathbf{5 \times 10^{-7}}$	15.543	15.581
$\mathbf{5 \times 10^{-9}}$	15.566	15.603

Table 3.2: Values of the minimum delta-v (in km/s) needed by an Hohmann transfer between $\mathcal{K}^u_{I_{1,E}}$ of the Sun–Earth L_1 and $\mathcal{K}^s_{I_{1,Me}}$ for different values of $I_{1,E}$ and $I_{1,Me}$, whose values are written in the first column and first row respectively.

position vector in the Oxy reference frame of the transfer belonging to the unstable Sun–Earth manifold tube, the time-span Δt_A needed by the spacecraft to reach $\boldsymbol{r}_A$ (the position vector in Oxy identified by A), the time-span Δt_{tr} needed to transfer the spacecraft from $\boldsymbol{r}_A$ to $\boldsymbol{r}_B$ (the position

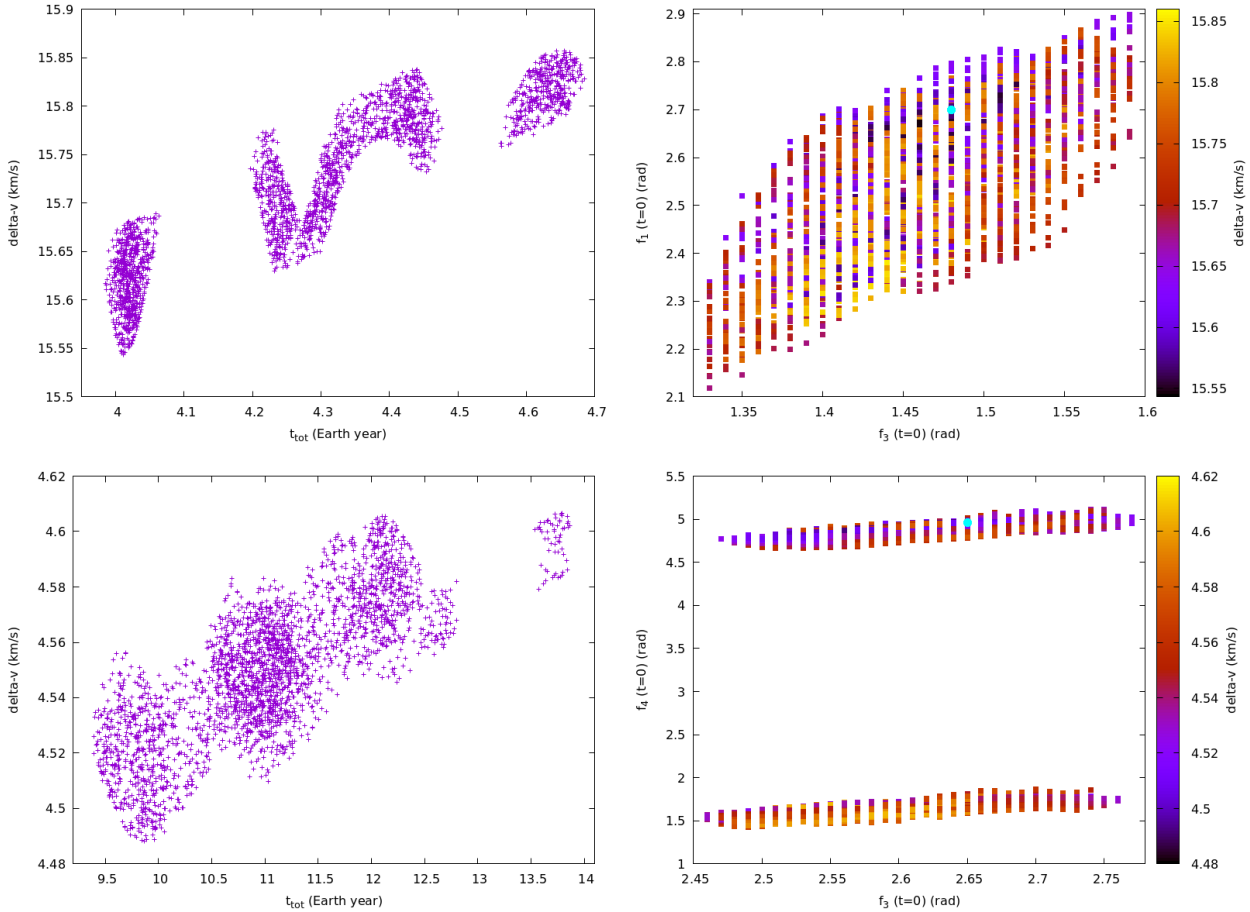

Figure 3.8: Top panels: values of delta-v found for the transfer between $\mathcal{K}^u_{I_1}$ of the Sun–Earth L_1 and $\mathcal{K}^s_{I_1}$ of the Sun–Mercury L_2 with $I_1 = 5 \times 10^{-7}$. Below panels: Values of delta-v found for the transfer between $\mathcal{K}^u_{I_1}$ of the Sun–Earth L_2 and $\mathcal{K}^s_{I_1}$ of the Sun–Mars L_1 with $I_1 = 5 \times 10^{-7}$. On the left of both the top and below panels, the total time interval needed for the whole transfer and the corresponding value of delta-v are shown; on the right, the values of delta-v for different initial true anomalies at epoch $t = 0$ of the planets at the beginning of the whole transfer. The cyan points indicate the values of the initial true anomalies corresponding to the minimum value of delta-v (about 15.543 km/s for the Earth–Mercury case, and 4.488 km/s for the Earth–Mars case).

vector in Oxy identified by B) through the Hohmann transfer, and the time-span Δt_B needed to reach the final vector state $\boldsymbol{r}_{fin}$. For the integration of the transfer we consider the equations of motion (3.2) where: i) from the starting point $\boldsymbol{r}_{in}$ to $\boldsymbol{r}_A$ we consider only the gravitational effects due to the Sun and the Earth; ii) from $\boldsymbol{r}_A$ to $\boldsymbol{r}_B$ we consider only the gravitational effects due to the Sun; iii) from $\boldsymbol{r}_B$ to $\boldsymbol{r}_{fin}$ we consider only the gravitational effects due to the Sun and Mercury (or Mars).

In Fig. 3.9 we plot the transfer between the Earth and Mercury; the manifold tubes in both Sun–Earth and Sun–Mercury systems were computed by defining $I_1 = 5 \times 10^{-7}$. In the top left panel, the transfer is shown in the Oxy reference frame, where the brown filled circle represent the location of Mercury at the end of the transfer, the black and cyan points represent $\boldsymbol{r}_{in}$, $\boldsymbol{r}_A$ and $\boldsymbol{r}_B$. The panels below show the projection of the whole transfer in both the Sun–Earth and Sun–Mercury rotating-pulsating reference frame.

Transfers in the BER4BP. Since the positions vector $\boldsymbol{r}_{in}$, $\boldsymbol{r}_A$, $\boldsymbol{r}_B$ and $\boldsymbol{r}_{fin}$ are sufficiently far from Mercury (or Mars) and the Earth respectively, and also the gravitational parameters of these planets are small, when we integrate the equations of motion by considering the gravitational effects of the Sun, the Earth, and Mercury (or Mars) we expect that only small changes appear. For the computation of the orbital transfer, we decided to: i) integrate the Eqs. (3.2) considering both Earth and Mercury (or Mars) with initial datum $\boldsymbol{r}_{in}$, and stop the integration when the time-span is Δt_A (let $\boldsymbol{r}_{\tilde{A}}$ be the position vector of the stopping point); ii) integrate Eqs. (3.2) by using as initial position vector $\boldsymbol{r}_{\tilde{A}}$ and as initial velocity vector the same Cartesian velocity vector found through Hohmann method for the transfer from A to B in the decoupled ER3BPs (the time-span of integration is Δt_{tr}, and let $\boldsymbol{r}_{\tilde{B}}$ be the position vector of the stopping point); iii) integrate the Eqs. (3.2) with initial vector position $\boldsymbol{r}_{\tilde{B}}$ and as velocity vector the same Cartesian velocity vector of the point B found in the arrival Sun–planet ER3BP. The integration time interval is Δt_B.

In the first panel of Fig. 3.10 we show the transfer between the Earth and Mercury using the BER4BP; both the manifold tubes of the Sun–Earth L_1 point and the Sun–Mercury L_2 points were computed using the Floquet-Birkhoff normal form with $I_1 = 5 \times 10^{-7}$. The transfer is almost equal to the transfer found using the ER3BPs (the reader is referred to the first panel of Fig. 3.9). This is because both Mercury and the Earth does not perturb so much the motion of the spacecraft when the latter is on the manifold of the Earth and Mercury respectively (the reader is referred to the right panel in Fig. 3.10 where the distance between the spacecraft and the Earth, and the spacecraft and Mercury during the whole transfer are plotted).

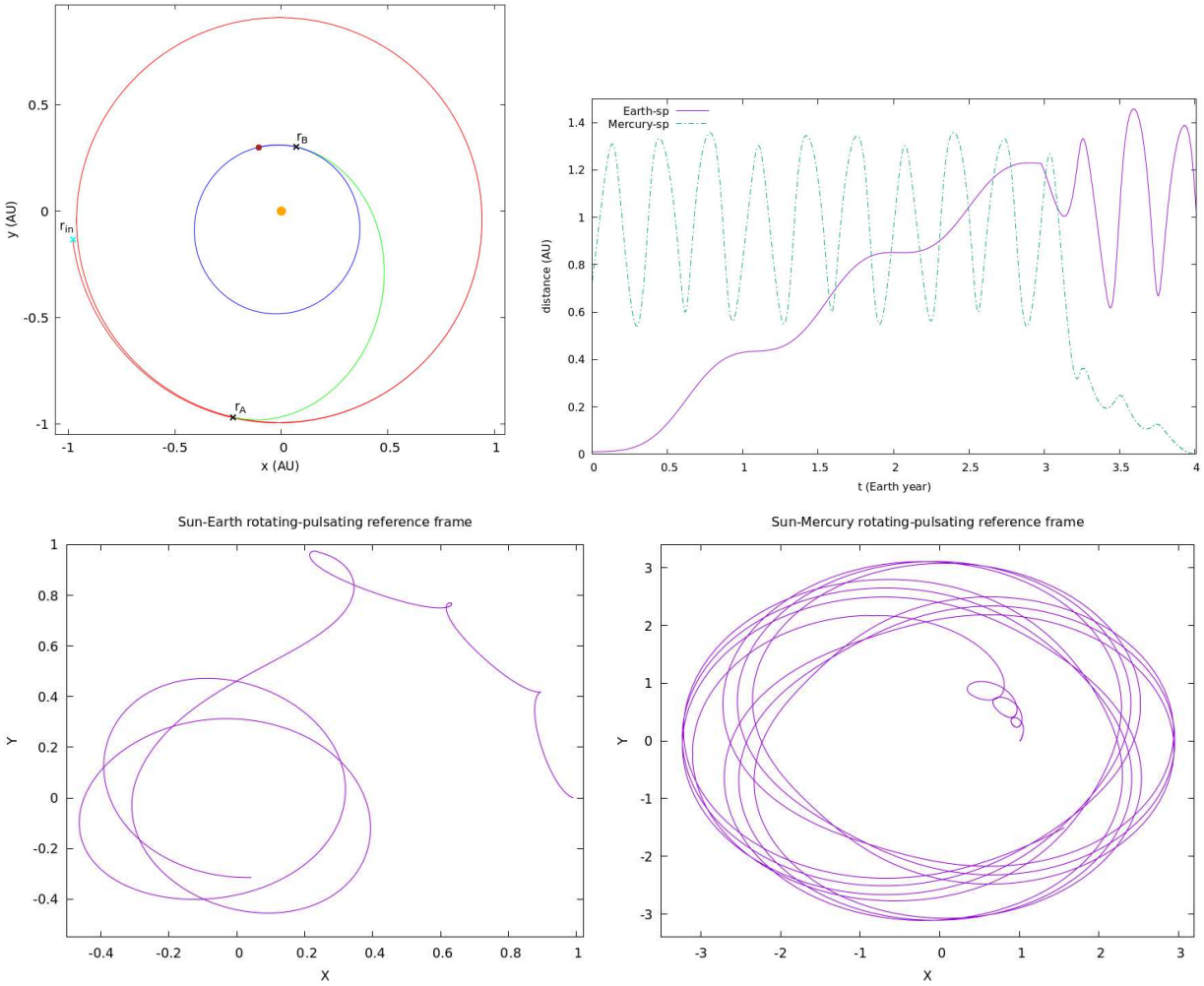

Figure 3.9: Transfer in the decoupled ER3BPs between the unstable manifold tube of the Sun–Earth L_1 (red orbit) and the stable manifold tube of the Sun–Mercury L_2 (blue orbit) in the Oxy reference frame (top left panel); for both system we compute the manifold tubes by imposing $I_1 = 5 \times 10^{-7}$ in the Floquet-Birkhoff normal forms. The brown filled circle represents the location of Mercury at the end of the transfer, while the black and cyan points denote the location of $\boldsymbol{r}_{in}$, $\boldsymbol{r}_A$, and $\boldsymbol{r}_B$. The top right panel displays the distance between the spacecraft and the Earth (continuum line) and Mercury (dashed line) in the Oxy reference frame. The projection of the transfer in the Sun–Earth and Sun–Mercury rotating-pulsating reference frame is shown in the last two panels. For the integration we use the Sun–Earth standard unit of measure, i.e. the gravitational parameters of the Earth and the Sun are respectively $\varepsilon_3 = M_3/(M_0 + M_3)$, $\mu = 1 - \varepsilon_3$, the semi-major axis of the Earth is equal to one, while the gravitational parameters of Mercury and Mars are $\varepsilon_j = M_j/(M_0 + M_3)$ with $j = 1, 4$ (M_0, M_1,M_3 and M_4 are the masses of the Sun, Mercury, the Earth and Mars respectively; their values are represented in the second column of Table 3.1).

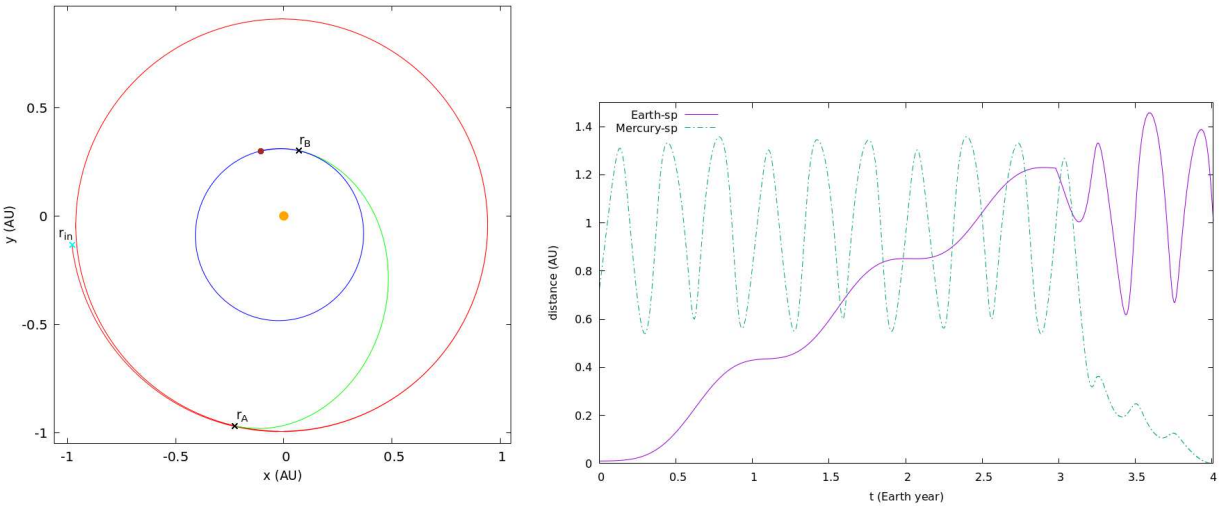

Figure 3.10: Left panel: transfer between the Earth and Mercury in the BER4BP (for the integration we use the Sun–Earth standard unit). Right panel: distance between the spacecraft and the Earth (continuous line), and the spacecraft and Mercury (dashed line) in the Oxy reference frame during the whole transfer.

Conclusion and perspectives

The Sun–Earth circular restricted three-body problem has been deeply investigated in connection to astrodynamics. This is because the Sun—Earth Lagrangian points L_1, L_2 and L_3 represent ideal locations for the observation of the Solar activities and space environment. As a matter of fact, there exists a lot of literature about the dynamics originating at the L_1 and L_2 points in the circular restricted three-body problem and the possibility to transfer a spacecraft between these two points via the heteroclinic intersections of their manifold tubes; moreover, several space missions were designed to reach the vicinity of the Sun—Earth Lagrangian points L_1 and L_2 (for example ISEE-3, WMAP, Herschel and Planck) and to exploit the heteroclinic connections as a low-energy transfer between L_1 and L_2 (for example Genesis and SOHO).

Since the circular restricted three-body problem gives only a crude approximation of the spacecraft dynamics in the Solar System, an extension of the study related to the solutions originating at the Lagrangian points is required. For these reasons, we decided to analyze the solutions originating at the Sun-Earth Lagrangian points L_1, L_2 and L_3 in the presence of the planetary perturbations, and to consider the elliptic shape of the planetary orbits in connection to space flight dynamics. For this purpose, we introduce several models for the motion of a spacecraft between the circular restricted three-body problem and a realistic model of the Solar System which is compatible with the precision of the JPL digital ephemerides. More precisely, we consider the elliptic restricted three-body problem, the multicircular restricted eight-body problem as well as the bi-elliptic restricted four-body problem. When we study the latter problems, several difficulties appear, since for the models mentioned above no global constants of motion are known and the development of perturbations theory is complicated. In this thesis we show how the combination between Hamiltonian Mechanics, Dynamical Systems and numerical modelization represents a powerful tool for the investigation of the spacecraft dynamics in models that are more realistic than the circular one, and for the study of the solutions of the restricted N-body problem in connection to space flight dynamics.

More precisely, the PhD research objective is twofold:

1) determination of libration orbits in the vicinity of the Sun–Earth L_3 point in a model of the Solar System that is compatible with the ephemerides provided by the JPL Horizon digital service;

2) determination of transfer orbits between the Earth and Mercury, and the Earth and Mars, in the bi-elliptic restricted four-body problem through the exploitation of the manifold tubes originating at the Lagrangian points L_1 and L_2.

To reach these goals we apply the methods typical of the Dynamical Systems and the Hamiltonian perturbation theories. Specifically, we implement the construction of normal forms within the

averaging method and the computation of chaos indicators.

In particular, for the research task 1), thanks to a combination of the Hamiltonian averaging method and the computation of fast Lyapunov indicators, we find orbits in the realistic model of the Solar System that remain in the vicinity of the Sun-Earth L_3 for at least two centuries, and whose libration amplitudes range from 2.5×10^{-4} AU to 3×10^{-2} AU. For the research task 2), we analyze the evolution of the orbital elements in the manifold tubes originating at the Lagrangian points L_1 and L_2 in the elliptic restricted three-body problem; we find a threshold value for the eccentricity of the planet where we have a drastic change in the distribution of the longitudes of perihelion for a family of orbits in the manifold tubes which are of interest for interplanetary transfers. This threshold value allows to identify the cases where the use of the elliptic restricted three-body model is necessary with respect to the circular one, and leads to important changes in the design of an interplanetary mission trajectory between the manifold tubes originating at the Lagrangian points of different Sun–planet elliptic restricted three-body problems.

The results present in the thesis were published in Scantamburlo and Guzzo (2020) and in the preprint Scantamburlo et al. (2021).

The topics presented in this thesis are not fully exhaustive, and the reader will probably ask herself/himself some questions. For example: i) is it possible to design a low-cost and fast (namely in a time-span that is useful for space missions) transfer from the Earth to the vicinity of the Sun—Earth L_3 point in the restricted N-body problem? ii) since the vicinity to the Sun, how does the dynamics around L_1 and L_2 of the Sun—Mercury (or Sun-–Mars) elliptic restricted three-body problem change when we also consider the contribution of the Solar radiation pressure? iii) can we use the chaos indicators for the determination of optimal impulsive maneuvers between the manifold tubes originating at L_1 and L_2 in the elliptic restricted three-body problems? According to us, the combinations of Hamiltonian Mechanics and Dynamical Systems from both a theoretical and numerical point of view will help to answer these questions and to develop further methodologies in modern astrodynamics.

Appendix A

Computation of the orbital elements of L_3 in the co-rotating reference frame

Let us consider the circular restricted three-body problem where the gravitational parameter of the most massive body P_0 is μ and the second body is performing a circular motion around P_0 with angular velocity n and initial phase displacement ϕ. Let $\boldsymbol{r}$ be the position vector of the spacecraft in the inertial reference frame centered at P_0, and $\boldsymbol{R} = (X, Y)^T$ be the position vector of the spacecraft in the co-rotating reference frame. The relation between the two vectors is $\boldsymbol{R} = \mathcal{R}^T \boldsymbol{r}$, where

$$\mathcal{R} = \begin{pmatrix} \cos(nt+\phi) & -\sin(nt+\phi) \\ \sin(nt+\phi) & \cos(nt+\phi) \end{pmatrix}. \tag{A.1}$$

Let $\boldsymbol{r} = \rho(\cos(f+\omega), \sin(f+\omega))^T$ where a, e, ω and f denote the semi-major axis, the eccentricity, the argument of perihelion and the true anomaly of the spacecraft; then

$$\begin{aligned} X &= \frac{a(1-e^2)}{1+e\cos f}\cos(f+\omega-nt-\phi) \\ Y &= \frac{a(1-e^2)}{1+e\cos f}\sin(f+\omega-nt-\phi). \end{aligned} \tag{A.2}$$

Hence

$$\begin{aligned} \dot{X} =& \frac{\partial X}{\partial f}\frac{df}{dt} + \frac{\partial X}{\partial t} \\ =& \sqrt{\frac{\mu}{a(1-e^2))}}(1+e\cos(f))\left(\frac{e}{1+e\cos(f)}\cos(f+\omega-nt-\phi)\sin(f) - \sin(f+\omega-nt-\phi)\right) \\ &+ n\frac{a(1-e^2)}{1+e\cos(f)}\sin(f+\omega-nt-\phi) \\ =& \sqrt{\frac{\mu}{a(1-e^2)}}e\cos(f+\omega-nt-\phi)\sin(f) - \sqrt{\frac{\mu}{a(1-e^2)}}(1+e\cos(f))\sin(f+\omega-nt-\phi) \\ &+ n\frac{a(1-e^2)}{1+e\cos(f)}\sin(f+\omega-nt-\phi) \end{aligned}$$

$$
\begin{aligned}
\dot{Y} =& \frac{\partial Y}{\partial f}\frac{df}{dt} + \frac{\partial Y}{\partial t} \\
=& \sqrt{\frac{\mu}{a(1-e^2))}}(1+e\cos(f))\left(\frac{e}{1+e\cos(f)}\sin(f+\omega-nt-\phi)\sin(f)+\cos(f+\omega-nt-\phi)\right) \\
& - n\frac{a(1-e^2)}{1+e\cos(f)}\cos(f+\omega-nt-\phi) \\
=& \sqrt{\frac{\mu}{a(1-e^2)}}(1+e\cos(f))\cos(f+\omega-nt-\phi) + \sqrt{\frac{\mu}{a(1-e^2)}}e\sin(f)\sin(f+\omega-nt-\phi) \\
& - n\frac{a(1-e^2)}{1+e\cos(f)}\cos(f+\omega-nt-\phi).
\end{aligned}
$$

Then the conjugate momenta to X and Y are

$$
P_X = \dot{X} - nY = -\sqrt{\frac{\mu}{a(1-e^2)}}\left(\sin(f+\omega-nt-\phi)+e\sin(\omega-nt-\phi)\right)
$$

$$
P_Y = \dot{Y} + nX = \sqrt{\frac{\mu}{a(1-e^2)}}\left(\cos(f+\omega-nt-\phi)+e\cos(\omega-nt-\phi)\right);
$$

hence

$$
\frac{P_X^2+P_Y^2}{2} - \frac{\mu}{\sqrt{X^2+Y^2}} = -\frac{\mu}{2a} \tag{A.3}
$$

$$
\begin{aligned}
XP_Y - YP_X =& \frac{\sqrt{\mu a(1-e^2)}}{1+e\cos(f)}\left(1+e\cos(f+\omega-nt-\phi)\cos(\omega-nt-\phi)\right. \\
& \left. +e\sin(f+\omega-nt-\phi)\sin(\omega-nt-\phi)\right) \\
=& \sqrt{\mu a(1-e^2)}.
\end{aligned} \tag{A.4}
$$

The collinear equilibrium point L_3 is characterized by $(X^*, Y^*, P_X^*, P_Y^*) = (X_{L_3}, 0, 0, nX_{L_3})$, with $X_{L_3} < 0$. Let a^*, e^*, ω^* and f^* the semi-major axis, eccentricity, argument of perihelion and true anomaly of L_3. By imposing $Y^* = 0$ and $X^* < 0$ we get $f^* + \omega^* - nt - \phi = \pi$. From $P_X^* = 0$ we obtain the condition $\omega^* - nt - \phi = j\pi$ with $j = 0, 1$, but the sign of $\cos(\omega^* - nt - \phi)$ is not determined. For this reason, we define $k := e^*\cos(\omega^* - nt - \phi)$; we note that $k^2 = (e^*)^2$, and $e^*\cos(f^*) = e^*\cos(\pi - \omega^* + nt + \phi) = -e^*\cos(\omega^* - nt - \phi) = -k$. Hence, from the relation $X^* = X_{L_3}$ we get

$$
|X_{L_3}| = a^*(1+k) \tag{A.5}
$$

and by replacing such condition in $P_Y^* = nX_{L_3}$ we obtain

$$
k = 1 - \frac{(nX_{L_3})^2|X_{L_3}|}{\mu}. \tag{A.6}
$$

Hence

- if $k > 0$, then $\omega^* - nt - \phi = 0$ and $f^* = \pi$;
- if $k < 0$, then $\omega^* - nt - \phi = \pi$ and $f^* = 0$.

The semi-major axis and eccentricity are:

$$
a^* = \frac{|X_{L_3}|}{1+k}, \qquad e^* = |k|. \tag{A.7}
$$

In Fig. A.1 we show the values of the orbital elements in standard unit[1] associated to L_3 for

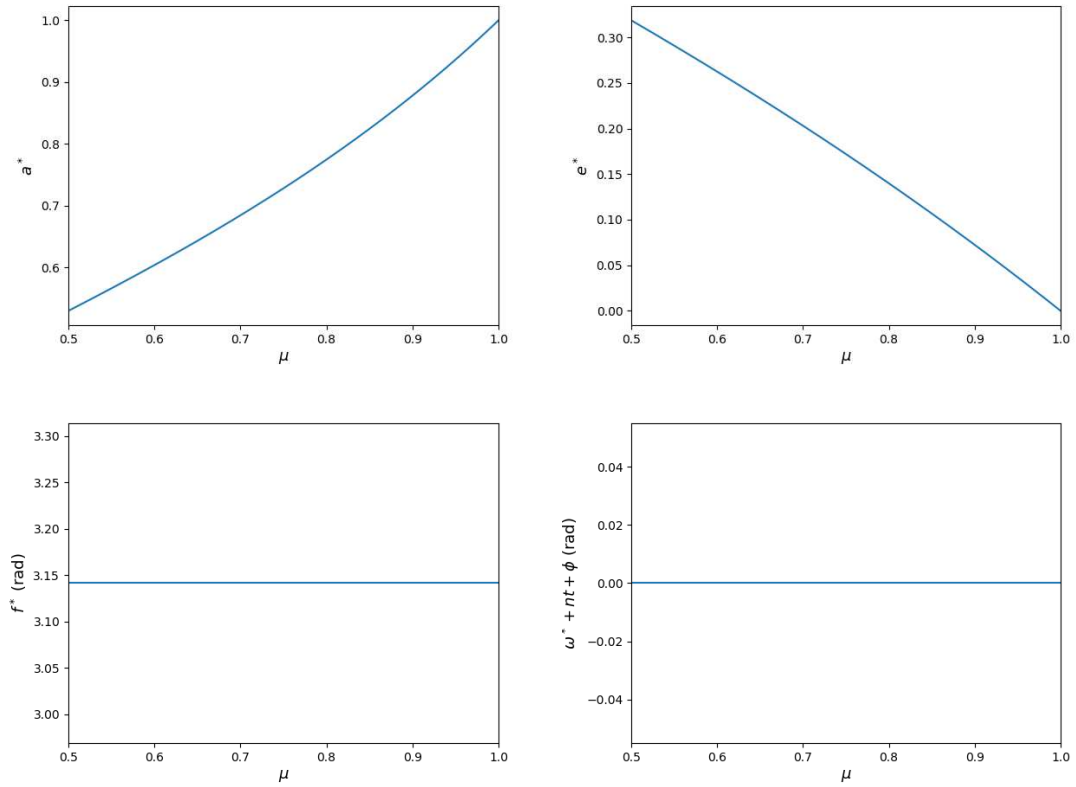

Figure A.1: Representation of the semi-major axis (in standard unit), eccentricity, true anomaly and $\omega^* - nt - \phi$ associated to the Lagrangian point L_3 for different value of μ. We remark that for $\mu \sim 1$ (as in the Sun–Earth case) the eccentricity is close to 0, while the semi-major axis is close to 1.

different values of μ. We remark that L_3 is always located at the aphelion, while its argument of perihelion evolves linearly in time, i.e. $\omega^* = t + \phi$. Moreover, for the Sun-Earth case, in which $\mu \sim 1$ we note that the semi-major axis of L_3 is close to 1, while its eccentricity is close to 0.

[1]The sum of the gravitational parameters of the two massive bodies, the distance between them and the angular frequency of the second body are equal to one.

Appendix B

Comparison between the modified Fast Lyapunov Indicators

Given the first order differential equations

$$\dot{\boldsymbol{\xi}} = F(\boldsymbol{\xi}, t), \qquad \boldsymbol{\xi} \in \mathbb{R}^n,\, t \in \mathbb{R} \tag{B.1}$$

and its variational equations

$$\dot{\boldsymbol{\Xi}} = \left[\frac{\partial F}{\partial \boldsymbol{\xi}}(\boldsymbol{\xi}, t)\right] \cdot \boldsymbol{\Xi}, \qquad \boldsymbol{\Xi} \in \mathbb{R}^n \tag{B.2}$$

where $\frac{\partial F}{\partial \boldsymbol{\xi}}$ represents the Jacobian matrix of F, in Scantamburlo and Guzzo (2020) we defined the modified Fast Lyapunov Indicator as

$$\mathrm{mFLI}(\boldsymbol{\xi}_0, \boldsymbol{\Xi}_0; T) := \max_{t\in[0,T]} \int_0^T \max\left(0, w(\boldsymbol{\xi}(s)) \frac{\boldsymbol{\Xi}(s) \cdot \dot{\boldsymbol{\Xi}}(s)}{\|\boldsymbol{\Xi}(s)\|^2}\right) ds \tag{B.3}$$

with a suitable window function $w : \mathbb{R}^n \to \mathbb{R}^+$, while in Guzzo and Lega (2014, 2015) the chaos indicator was defined as

$$\mathrm{FLI}(\boldsymbol{\xi}_0, \boldsymbol{\Xi}_0; T) := \int_0^T w(\boldsymbol{\xi}(s)) \frac{\boldsymbol{\Xi}(s) \cdot \dot{\boldsymbol{\Xi}}(s)}{\|\boldsymbol{\Xi}(s)\|^2} ds. \tag{B.4}$$

We decided to use (B.3) to find libration orbits, instead of (B.4) since the chaos indicator (B.3) converge faster for a libration orbit. As a matter of fact, for libration orbits the function

$$f_1(\boldsymbol{\xi}, \boldsymbol{\Xi}, s) := w(\boldsymbol{\xi}(s)) \frac{\boldsymbol{\Xi}(s) \cdot \dot{\boldsymbol{\Xi}}(s)}{\|\boldsymbol{\Xi}(s)\|^2} \tag{B.5}$$

has oscillation terms, but the computation of the integral (B.4) cancels their contributions. If we consider the integrand

$$f_2(\boldsymbol{\xi}, \boldsymbol{\Xi}, s) := \max\left(0, f_1(\boldsymbol{\xi}, \boldsymbol{\Xi}, s)\right) \tag{B.6}$$

the integral (B.3) sums up all the contributions due to the oscillation terms.

As numerical example, let us consider the forced in time mechanical pendulum whose system

of differential equations is

$$\begin{cases} \dot{\xi}_1 &= \xi_2 \\ \dot{\xi}_2 &= -\sin(\xi_1)\,(1-\epsilon\sin(t)) \end{cases} \tag{B.7}$$

and the variational equations are

$$\begin{cases} \dot{\Xi}_1 &= \Xi_2 \\ \dot{\Xi}_2 &= -\cos(\xi_1)\,(1-\epsilon\sin(t))\,\Xi_1 \end{cases} \tag{B.8}$$

where $\epsilon = 5 \times 10^{-2}$. We note that when $\epsilon = 0$ the system reduces to the integrable mechanical pendulum having $(\xi_1^*, \xi_2^*) = (\pi, 0)$ as hyperbolic equilibrium point.

We numerically integrate the equations of motion with the initial data $\xi_1(0) = \pi - 0.69$, $\xi_2(0) = 0$, the initial tangent vector $\Xi_1(0) = 1/\sqrt{2}$, $\Xi_2(0) = 1/\sqrt{2}$ and in the time interval $[0, 50]$. The orbit, the evolution of the functions f_1 and f_2, and of the two chaos indicators (B.4) and (B.3) with $w(\boldsymbol{\xi}) = 1$, are shown in Fig. B.1. We emphasize that the chaos indicator (B.3) grows more rapidly with respect to (B.4) (the reader is referred to the right bottom panel of Fig. B.1). As a consequence, we understand if a orbit is librating or not in a shorter time-span.

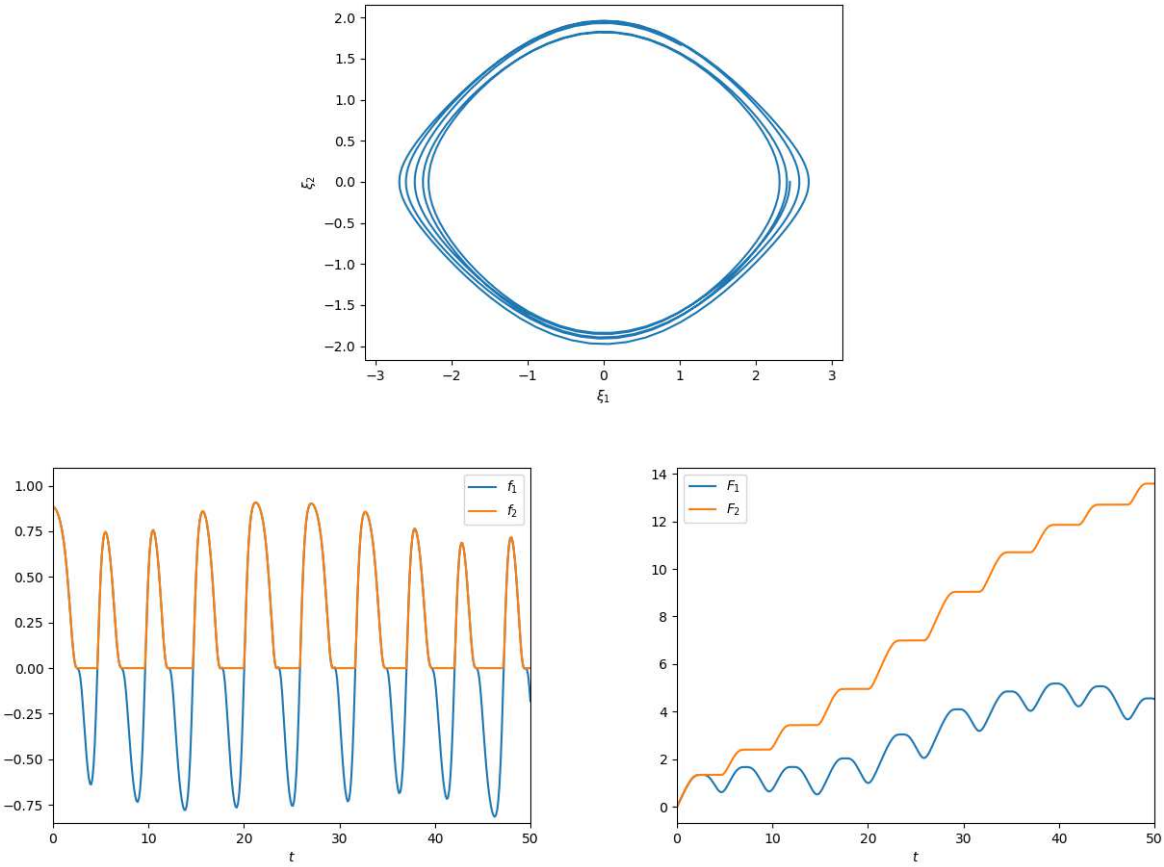

Figure B.1: Orbit found via numerical integration with initial data $\xi_1(0) = \pi - 0.69$, $\xi_2(0) = 0$, the initial tangent vector $\Xi_1(0) = 1/\sqrt{2}$, $\Xi_2(0) = 1/\sqrt{2}$ and in the time interval $[0, 50]$. The orbit is a libration around the origin. The second panel displays the evolution of f_1 and f_2 in time, while the third panel shows the evolution of (B.4), denoted by F_1 in the figure, and of (B.3), denoted by F_2.

Appendix C

Orbital elements of L_1 and L_2 in the elliptic restricted three-body problem

Let us consider the elliptic restricted three-body problem, in which a planet P_j of gravitational parameter ε_j is performing an elliptic motion with semi-major axis a_j, eccentricity e_j, longitude of perihelion ϖ_j and true anomaly f_j around the Sun of gravitational parameter μ. Let use denote by $(X_{L_i}, 0)$ the position vector of L_1 or L_2 in the rotating-pulsating reference frame, and $\Gamma = |X_{L_i}|$.

In this appendix we aim to compute the orbital elements a, e, ϖ and f of the Lagrangian solutions. In the inertial reference frame the position vectors of the Lagrangian point and P_j are respectively:

$$\boldsymbol{r} = \frac{a(1-e^2)}{1+e\cos f}\left(\cos(f+\varpi), \sin(f+\varpi)\right) \tag{C.1}$$

$$\boldsymbol{r}_j = \frac{a_j(1-e_j^2)}{1+e_j\cos f_j}\left(\cos(f_j+\varpi_j), \sin(f_j+\varpi_j)\right) \tag{C.2}$$

At the Lagrangian points we have

$$\boldsymbol{r} = \Gamma \boldsymbol{r}_j. \tag{C.3}$$

From Eq. (C.3) we immediately obtain the two relations:

$$f + \varpi = f_j + \varpi_j, \tag{C.4}$$

$$\frac{a(1-e^2)}{1+e\cos f} = \Gamma \frac{a_j(1-e_j^2)}{1+e_j\cos f_j}. \tag{C.5}$$

The velocity of the Lagrangian solution and P_j in the inertial reference frame are respectively:

$$\boldsymbol{v} = \sqrt{\frac{\mu}{a(1-e^2)}}\left(e\sin f(\cos(f+\varpi), \sin(f+\varpi)) + (1+e\cos f)(-\sin(f+\varpi), \cos(f+\varpi))\right) \tag{C.6}$$

$$\boldsymbol{v}_j = \sqrt{\frac{\mu}{a_j(1-e_j^2)}}\left(e_j\sin f_j(\cos(f_j+\varpi_j), \sin(f_j+\varpi_j)) + (1+e_j\cos f_j)(-\sin(f_j+\varpi_j), \cos(f_j+\varpi_j))\right) \tag{C.7}$$

where we assume that ε_j is negligible with respect μ.

Since $\boldsymbol{v} = \Gamma \boldsymbol{v}_j$ we obtain

$$\frac{e \sin f}{\sqrt{a(1-e^2)}} = \Gamma \frac{e_j \sin f_j}{\sqrt{a_j(1-e_j^2)}} \tag{C.8}$$

$$\frac{1 + e \cos f}{\sqrt{a(1-e^2)}} = \Gamma \frac{1 + e_j \cos f_j}{\sqrt{a_j(1-e_j^2)}} \tag{C.9}$$

By dividing Eq. (C.8) with (C.9) we get

$$\frac{e \sin f}{1 + e \cos f} = \frac{e_j \sin f_j}{1 + e_j \cos f_j}, \tag{C.10}$$

while multiplying Eq. (C.5) by Eq. (C.9) we obtain

$$a(1-e^2) = \Gamma^4 a_j (1-e_j^2); \tag{C.11}$$

hence, to determine the orbital elements of the Lagrangian solutions we solve the system

$$\begin{cases} \frac{a(1-e^2)}{1+e\cos f} = \Gamma \frac{a_j(1-e_j^2)}{1+e_j \cos f_j} \\ \frac{e \sin f}{\sqrt{a(1-e^2)}} = \Gamma \frac{e_j \sin f_j}{\sqrt{a_j(1-e_j^2)}} \\ a(1-e^2) = \Gamma^4 a_j (1-e_j^2) \end{cases} \tag{C.12}$$

For this reason, we define the variables

$$\xi = e \cos f \quad \eta = e \sin f. \tag{C.13}$$

Then, the solution of system (C.12) is

$$a = -\frac{a_j(1-e_j^2)\Gamma}{2e_j(\Gamma^3 - 1)\cos f_j + (1+e_j^2)\Gamma^3 - 2} \tag{C.14}$$

$$\xi = \Gamma^3 - 1 + e_j \Gamma^3 \cos f_j, \qquad \eta = e_j \Gamma^3 \sin f_j. \tag{C.15}$$

Hence ξ and η describe a circumference parameterized by f_j, whose center and radius are $(\Gamma^3 - 1, 0)$ and $e_j \Gamma^3$ respectively.

To represent the longitude of pericenter of the Lagrangian solution we introduce the variables

$$\tilde{\xi} = e \cos \varpi, \quad \tilde{\eta} = e \sin \varpi. \tag{C.16}$$

Then

$$\begin{aligned} \tilde{\xi} &= e \cos(f_j + \varpi_j - f) = e\left(\cos f \cos(f_j + \varpi_j) + \sin f \sin(f_j + \varpi_j)\right) \\ &= \xi \cos(f_j + \varpi_j) + \eta \sin(f_j + \varpi_j) \end{aligned} \tag{C.17}$$

$$\begin{aligned} \tilde{\eta} &= e \sin(f_j + \varpi_j - f) = e\left(\cos f \sin(f_j + \varpi_j) - \sin f \cos(f_j + \varpi_j)\right) \\ &= \xi \sin(f_j + \varpi_j) - \eta \cos(f_j + \varpi_j) \end{aligned} \tag{C.18}$$

$$\implies \tilde{\xi} = e_j \Gamma^3 \cos \varpi_j + (\Gamma^3 - 1)\cos(f_j + \varpi_j), \qquad \tilde{\eta} = e_j \Gamma^3 \sin \varpi_j + (\Gamma^3 - 1)\sin(f_j + \varpi_j); \tag{C.19}$$

hence $\tilde{\xi}$ and $\tilde{\eta}$ describe a circumference parameterized by f_j, whose center and radius are $(e_j\Gamma^3\cos\varpi_j$, $e_j\Gamma^3\sin\varpi_j)$ and $|\Gamma^3-1|$ respectively.

Since $|\Gamma^3-1|\approx 3^{2/3}\sqrt[3]{\varepsilon_j}=3r_{\rm H}$, where $r_{\rm H}$ denote the Hill radius of P_j, and $e_j\Gamma^3\approx e_j$, we obtain

$$\xi\approx 3r_{\rm H}+e_j\cos f_j,\qquad \eta\approx e_j\sin f_j \tag{C.20}$$

$$\tilde{\xi}\approx e_j\cos\varpi_j+3r_{\rm H}\cos(f_j+\varpi_j),\qquad \tilde{\eta}\approx e_j\sin\varpi_j+3r_{\rm H}\sin(f_j+\varpi_j). \tag{C.21}$$

We emphasize that if:

- $3r_{\rm H}\gtrsim e_j$, then $\varpi\in[0,2\pi]$, while f is bounded;
- $3r_{\rm H}\lesssim e_j$, then ϖ is bounded, while $f\in[0,2\pi]$.

In Fig. C.1 we plot the circumferences describing (ξ,η) and $(\tilde{\xi},\tilde{\eta})$ for both $3r_{\rm H}\gtrsim e_j$ and $3r_{\rm H}\lesssim e_j$.

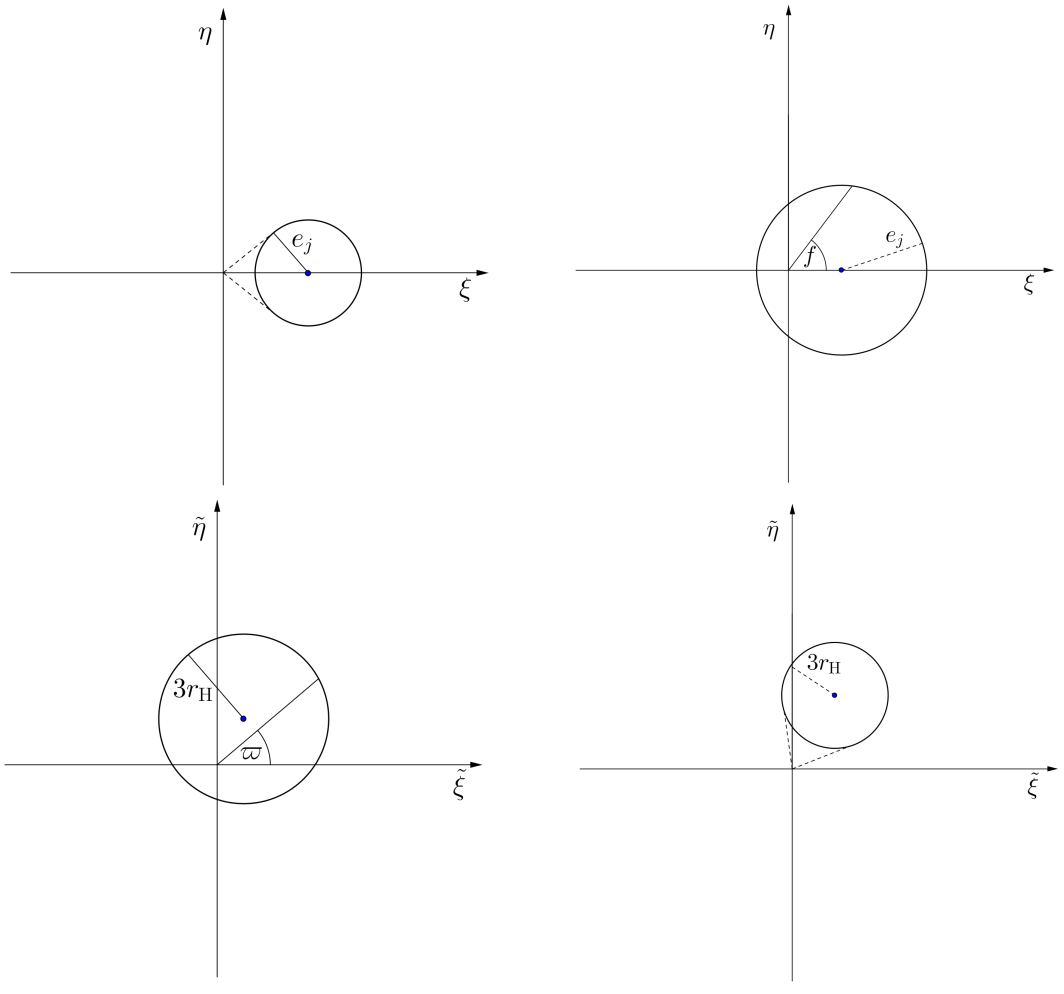

(a) $3r_{\rm H}\gtrsim e_j$. (b) $3r_{\rm H}\lesssim e_j$.

Figure C.1: Representation of the variables (ξ,η) and $(\tilde{\xi},\tilde{\eta})$ for $3r_{\rm H}\gtrsim e_j$ (panels on the left) and $3r_{\rm H}\lesssim e_j$ (panels on the right).

Bibliography

A.F.B de Almeida Prado. Numerical and analytical study of the gravitational capture in the bicircular problem. *Advances in Space Research*, 36:578–584, 2005.

M.A. Andreu. *The quasi-bicircular problem.* PhD thesis, Universitat de Barcelona, 1998.

M.A. Andreu. Dynamics in the center manifold around L_2 in the quasi-bicircular problem. *Celestial Mechanics*, 84:105–133, 2002.

V.I Arnold. *Mathematical Methods of Classical Mechanics.* Springer-Verlag, 1989.

V.I. Arnold, V.V. Kozlov, and A.I. Neishtadt. *Dynamical systems III. Mathematical aspects of classical and celestial mechanics.* Encyclopaedia of mathematical sciences, Springer, 2nd edition, 1993.

E. Barrabés, G. Gómez, J.M. Mondelo, and M. Ollè. Pseudo-heteroclinic connections between bicircular restricted four-body problems. *Monthly Notices of the Royal Astronomical Society*, 462:740–750, 2016.

E. Barrabés and M. Ollé. Invariant manifolds of L_3 and horseshoes motion in the restricted three-body problem. *Nonlinearity*, 19:2065–2089, 2006.

E. Belbruno, M. Gidea, and F. Topputo. Weak Stabilty Boundary and Invariant Manifolds. *SIAM Journal on Applied Dynamical Systems*, 9:1061–1089, 2010.

M. Belló, G. Gómez, and J.J. Masdemont. Invariant manifolds, Lagrangian trajectories and space mission design. *Space Manifolds Dynamics, E. Perozzi, S. Ferraz-Mello eds., Springer*, 2010.

G. Benettin. *The elements of Hamiltonian perturbations theory, lectures at the Porquerolles school 2001 "Hamiltonian systems and Fourier analysis".* D. Benest, C. Froeschlé e E. Lega editori, Cambridge Scientific (UK), 2004.

G. Benettin, L. Galgani, A. Giorgilli, and J.M. Strelcyn. Lyapunov characteristic exponents for smooth dynamical systems: a method for computing all of them. *Meccanica*, 15:9–15, 1980a.

G. Benettin, L. Galgani, A. Giorgilli, and J.M. Strelcyn. Lyapunov characteristic exponents for smooth dynamical systems: a method for computing all of them. *Meccanica*, 15:21–30, 1980b.

J.V. Breakwell. Investigation of halo satellite orbit control. *Technical Report, NASA-CR-132858*, 1970.

R. Broucke. Stability of periodic orbits in the elliptic, restricted three-body problem. *AIAA Journal*, 7, 1969.

S. Bucciarelli, M. Ceccaroni, A. Celletti, and G. Pucacco. Qualitative and analytical results of the bifurcation thresholds to halo orbits. *Annali di Matematica Pura ed Applicata*, 195:489–512, 2016.

S. Campagnola and R.P. Russell. Endgame problem Part 1: V-Infinity leveraging technique and the leveraging graph. *Journal of Guidance, Control, and Dynamics*, 33:463–475, 2010a.

S. Campagnola and R.P. Russell. Endgame Problem Part 2: Multibody technique and the Tisserand-Poincaré graph. *Journal of Guidance, Control, and Dynamics*, 33:476–486, 2010b.

M.J. Capiński and P. Roldán. Existence of a center manifold in a pratical domain around L_1 in the restricted three-body problem. *SIAM Journal of Applied Dynamical Systems*, 11:285–318, 2012.

M.J. Capinski, M. Gidea, and R. de la Llave. Arnold diffusion in the planar elliptic restricted three-body problem: mechanics and numerical verification. *Nonlinearity*, 30:329, 2016.

C. Caracciolo and U. Locatelli. Computer-assisted estimates for Birkhoff normal forms. *Journal of Computational Dynamics*, 7:425–460, 2020.

M. Ceccaroni, A. Celletti, and G. Pucacco. Halo orbits around the collinear points of the restricted three-body problem. *Physica D: Nonlinear Phenomena*, 317:28–42, 2016.

A. Celletti and C. Froeschlé. Numerical investigation of the break-down threshold for a restricted three-body problem. *Planetary and Space Science*, 46:1535–1542, 1998.

A. Celletti and C. Gales. On the dynamics of space debris 1:1 and 2:1 resonances. *Journal of Nonlinear Science*, 24:1231–1262, 2014.

A. Celletti and C. Gales. A study of the lunisolar secular resonance $2\dot{\omega} + \dot{\Omega} = 0$. *Frontiers in Astronomy and Space Sciences - Fundamental Astronomy*, 2016.

A. Celletti and A. Giorgilli. On the stability of the Lagrangian points in the spatial restricted problem of three bodies. *Celestial Mechanics and Dynamical Astronomy*, 50:31–58, 1990.

A. Celletti, G. Pucacco, and D. Stella. Lissajous and halo orbits in the restricted three-body problem. *Journal of Nonlinear Science*, 25:353–370, 2015.

A. Celletti, C. Gales, and G. Pucacco. Bifurcations of lunisolar secular resonances for space debris orbits. *SIAM Journal of Applied Dynamical Systems*, 15:1352–1383, 2016.

A. Celletti, C. Efthymiopoulos, F. Gachet, C. Gales, and G. Pucacco. Dynamical models and the onset of chaos in space debris. *Internation Journal of Nonlinear Mechanics*, 90:147–163, 2017.

P. Cincotta and C. Simó. Simple tools to study global dynamics in non aximmetric galactic potentials-I. *Astronomy and Astrophysical Supplement Series*, 147:205, 2000.

J. Cobos and J.J. Masdemont. *Astrodynamical applications of invariant manifolds associated with collinear Lissajous libration orbits. In Libration point orbits and applications.* World Scientific, Gómez, G., Lo, M.W. and Masdemont, J.J. edition, 2003.

C.C. Conley. Low energy transit orbits in the restricted three-body problem. *SIAM Journal on Applied Mathematics*, 16:732–746, 1968.

H. Curtis. *Orbital Mechanics for Engineering Students.* Elsevier Aerospace Engineering Series, 2005.

J. Daquin, A.J. Rosengren, F. Deleflie, E.M. Alessi, G.B. Valsecchi, and A. Rossi. The dynamical structure of the MEO region: long-term stability, chaos, and transport. *Celestial Mechanics and Dynamical Astronomy*, 2016.

J. Daquin, I. Gkolias, and A.J. Rosengren. Drift and its mediation in terrestrial orbits. *Frontiera in Applied Mathematics and Statistics*, 4:35, 2018.

J. Daquin, E.M. Alessi, J. O' Leary, A. Lemaitre, and A. Buzzoni. Dynamical properties of the Molniya satellite constellation: long-term evolution of the semi-major axis. *arxiv:2103.06251v2*, 2021a.

J. Daquin, E. Legnaro, I. Gkolias, and C. Efthymiopoulos. A deep dive into the $2g+h$ resonance: separatrices, manifolds and phase space structure of navigation satellites. *arXiv:2107.14507*, 2021b.

A.F.B. de Almeida Prado. Close-approach trajectories in the elliptic restricted problem. *Journal of Guidance, Control, and Dynamics*, 20:797, 1997.

A.F.B. de Almeida Prado and E.V. Neto. Study of the gravitational capture in the elliptical restricted three-body problem. *The Journal of the Astronautical Sciences*, 54:567–582, 2006.

D.W. Dunham and R.W. Farquhar. *Libration Point Missions, 1978-2003. In Libration point orbits and applications.* World Scientific, Gómez, G. and Lo, M.W. and Masdemont, J.J. edition, 2003.

C. Efthymiopoulos. High order normal form stability estimates for co-orbital motion. *Celestial Mechanics and Dynamical Astronomy*, 117:101–112, 2013.

E.A. Euler and E.Y. Yu. Optimal station keeping at collinear points. *Journal Spacecraft and Rockets*, 8: 513–517, 1971.

R.W. Farquhar. *The control and use of libration-point satellites*. PhD thesis, Stanford University, 1968.

R.W. Farquhar. The Flight of ISEE-3 (ICE: Origins, Mission History, and a Legacy. *AIAA Paper 98-4464*, 1998.

R.W. Farquhar, D.P. Muhonen, and Richardson D.L. Mission design for a halo orbiter of the Earth. *Journal Spacecraft and Rockets*, 14:170–177, 1977.

R.W. Farquhar, D.P. Muhonen, C.R. Newman, and H.S. Heuberger. The first libration-point satellite - Mission overview and flight history. *AAS/AIAA Astrodynamics Specialist Conference*, 1979.

R.W. Farquhar, D.W. Dunham, Y. Guo, and J.V. McAdams. Utilization of libration points for human exploration in the Sun–Earth–Moon system and beyond. *Acta Astronautica*, 55:687–700, 2004.

A. Farrés and À. Jorba. Dynamics of a Solar Sail near a Halo orbit. *Acta Astronautica*, 67:979–990, 2010.

F. Ferrari and F. Lavagna. Periodic motion around libration points in the Elliptic Restricted Three-Body Problem. *Nonlinear Dynamics*, 93:453–462, 2018.

A.F.S. Ferreira, A.F.B. de Almeida Prado, O.C. Winter, and D.P.S. Santos. Effects of the eccentricity of the primaries in powered swing-by maneuvers. *Advances in Space Research*, 59:2071–2087, 2017.

A.F.S. Ferreira, A.F.B.A. Prado, O.C. Winter, and D.P.S. Santos. Analytical study of the swing-by maneuver in an elliptical system. *Astrophysics and Space Science*, 363, 2018.

G. Floquet. Sur les èquations diffèrentielles linèaires á coefficients périodiques. *Annales Scientifique de l'École Supérieure*, 12:47–88, 1883.

D. Folta and M. Beckman. *Libration Orbit Mission Design: Applications of Numerical and Dynamical Methods. In Libration point orbits and applications*. World Scientific, Gómez, G., Lo, M.W. and Masdemont, J.J. edition, 2003.

C. Froeschlé, R. Gonczi, and E. Lega. The fast Lyapunov indicator: a simple tool to detect weak chaos. Application to the structure of the main asteroidal belt. *Planetary and Space Science*, 45:881–886, 1997a.

C. Froeschlé, E. Lega, and R. Gonczi. Fast Lyapunov Indicators. Application to asteroidal motion. *Celestial Mechanics and Dynamical Astronomy*, 67:41–62, 1997b.

C. Froeschlé, M. Guzzo, and E. Lega. Graphical evolution of the Arnold web: from order to chaos. *Science*, 289:2108–2110, 2000.

F. Gabern and Á. Jorba. A restricted four-body model for the dynamics near the Lagrangian points of the Sun–Jupiter system. *Discrete and Continuous Dynamical Systems Series B*, 1:143–182, 2001.

F. Gabern, Á. Jorba, and U. Locatelli. On the construction of the Kolmogorov normal form for the trojan asteroids. *Nonlinearity*, 18:1705, 2005.

E.S. Gawlik, J.E. Marsden, P.C. Du Toit, and S. Campagnola. Lagrangian coherent structures in the planar elliptic restricted three-body problem. *Celest Mech Dyn Ast*, 103:227–249, 2009.

A. Giorgilli. On a theorem of Lyapunov. *Rendiconti dell'Istituto Lombardo Accademia di Scienze e Lettere*, 146:133–160, 2012.

I. Gkolias, J. Daquin, D.K. Skoulidou, K. Tsiganis, and C. Efthymiopouos. Chaotic transport of navigation satellite. *Chaos*, 29, 2019.

G. Gómez and J.M. Mondelo. The dynamics around the collinear equilibrium points of the RTBP. *Physica D: Nonlinear Phenomena*, pages 283–321, 2001.

G. Gómez, À. Jorba, J.J. Masdemont, and C. Simó. Study of the transfer from the Earth to a Halo orbits around the equilibrium point L_1. *Celestial Mechanics and Dynamical Astronomy*, 56:541–562, 1993.

G. Gómez, J.J. Masdemont, and C. Simó. Study of the transfer between halo orbits. *Acta Astronautica*, 43: 493–520, 1998.

G. Gómez, À. Jorba, J. Masdemont, and C. Simó. *Dynamics and mission design near libration point orbits* Advanced Methods for Collinear Points, volume 3. Singapore: World Scientific, 2000.

G. Gómez, W.S. Koon, M.W. Lo, J.E. Marsden, J. Masdemont, and S.D. Ross. Connecting orbits and invariant manifolds in the spatial restricted three-body problem. *Nonlinearity*, 17:1571–1606, 2004.

J. Gómez, Llibre, R. Martinez, and C. Simó. *Dynamics and mission design near libration point*, volume 1 of World Scientific Monograph Series in Mathematics. World Scientific Publishing Co. Inc., 2001.

M. Guzzo. The web of three–planets resonances in the outer Solar System. *Icarus*, 174:273–284, 2005.

M. Guzzo. The web of three-planet resonances in the outer solar system II: a source of orbital instability for Uranus and Neptune. *Icarus*, 181:475–485, 2006.

M. Guzzo. *Space Manifold Dynamics: Novel Spaceways for Science and Exploration*. Springer, E. Perozzi, S. Ferraz-Mello edition, 2010.

M. Guzzo and E. Lega. On the identification of multiple close encounters in the planar circular restricted three-body problem. *Monthly Notices of the Royal Astronomical Society*, 428:2688, 2013.

M. Guzzo and E. Lega. Evolution of the tangent vectors and localization of the stable and unstable manifolds of hyperbolic orbits by Fast Lyapunov Indicators. *SIAM Journal on Applied Mathematics*, 74:1058–1086, 2014.

M. Guzzo and E. Lega. A study of the past dynamics of comet 67P/Churyumov-Gerasimenko with fast Lyapunov indicators. *Astronomy & Astrophysics*, 579:A79, 2015.

M. Guzzo and E. Lega. Scenarios for the dynamics of comet 67P over the past 500 kyr. *Monthly Notices of the Royal Astronomical Society*, 469:S321, 2017.

M. Guzzo and E. Lega. Geometric chaos indicators and computations of the spherical hypertube manifolds of the spatial circular restricted three-body problem. *Physica D: Nonlinear Phenomena*, 373:38, 2018.

M. Guzzo and E. Lega. Theory and applications of Fast Lyapunov Indicators for the computation of transit orbits in the three-body problem. hal-03326476, 2021.

M. Guzzo, E. Lega, and Cl. Froeschlé. On the numerical detection of the effective stability of chaotic motions in quasi-integrable systems. *Physica D: Nonlinear Phenomena*, 163:1–25, 2002.

M. Guzzo, E. Lega, and Cl. Froeschlé. First numerical evidence of global Arnold diffusion in quasi-integrable systems. *Discrete and Continuous Dynamical Systems – Series B*, 5:687–698, 2005.

M. Guzzo, E. Lega, and Cl. Froeschlé. A numerical study of the topology of normally hyperbolic invariant manifolds supporting Arnold diffusion in quasi-integrable systems. *Physica D: Nonlinear Phenomena*, 238: 1797–1807, 2009.

H. Heuberger. Halo orbit station keepin for ISEE-C. *AAS/AIAA Spaceflight Mechanics Conference*, 1977.

L.A. Hiday-Johnston and K.C. Howell. Transfers between libration-point orbits in the elliptic restricted problem. *Celestial Mechanics and Dynamical Astronomy*, 58:317–337, 1994.

X. Hou, J. Tang, and L. Liu. Transfer to collinear libration point L_3 in the Sun–Earth+Moon system. *NASA Technical Report*, 2007.

X.Y. Hou and L. Liu. On motions around the collinear libration points in the elliptic restricted three-body problem. *Monthly Notices of the Royal Astronomical Society*, 415, 2011.

K.C. Howell and S.C. Gordon. Orbit determination error analysis and a station-keeping strategy for Sun–Earth L_1 libration point orbits. *Journal of the Astronautical Sciences*, 42:207–228, 1994.

K.C. Howell and L.A. Hiday-Johnston. Time-free transfers between libration-point orbits in the elliptic restricted problem. *Acta Astronautica*, 32:245–254, 1994.

K.C. Howell and M. Kakoi. Transfers between the Earth–Moon and Sun–Earth systems using manifolds and transit orbits. *Acta Astronautica*, 59:367–380, 2006.

K.C. Howell and H.J. Pernika. Stationkeeping method for libration point trajectories. *Journal of Guidance, Control and Dynamics*, 16:151–159, 1993.

K.C. Howell, B.T. Barden, and M.W. Lo. Application of dynamical systems theory to trajectory design for a libration point mission. *The Journal of the Astronautical Science*, pages 161–178, 1997.

K.C. Howell, B.T. Barden, R.S. Wilson, and M.W. Lo. Trajectory design using a dynamical systems approach with application to GENESIS. *Advanced in the Astronautical Science*, pages 1665–1684, 1998.

K.C. Howell, M. Beckman, C. Patterson, and D. Folta. Representations of Invariant Manifolds for Applications in Three-Body Systems. *The Journal of the Astronautical Sciences*, 54:69–93, 2006.

N. Hyeraci and F. Topputo. Method to design ballistic capture in the elliptic restricted three-body problem. *Journal of Guidance, Control, and Dynamics*, 33:1814, 2010.

Á. Jorba. A methodology for the numerical computation of normal forms, centre manifolds and first integrals of hamiltonian systems. *Experimental Mathematics*, 8:155–195, 1999.

Á. Jorba. The Lagrangian solutions. *UNESCO Encyclopedia of Life Support Systems*, 6.119.55, 2012.

Á. Jorba and A. Farrès. On the high order approximation of the centre manifold for ODEs. *Discrete and Continuous Dynamical Systems - Series B*, 14:977–1000, 2010.

Á. Jorba and J. Masdemont. Dynamics in the center manifold of the collinear points of the restricted three body problem. *Physica D: Nonlinear Phenomena*, 132:189–213, 1999.

Á. Jorba and B. Nicolás. Transport and invariant manifolds near L_3 in the Earth–Moon bicircular model. *Communications in Nonlinear Science and Numerical Simulation*, 89:105327, 2020.

Á. Jorba and J. Villanueva. Numerical Computation of normal forms around some periodic orbits of the restricted three body problem. *Physica D: Nonlinear Phenomena*, 114:197–229, 1998.

Á. Jorba, M. Jorba-Cuscò, and J.J. Rosales. The vicinity of the Earth–Moon L_1 point in the bicircular problem. *Celestial Mechanics and Dynamical Astronomy*, 132:11, 2020.

W.S. Koon, M. Lo, J. Marsden, and S. Ross. Low energy transfer to the Moon. *Celestial Mechanics and Dynamical Astronomy*, 81:63–73, 2001.

W.S. Koon, M.W. Lo, J.E. Marsden, and S.D. Ross. *Dynamical systems, the three-body problem and space mission design*. Marsden Books, 2008.

B. Kumar, R.L. Anderson, and R. de la Llave. Rapid and accurate methods for computing whiskered tori and their manifolds in periodically perturbed planar circular restricted three-body problems. *To appear in Celestial Mechanics and Dynamical Astronomy, arXiv:2105.11100*, 2021.

E. Lega and M. Guzzo. *Theory and applications of the fast Lyapunov indicator (FLI) method, in: Lecture notes in Physics 915*. Chaos Detection and Predictability, 2016a.

E. Lega and M. Guzzo. Three-dimensional representations of the tube manifolds of the planar restricted three-body problem. *Physica D: Nonlinear Phenomena*, 325:41–52, 2016b.

E. Lega, M. Guzzo, and Cl. Froeschlé. Detection of Arnold diffusion in Hamiltonian systems. *Physica D: Nonlinear Phenomena*, 182:179–187, 2003.

E. Lega, M. Guzzo, and C. Froeschlé. Detection of close encounters and resonances in three-body problems through Levi-Civita regularization. *Monthly Notices of the Royal Astronomical Society*, 418:107, 2011.

Ch. Lhotka, C. Efthymiopoulos, and R. Dvorak. Nekhoroshev stability at L_4 or L_5 in the elliptic-restricted three-body problem – application to Trojan asteroids. *Monthly Notices of the Royal Astronomical Society*, 384:1165–1177, 2008.

J. Llibre and C. Piñol. On the elliptic restricted three-body problem. *Celestial Mechanics and Dynamical Astronomy*, 48:319–345, 1990.

J. Llibre, R. Martínez, and C. Simó. Tranversality of the invariant manifolds associated to the Lyapunov family of periodic orbits near L_2 in the restricted three-body problem. *Journal of Differential Equations*, 58:104–156, 1985.

S.S. Lukjanov. Control of a spacecraft motion in the vicinity of a collinear libration point of the circular three-body problem by means of light pressure. *Cosmic Research*, 19:518–527, 1980.

C. Martin, B.A. Conway, and P. Ibánez. *Space Manifold Dynamics: Novel Spaceways for Science and Exploration*. Springer, E. Perozzi, S. Ferraz-Mello edition, 2010.

M. Michalodimitrakis. The circular restricted four-body problem. *Astrophysics and Space Science*, 75: 289–305, 1981.

J.K. Miller and C.J. Weeks. Application of Tisserand's criterion to the design of gravity assist trajectories. *AIAA*, 2002.

A. Morbidelli. *Modern Celestial Mechanics. Aspects of Solar System Dynamics*. 2011.

D.P. Muhanen. Accelerometer enhanced orbit control near the Sun–Earth L_1 libration point. *Space Flight Mechanics, Science and Technology Series, AIAA Paper 83-0018*, 1983.

R.B. Negri and A.F.B. Prado. Generalizing the bicircular restricted four-body problem. *Journal of Guidance, Control, and Dynamics*, 43, 2020.

R.I. Paez. *New normal form approaches adapted to the Trojan problem*. PhD thesis, Universitá degli Studi di Roma "Tor Vergata", 2016.

R.I. Paez and C. Efthymiopoulos. Trojan resonant dynamics, stability, and chaotic diffusion, for parameters relevant to exoplanetary systems. *Celestial Mechanics and Dynamical Astronomy*, 121:139–170, 2015.

R.I. Paez and M. Guzzo. A study of temporary captures and collisions in the circular restricted three-body problem with normalizations of the Levi-Civita Hamiltonian. *International Journal of Non-Linear Mechanics*, 120:103417, 2020.

R.I. Paez and M. Guzzo. Transits close to the lagrangian solutions L_1, L_2 in the Elliptic restricted three-body problem. *Nonlinearity*, 34:6417, 2021.

R.I. Paez and U. Locatelli. Design of maneuvers based on new normal form approximations: the case study of the CPRTBP. *ICNPAA 2014 proceedings, AIP Conference Proceedings*, 1637:776, 2014.

R.I. Paez and U. Locatelli. Trojan dynamics well approximated by a new Hamiltonian normal form. *Monthly Notices of the Royal Astronomical Society*, 453:2177, 2015.

F. Paita, A. Celletti, and G. Pucacco. Element history of the Laplace resonance: a dynamical approach. *Astronomy & Astrophysics*, 617:A35, 2018.

J. Palacián and P. Yanguas. *Invariant manifolds of spatial restricted three-body problems: the lunar case.* New Advances in Celestial Mechanics and Hamiltonian Systems. J. Delgado, E. A. Lacomba, J. Llibre and E. Pérez Chavela, Dordrecht: Kluwer, 2004.

J.F. Palacián, P. Yangua, S. Fernández, and M.A. Nicotra. Searching for periodic orbits of the spatial elliptic restricted three-body problem by double averaging. *Physica D: Nonlinear Phenomena*, 213:15–24, 2006.

J. Parker and R.L. Anderson. *Low-energy lunar trajectory design*. Pasadena, CA: Jet Propulsion Laboratory, California Institute of Technology, 2013.

H. Peng and S. Xu. Stability of two groups of multi-revolution elliptic halo orbits in the elliptic restricted three-body problem. *Celestial Mechanics and Dynamical Astronomy*, 123:279–303, 2015.

H. Peng, Y. Qi, S. Xu, and Y. Li. *AAS/AIAA Spaceflight Mechanics Conference. Williamsburg, VA*, 2015.

H. Peng, X. Bai, and S. Xu. Continuation of periodic orbits in the Sun–Mercury elliptic restricted three-body problem. *Communications in Nonlinear Science and Numerical Simulations*, 47:1–15, 2017.

P. Pergola, K. Geurts, C. Casaregola, and M. Andrenucci. Earth–Mars halo to halo low-thrust manifold transfer. *Celestial Mechanics and Dynamical Astronomy*, 105:19–32, 2009.

H. Poincaré. *Les méthodes nouvelles de la Mécanique Céleste*, volume 1. Gautier-Villars, Paris, 1892.

G. Pucacco. Structure of the centre manifold of the L_1, L_2 collinear libration points in the restricted three-body problem. *Celestial Mechanics and Dynamical Astronomy*, 131, 2019.

Y. Qi and A. de Ruiter. Energy analysis in the elliptic restricted three-body problem. *Monthly Notices of the Royal Astronomical Society*, 478:1392–1402, 2018.

Y. Qi, S. Xu, and R. Qi. Transfer from Earth to libration point orbit using lunar gravity assist. *Acta Astronautica*, 133:145–157, 2017.

Y. Ren, J.J. Masdemont, G. Gòmez, and E. Fantino. Two mechanisms of natural transport in the Solar System. *Communications in Nonlinear Science and Numerical Simulation*, 17:844–853, 2012.

A.J. Rosengren, J. Daquin, K. Tsiganis, E.M. Alessi, F. Deleflie, A. Rossi, and G.B. Valsecchi. Galileo disposal strategy: stability, chaos and predictability. *Monthly Notices of the Royal Astronomical Society*, 464:4063–4076, 2017.

E. Scantamburlo. On the computation of the dynamical substitutes for the Lagrange equilibria in the bi-circular restricted four-body problem. Master's thesis, Universitá degli Studi di Padova, 2018.

E. Scantamburlo and M. Guzzo. Short-period effects of the planetary perturbations on the Sun–Earth Lagrangian point L_3. *Astronomy & Astrophysics*, 638:A137, 2020.

E. Scantamburlo, M. Guzzo, and R.I. Paez. Interplanetary transfers using stable and unstable manifold tubes originating at L_1 and L_2 in the elliptic restricted three-body problems. hal-03436121, 2021.

J. Sijbrand. Properties of center manifolds. *Transactions of the American Mathematical Society*, 289:431–469, 1985.

C. Simó. *Hamiltonian Systems with Three or more degrees of freedom*, volume 533. NATO Advanced Science Institutes Series C. Mathematical and Physics Sciences, 1999.

C. Simó. *On the analytical and numerical approximations of invariant manifolds, in Modern Methods in Celestial Mechanics*. Editions Frontières, D. Benest, Cl. Froeschlé edition, 2010.

C. Simó, G. Gómez, J. Llibre, and R. Martínez. Station keeping of a quasiperiodic halo orbit using invariant manifolds. *Second International Symposium on Spacecraft Flight Dynamics ESA SP-255*, pages 61–70, 1986.

C. Simó, G. Gómez, R. Martínez, and J. Rodriguez. On the optimal station keeping control of Halo orbits. *Acta Astronautica*, 15:391–397, 1987.

N.L. Strange and J.M. Longuski. Graphical methods for gravity-assit trajectory design. *Journal of Spacecraft and Rockets*, 39:9–16, 2002.

V. Szebehely. *Theory of Orbits*. Academic Press INC. (LONDON) LTD, 1967.

V. Szebehely and G.E.O. Giacaglia. On the Elliptic Restricted Problem of Three Bodies. *The Astronomical Journal*, 69, 1964.

X.Z. Tang and A.H. Boozer. Finite time Lyapunov exponent and advection-diffusion equation. *Physica D: Nonlinear Phenomena*, 95:283–305, 1996.

M. Tantardini, E. Fantino, Y. Ren, P. Pergola, G. Gómez, and J. J. Masdemont. Spacecraft trajectories to the L_3 point of the Sun–Earth three-body problem. *Celestial Mechanics and Dynamical Astronomy*, 108: 215–232, 2010.

A. Tartaglia, E.C. Lorenzini, D. Lucchesi, G. Pucacco, M.L. Ruggiero, and M.L. Valko. How to use the Sun–Earth Lagrange points for fundamentals physics and navigation. *General Relativity and Gravitation*, 2018.

M.O. Terra, C. Simó, and P. de Sousa Silva. Evidences of diffusion related to the center manifold of L_3 of the SRTBP. *In 65th International Astronautical Congress, Toronto, Canada*, 2014.

N. Todorović, D. Wu, and A.J. Rosengren. The arches of chaos in the Solar System. *Science Advances*, 6, 2020.

F. Topputo, M. Vasile, and F. Bernelli-Zazzera. Low energy interplanetary transfers exploiting invariant manifolds of the restricted three-body problem. *The Journal of the Astronautical Sciences*, 53:353–372, 2005.

C.C. van Damme, R.C. Gorgojo, J. Gil-Fernandez, and M. Graziano. *Space Manifold Dynamics: Novel Spaceways for Science and Exploration*. Springer, E. Perozzi, S. Ferraz-Mello edition, 2010.

A. Vanderbauwhede. Centre manifolds, normal forms and elementary bifurcations. *Dynamics reported*, pages 89–169, 1989.

W.E. Wiesel and D.J. Pohlen. Canonical Floquet theory. *Celestial Mechanics and Dynamical Astronomy*, 58:81–96, 1994.

A. Zanzottera, G. Mingotti, R. Castelli, and M. Dellnitz. Intersecting invariant manifolds in spatial restricted three-body problems: design and optimization of Earth-to-halo transfers in the Sun–Earth–Moon scenario. *Communications in Nonlinear Science and Numerical Simulations*, 17:832, 2012.